Reactive Blade Coating for Low-Cost Fabrication of Self-Assembled Metal Nanoparticles for Bio-applications: Disinfecting SARS-CoV-2 to Limit the Spread of COVID-19 Illness

Bita Ebrahimzadeh Asl Tabrizi

A thesis submitted in partial fulfillment of the requirements for the
Master's degree in Biomedical Engineering

Department of Biomedical Engineering
Faculty of Engineering
University of Ottawa

Abstract

Considerable attention has been focused on nanomaterials and their extensive applications. Metallic nanoparticles, especially gold nanoparticles (AuNPs) and silver nanoparticles (AgNPs), due to their superior physical, chemical, and optical properties, are vastly developed for numerous biomedical applications such as drug and gene delivery systems, diagnostic biosensors, imaging, and therapeutics. This study presents a low-cost method for the fabrication of self-assembled metallic nanoparticles, including gold and silver, via a reactive blade coating process, which is carried out based on *in situ* reduction of the metal precursors. This technique is a roll-to-roll compatible technique suitable for scalable nanomanufacturing. Oleylamine was used as a reducer agent and gold (III) chloride hydrate and silver salts, including silver nitrate and silver perchlorate hydrate, used as the metal precursors. Fabrication was carried out by first blade coating the reducer ink and subsequently coating the precursor ink followed by 3 hours of heat treatment. Various solvent systems were used to examine the effect of different solvents on the fabrication process. Surface morphology, crystalline phase composition, and plasmon resonance of the coated samples were characterized by scanning electron microscopy (SEM), X-ray diffractometer (XRD), and UV-Vis spectroscopy, respectively. Results demonstrated the synthesis of spherical self-assembled AuNPs using toluene (TOL) and isopropyl alcohol (IPA) for reducing and precursor solvents, respectively. Changing the concentration of recants or increasing the coating layers exhibited a change in the average size of AuNPs. Self-assembled AuNPs thin films were also demonstrated to have the potential to be used as a biosensing platform based on localized surface plasmon resonance (LSPR) effect to detect the elevated levels of glucose in an aqueous solution.

Recently, the world has faced a pandemic of Covid-19 caused by severe acute respiratory syndrome coronavirus 2 (SARS-CoV-2), which not only has threatened human health but also has brought a worldwide devastating economic and social crisis. Hence, finding a solution to mitigate the current breakout of Covid-19 is vital to protect the international community from its causing harm. AgNPs as an antimicrobial agent, which has exhibited promising antiviral activity against several viruses, can offer a resolution to combat the spread of Covid-19.

In this regard, AgNPs thin films were fabricated analogously via blade coating using various reducer and silver salt inks made of different solvent systems. Virucidal efficacy of reactive blade coated AgNPs on glass substrates was analyzed against human coronavirus 229E, a virus from the

Coronavirus family, as a surrogate SARS-CoV-2 (according to the Level 2 Biosafety facility at uOttawa). Plaque forming assay indicated more than 99.99% reduction in infectivity of the virus when it contacts the AgNPs coated glass for 30 min before infecting cells. These results suggest the excellent potential for reactive blade coated AgNPs as an antiviral agent against coronavirus to avoid the spread of the virus.

Acknowledgment

First and foremost, I would like to express my deepest gratitude to my supervisor, Professor Ghassan Jabbour, for his invaluable direction, continued encouragement, and generous support throughout my research. It has been a splendid opportunity for me to join his lab and conduct research under his supervision. I sincerely appreciate his guidance, patience, understanding, and his financial support during my master's program.

Special thanks to Dr. Mutalifu Abulikemu, Research Associate at the Advanced Materials and Device Laboratories, for being a kind and generous mentor, sharing his extensive knowledge and valuable time, and advising me when there was a conflict in my research.

Many thanks to dr. Shahrokh Ghobadloo, Flow Cytometry and Robotics Core Facility Manager in Prof. Maxim Berezovsky's lab at the Department of Chemistry and Biomolecular Sciences, for providing us with the viral tests and results.

I would also like to thank Centre for Research in Photonics (CRPuO) lab manager dr. Antony Olivera, Howard Northfield, and CRPuO administrative staff Chelsea Barna for providing us the access and training to the NanoFab lab facilities. Many Thanks to dr. Neeraj Joshi for training and access to the instruments at Centre for Advanced Material Research (CAMaR)at the Department of Chemistry and Biomolecular Sciences and to dr. Jeffrey Ovens for access to the uOttawa's X-ray Core Facility.

Finally, I would like to thank my family for their endless support and motivation throughout my academic life. None of my accomplishments would have been possible without them.

Table of Contents

List of figures

List of tables

Abbreviations

AgNPs	Silver nanoparticles
AuNPs	Gold nanoparticle
Covid-19	Coronavirus disease 2019
DCB	Dichlorobenzene
DMSO	Dimethyl sulfoxide
EDS	Energy-dispersive X-ray spectroscopy
FBS	Fatal bovine serum
GOx	Glucose oxidase
HCoV-229E	Human coronavirus 229E
IPA	Isopropyl alcohol
LSPR	Localized surface plasmon resonance
MOI	Multiplicity of infection
PDMS	Polydimethylsiloxane
PET	Polyethylene terephthalate
ROS	Reactive oxygen species
RT	Room temperature
SARS-CoV-2	Severe acute respiratory syndrome coronavirus 2
SEM	Scanning electron microscopy
SPR	Surface plasmon resonance
TBA	Tert-Butyl Alcohol
TOL	Toluene
XRD	X-ray diffractometer

Chapter 1. Introduction

Nanomaterials have been the subject of immense interest in the extensively various fields of research and applications ranging from electronics and the food industry to chemical and biomedical products. This versatility arises from the tunable properties of nanomaterials that can be changed toward the desired purposes [1–4]. According to the report released in 2019, the global market for nanomaterials is projected to rise to US$ 15 Billion by 2027, as the growth of 15.2% is forecasted [5].

Materials and particles with dimensions of nanometer (sub-micron or 1-100 nanometer) scale are defined as nanomaterials and nanoparticles which offer unique characteristics and properties compared to the same elements but in the bulk form [6]. Nanoparticles, having the highest share of the global market for nanomaterials [7], can be obtained from natural resources such as soil colloids, clay minerals, and metal oxides, or to be generated synthetically in the laboratory such as metallic nanoparticles and polymeric nanoparticles [8–10]. Nanoparticles are classified into various categories based on the constituting elements and properties. They include:

1-Nanopolymers and dendrimers, polymeric nanoparticles, polymer nanotubes, nanowires and nanorods, nanocellulose, nanostructured polymer films.

2- Carbon-based nanomaterials such as carbon nanotubes, graphene, and carbon nanofibers.

3- Quantum dots such as carbon dots, which are fluorescence emitting nanoparticles with good biocompatibility that are used for bacteria imaging and identification applications.

4- Inorganic metal oxide nanoparticles (TiO_2, SiO_2, ZnO, $Al(OH)_3$, Fe_2O_3, Fe_3O_4, ZrO_2, CaO)
5- Metals and metal alloys (Au, Ag, Pt, Pd, Cu, Fe, Ni, Co, Al, Mn, Mo) [11, 12].

Medicine and health system are among the most important markets for nanoparticles. Figure 1-1 illustrates the diverse nanoparticles frequently applied in biomedical research and applications.

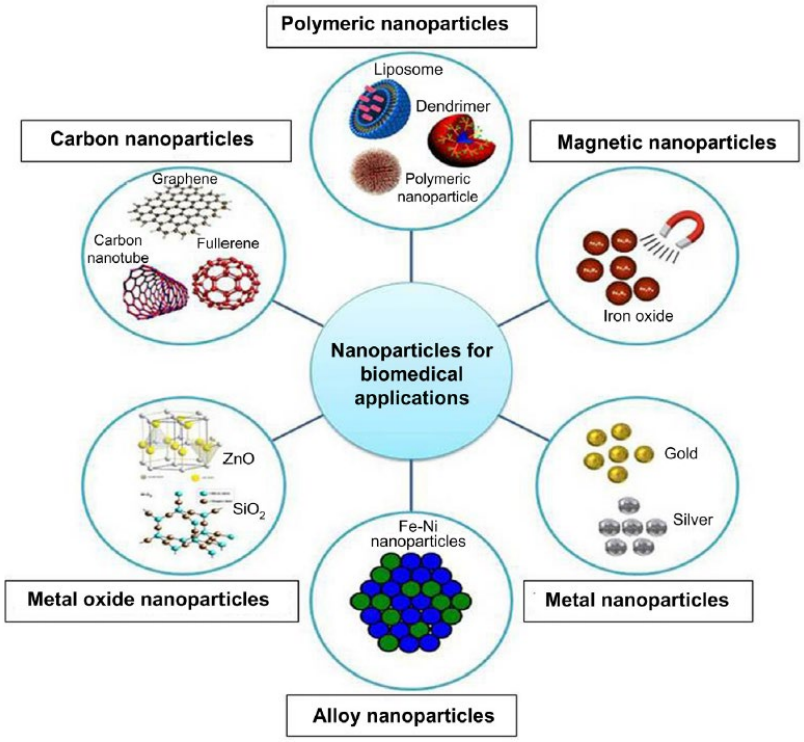

Figure 1-1: Various types of nanoparticles used in biomedical applications [1]

Among nanomaterials, metallic nanoparticles, including gold and silver, owing to their superior chemical, physical and optical properties, have been investigated in bio-applications such as bacteria detection, antimicrobial, and antiviral approaches [13].

Gold is a noble metal with high resistivity against corrosion, oxidation, in vivo degradation [14], and other chemical reactions. Additionally, excellent biocompatibility, low toxicity, high surface-to-volume ratio, easy handling and fabrication, tunable electrochemical properties, and remarkable optical and thermal properties make gold and gold nanoparticles (AuNPs) an ideal material to be used in bio-nanotechnology [15, 16]. Drug delivery and gene delivery systems [17], biosensors and diagnostic devices [18], imaging, and therapeutic approaches [19, 20] are various biomedical applications using different size and shapes of gold nanoparticles and gold nanoparticle-based platforms.

Surface plasmon resonance (SPR) is an optical phenomenon occurring by the incidence of light on the metals' surface, such as gold and silver, and their surrounding medium interface. The interactions of the electric field in the incidence light and the conduction electrons near the surface of the metal sets a collective oscillation of these conduction electrons. These oscillations are quantized, with each quantum known as a plasmon. When the wavelength of the light excitation

is on the order or larger than the metal object being irradiated (a nanoparticle), the plasmons are localized over the surface of the nanoparticle; thus, it is termed localized surface plasmon resonance (LSPR). Au and Ag NPs are among the best materials to demonstrate large LSPR. Due to this characteristic, these metallic NPs are employed in many applications, particularly optical diagnostic biosensors [21, 22]. Various gold nanoparticles-based biosensing platforms using the LSPR effect have been developed for detecting a broad range of biomolecules and disease-causing microorganisms such as bacteria and viruses [23–25].

Silver nanoparticles (AgNPs), on the other side, are the next most popular metal nanoparticles having unique chemical, physical, and biological properties, which offer great potential in widespread biomedical applications such as surface modification, drug delivery systems, diagnostic probes, and imaging devices [26]. However, the antimicrobial and antibacterial effect is the most prominent characteristic of the silver nanoparticles that have been extensively exploited in medical products, the food industry [27], cosmetics [28], textile production [29], and environmental approaches [26, 30, 31]. AgNPs as antimicrobial agents have demonstrated promising effects on deactivating a broad variety of bacteria [32], viruses [33, 34], and fungi [35].

According to WHO, infectious diseases caused by pathogenic microorganisms annually trigger the death of almost 17 million people worldwide. Therefore, detection and decontamination of the root cause of the infections have always been a priority for bio-scientists and health care providers [36]. The recent global outbreak of SARC-CoV-2, the cause of the illness known as the COVID-19, revealed the restriction in resources and incapability of the healthcare systems to control the spread of such an infectious virus and reduce its mortality rate [37]. Various decontamination approaches and sanitizing chemicals such as peroxides, chlorines, and alcohols are utilized to curb the spread of the virus. However, despite their fulfilling results, chemical disinfectants face some limitations, including lack of long-term effectiveness, the need for highly concentrated products for complete sanitization, and the risk for adverse impact on the health and environment. This is compounded with the fact that vaccination against a newly emerged viral pandemic necessitates a long-time research and sound investigation, which requires the dedication of significant financial resources by government and private investors alike [38].

On the other hand, current advances in nanotechnology propose a potential efficiency of employing nanomaterials in both disinfecting and diagnosis of COVID-19. Taking these factors

into account, it is possible to develop antibacterial and antiviral nano-based products for disinfecting different surfaces and enable reliable personal protective equipment (e.g., face mask) to efficiently and accurately exterminate this lethal virus to resolve this global crisis [37].

Toward this end, specially designed gold and silver NPs with unique properties have received significant attention [39]. In addition, interest deepened in novel approaches and/or improving current methods for the synthesis of colloidal gold and silver NPs. AuNPs and AgNPs are commonly synthesized through conventional liquid chemistry techniques, biological, and green synthesis methods [40, 41]. Turkevich method is the most popular method used for the synthesis of colloidal NPs, which involves using citrates acting both as reducing and stabilizing agent for forming NPs. For example, for synthesis of AuNPs, sodium citrate is added to a boiling solution of gold hydrochloride (as the metal precursor) under vigorous stirring to complete the reduction reaction. This method usually extra requires steps of purification and size selection of the NPs in order to obtain monodispersed particle size. Techniques such as centrifugation or dialysis are employed for this purpose. These time-consuming processes also result in the consumption of a large amount of materials, organic solvents, and energy which adds up to the end cost of the NPs [19]

That is one of the reasons why monodispersed particles having a small size distribution (less than 2 nm) tend to be extremely expensive. For example, 1 gram of AgNPs powder with a random size distribution of <100 nm costs about US$ 13.50 (sold by Sigma Aldrich in 5g quantity and costs US$ 68.20). On the other hand, a 25ml suspension of 0.02 mg/ml of AgNPs having the size of (10+4) nm costs US$ 132, according to Sigma Aldrich. A simple calculation based on such information puts the cost of 1gram of dried particles at US$ 284,000. Finding alternative synthesis of uniform AgNPs that lower this cost significantly will have a direct impact on the market penetration of such important nanomaterials.

Nevertheless, self-assembly of monodispersed NPs array structures, including functional periodic structures or broad-range ordered thin-films of NPs (e.g., AuNPs), are important for many applications ranging from chemical and biological sensors to diffractive optical devices [42, 43] to solar cells [44].

The unique features of the nano-scaled structures, including the size and shape of the constituting nanoparticles, can have a remarkable impact on the electronic and optical properties. However,

their cost of manufacturing still remains relatively high for widespread use. Therefore, it is imperative to innovate new approaches to NPs synthesis that enable low-cost fabrication of well-defined self-assembled array structures and have a low carbon footprint. Among various fabrication techniques, solution-based thin-film coating procedures are promising low-cost methods to fabricate metallic NPs on various substrates for a broad spectrum of applications in industry, scientific research, and biomedical devices, for example, the LSPR or SPR based biosensors [45, 46].

Conventionally, to deposit thin films of NPs, for instance, the AuNPs or the AgNPs, a standard solution-based chemistry (bottom-up) technique must be used to synthesis the NPs, followed by size-selective steps to reduce the variation in NPs diameter to an acceptable range for a given application. Additional steps during the chemical synthesis process may be called upon if the surface of the NPs is to be functionalized with certain ligands to suit a target application or obtain a colloidal solution of NPs. Obtaining highly ordered thin films of NPs might call upon substrate surface functionalization. For example, the immersion of the thiol or amine-functionalized substrates into a gold nanoparticle-containing suspension results in covalent attachment of the nanoparticles to the surface and subsequent formation of the uniform thin film [47, 48]. However, the colloidal solution of the NPs can be cast into thin films using a myriad of liquid-based deposition techniques such as dip coating, spray coating, printing, etc. [49].

The above-mentioned fabrication methods of thin films of NPs require the use of colloidal solutions of pre-synthesized metal NPs and functionalized substrate surface if ordered NPs films are needed. The multistep chemical consuming and environmentally unfriendly traditional chemical route to NPs synthesis, along with the extra steps to obtain ordered thin films of NPs (as mentioned above), makes this approach expensive and hampers its adoption in the mass market.

Jabbour's group has introduced a one-step reactive inkjet printing that is capable of not only in-situ self-assembly of metallic NPs, but also impart the NPs with surface functionalization to prevent their coalescence, thus maximizing size uniformity, stability, and positional order of the NPs within the thin film. In this reactive printing approach, the inks constituted commercially available precursors and agents, which were used with more than 99.5% efficiency, making the process with virtually zero environmentally hazardous byproducts. It is worth mentioning that the

group optimized this process to yield highly uniform NPs films in a record time of just 1 minute [50, 51].

A 20-hour size-selective deposition of pre-synthesized NPs (nano disks) has been demonstrated by Zhang et al. [52]. The drawbacks of this approach are its long processing time and the fact that NPs must be made prior to the deposition process. In-situ synthesis of AuNPs embedded in flexible polydimethylsiloxane (PDMS) film has also been demonstrated. In this case, the curing agent acted as both the hardener of the polymer and the reducer for the metal salt upon casting the mixture of the silicone elastomer, curing agent, and the metal precursor on a glass slide substrate, with no need of adding an external reducing or stabilizing agent. The film has potential for applications in optical and biomedical sensors. However, this technique is only suited for PDMS and cannot be used to extract the synthesized NPs economically, nor arrange them in highly ordered structures needed for many applications as mentioned above [53]. Ahmed et al. reported a simple one-step process that involves immersion of the substrate of any hydrophobic or hydrophilic glass, PDMS, or polystyrene into the reaction solution consisting of a mixture of the Au precursor and the reducer agent, which resulted in nanoparticles a diameter of 30-40 nm [42]. Although a simple one-step approach, the shelf lifetime of the combined ink is limited as the reaction that results in the formation of NPs is short-lived, thus rendering the ink into a colloidal solution of NPs of various sizes. The reactive inkjet process mentioned above was capable of preserving the starting components for months in storage without any formation of NPs. However, when both starting component inks were printed on top of each other in a controlled manner, self-assembled AuNPs with relatively uniform size distribution in the range of 8±2 nm, smaller than those produced by conventional colloidal techniques (15±2 nm), was demonstrated on glass and silicon substrate using a reactive inkjet printer [54]. Although inkjet printing is suited to roll-to-roll (R2R) manufacturing process, it is still expensive due to the high price of printing cartridges that have the tendency to clog over time, thus increasing the production costs of NPs. To mitigate this, a faster and commercially viable reactive printing approach must be put in place to meet the needs of low cost and enable widespread use of NPs with uniform size distribution. This can only be done through roll-to-roll compatible approaches such as blade coating, gravure printing, and slot die coating, to mention a few. A R2R (or sheet-to-sheet for hard rigid substrates) system is a continuous process in which a flexible substrate (or rigid) is passed at high speed (can reach 60

km/hr) to receive on its surface various materials deposited sequentially down the line to form in a multilayer coating structure [55, 56].

In this study, blade coating was selected due to its application as a potential in roll-to-roll manufacturing of NPs, Figure 1-2. For the first time, to the best of my knowledge, I will demonstrate not only the synthesis of AuNPs using reactive coating approach that yields NPs with uniform size distribution but also layers of ordered metal NPs over the substrate surface. This low-cost process could lead to drastic cost reduction in the price of NPs if successfully transferred and adopted by industry.

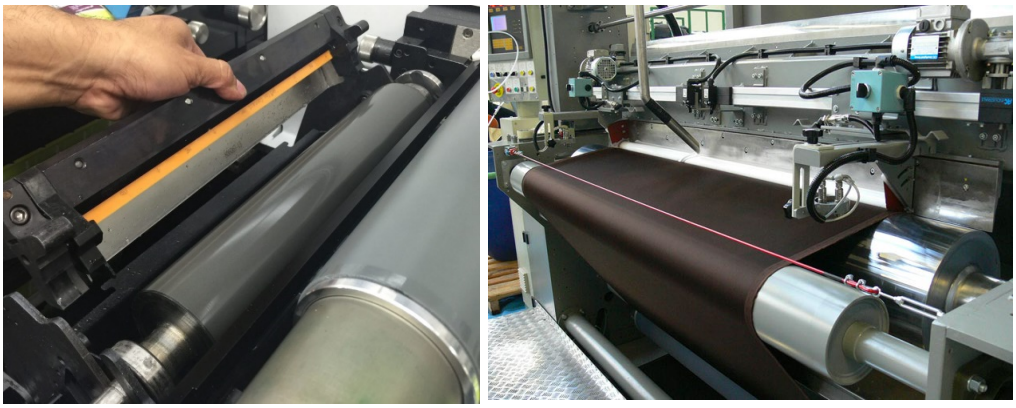

Figure 1-2: Roll-to-roll blade coating [57, 58].

Here, reactive blade coating was carried out using oleylamine as both the reducing and stabilizing agent for Au and Ag precursors. To examine the impact of the solvent on the coating process and shape and size distribution of the resulting NPs, different organic solvents were utilized in the preparation of both reducer and precursor ink solutions.

Considering the above, the main objectives of this z by blade coating process and optimize the uniformity and stability of the film.

1) Explore in-situ self-assembly of AuNPs and AgNPs by the low-cost, roll-to-roll compatible reactive blade coating process.
2) Investigate the behavior of various organic media used as ink components during the blade coating process and assess their impact on the uniformity of the film coating and NP size distribution.

3) Demonstrate two potential biomedical applications of the synthesized NPs, namely, examine the capability of the self-assembled AuNPs as LSPR glucose biosensor, and investigate the antiviral activity of the synthesized AgNPs, and coatings thereof. A particular aim was the impact of reactive blade coated AgNPs on disinfecting the coronaviruses using a surrogate virus (of the same family as SARS-COV-2).

The following chapters outline the different aims of this project, as they are described below:

Chapter 2 presents a brief overview of AuNPs and AgNPs, the NPs synthesis routes, thin-film deposition techniques, and applications of AuNPs in various biosensing platforms, particularly LSPR-based biosensors. The application of AgNPs as an antiviral agent is briefly reviewed as well.

Chapter 3 describes the fabrication process of the AuNPs thin films via the reactive blade coating process and the materials consumed for synthesizing the self-assembled AuNPs. The chapter also includes the characterization techniques, results, and their analysis. The biosensing activity of the AuNPs by utilizing their LSPR effect is also presented in this chapter.

Chapter 4 initially begins with a description of the fabrication process of self-assembled AgNPs using reactive blade coating, characterization of the coatings, results, and conclusion. This is followed by a discussion of the potential antiviral application of such coatings against the coronavirus, as supported by the results from the antiviral efficacy of the AgNPs as observed in plaque-forming unit (PFU) measurements performed at uOttawa biosafety level 2 facility.

Chapter 5 presents the overall conclusion of the reactive blade coating fabrication of self-assembled metallic nanoparticles and their prospective future applications for detection and deactivation of disease-causing pathogens, which can lead to addressing the current pandemic of COVID-19 or related possible infections.

Chapter 2. Background

2.1 Gold nanoparticles

Gold nanoparticles (AuNPs), owing to their unique chemical and physical characteristics such as stability and multifunctionality, have received tremendous attention on both fronts of synthesis and applications [16]. Apart from their superior chemical stability, which makes them perfect for bio-nanotechnology applications, AuNPs morphology and size-dependent optoelectronic properties are also significant characteristics of these particles. For example, a broad range of colors can be observed in a colloidal solution of AuNPs by enlarging the size of the particles from 1 to 100 nm [19]. This size-dependent color change upon incident light on the metallic NPs is due to the surface plasmon resonance (SPR) phenomenon. SPR is an optical effect arising from the interaction of conduction electrons of the metal nanoparticles with the electric field of the incident photons leading to collective resonant oscillations of the conduction electrons [21]. Such characteristics are magnified greatly in AuNPs and AgNPs, enabling their use in optical-based diagnostic platforms discussed further in section 2.3.7.

2.1.1 Synthesis of gold nanoparticles

Gold nanoparticles are fabricated mainly via two methods: 1) top-down, and 2) bottom-up. In the top-down approach, techniques are mostly physical, and gold in a bulk form is broken down to fine nano-sized particles using different methods, including metal grinding, mechanical milling, thermal decomposition, laser ablation, sputtering, and lithography, such as electron-beam lithography and nanoimprint lithography. However, such methods require sophisticated fabrication equipment and are limited in their application to thin-film applications and small sample sizes [59]. On the other hand, it is possible to bring gold atoms together to form tiny particles, having nanometer dimensions, using chemically based techniques. This is the bottom-up approach and the most popular due to its relatively low cost and versatility in functionalizing the NPs during synthesis. Some of the leading bottom-up approaches described in this chapter include the Turkevich method and green methods [19].

2.1.1.1 *Chemical methods*

Wet chemical synthetic methods (e.g., Turkevich method) remain the dominant approaches to the synthesis of AuNPs and AgNPs. Among various methods, chemical reduction of metal precursors

is the most broadly utilized approach used for colloidal AuNPs and AgNPs production. The main mechanism behind the formation of the metal NPs when using wet chemistry includes two stages of nucleation and growth. This process mostly involves chemical reduction of metal precursors and comprises three main components, (1) a metal precursor, (2) reducing agents, (3) stabilizing agents. As it is shown in figure 2-1 the process initiates with the reduction of metal ions resulting from dissolution of the metal salt (here AgNO3) by means of a reducing agent. The next step is nucleation by aggregation of some atoms to form clusters of atoms called nuclei. This is followed by the growth of the clusters and their coalescence to form nanoparticles [60].

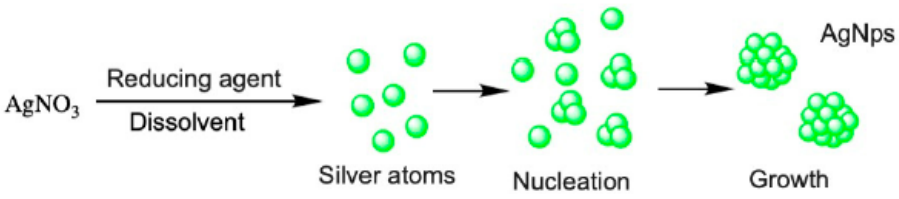

Figure 2-1: Process for the synthesis of AgNPs [60].

Altering the experimental parameters, such as the type and concentration of precursor, reducing agents, pH, and temperature, can impact the average size, polydispersity, and shape of resulting NPs. Moreover, the stabilization stage plays a key role in the synthesis of NPs as it empowers the NPs to withstand agglomeration and oxidation processes. In addition, capping agents can assist in the formation of small particles that can act as seeds for further growth of NPs, as it shown in figure 2-2. Moreover, smaller particles, due to higher solubility, according to Ostwald ripening phenomenon, re-dissolve into silver (or gold) ions which are reduced and deposited on the larger particles to make them grow even more [61]

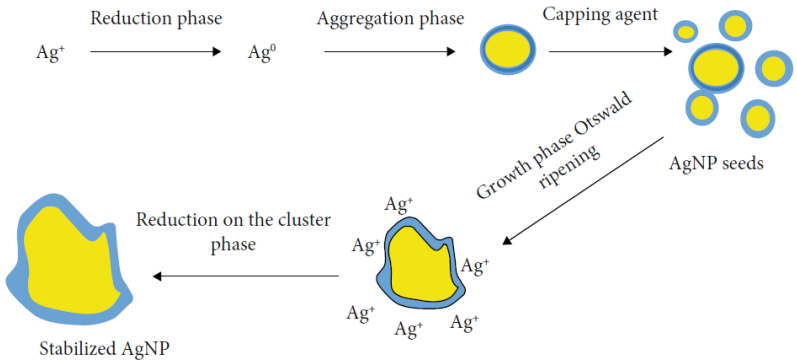

Figure 2-2: Representation of the nucleation and growth mechanism for AgNPs [61].

Chemical synthesis of gold nanoparticles occurs in a liquid phase composed of Hydro chloroauric acid (HAuCl4) as the gold precursor, hydrogen peroxide, or sodium citrate as reducing agents, and amines, thiols, and surfactants as stabilizing agents. First, the HAuCl4 is dissolved. Then, the $Au3^{+}$ ions are reduced to neutral atoms by a reducing agent acting as an electron donor. The next step is stabilization to stop NPs from aggregation. By adding the stabilizing agents, a repulsive force is created on the surface of the NPs to make them dispersed. This stabilization process could also control the shape and size of the AuNPs. Sometimes, one material can have a dual role as the reducing and stabilizing agent, such as the case with citrates [40, 57].

- *Turkevich method*

The Turkevich method is a well-known chemical method that is frequently used by researchers to synthesize AuNPs. In this method, which was first introduced by Turkevich in 1951 [62], $HAuCl_4$ was used as the precursor and trisodium citrate as both the reducing and capping agent (figure 2-3.a). The synthesis occurs when the solution is heated to boil accompanied by vigorous stirring. A wide range of various sizes of spherical AuNPs from 1nm-50 nm can be generated by slightly changing the $HAuCl_4$/citrate ratio and controlling the pH and temperature. Red-colored colloids of AuNPs are mostly produced through this method [40].

- *Burst-Shiffrin*

Another chemical method frequently used to fabricate AuNPs is that of Burst and Shiffrin, which was first published in the 1990s (figure 2-3.b). Organic liquids that are not miscible with the aqueous phase are mainly used here. $HAuCl_4$ aqueous solution is firstly mixed with tetraoctylammonium bromide (TOAB) dissolved in an organic solvent like toluene. Here, TOAB acts as a phase transfer catalyst to transfer $AuC1_4$ from an aqueous solution to an organic toluene solution. Then an alkylthiol (dodecanethiol) as a stabilizing agent is added to the organic phase.

The Au is then reduced with the addition of sodium borohydride $NaBH_4$ as an electron donor under vigorous stirring. Particles of 2.5 nm is produced by this method. [57, 59].

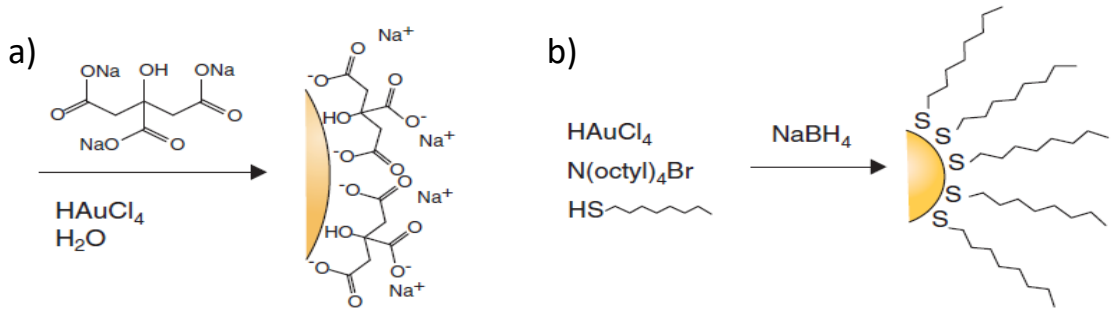

Figure 2-3: Scheme of a) using citrate as both reductant and capping agent for generating AuNPs by Turkevich method, and (b) AuNPs capped with thiols by Brust method [14].

- *AuNPs synthesis using Oleylamine*

In addition to the previously mentioned techniques, AuNPs can be produced in an organic medium by using Oleylamine (OA, $C_{18}H_{35}NH_2$) as both reducing and capping agent, and Au precursors such as NaAuCl4. Oleylamine consists of 1) an amino group that performs as an electron donor at elevated temperatures, e.g., 80ºC, for reducing Au^{3+}, and 2) a long hydrocarbon chain that contributes to the stabilization of AuNPs [64]. Figure 2-4 shows the steps of the formation of the gold nanoparticles using this approach.

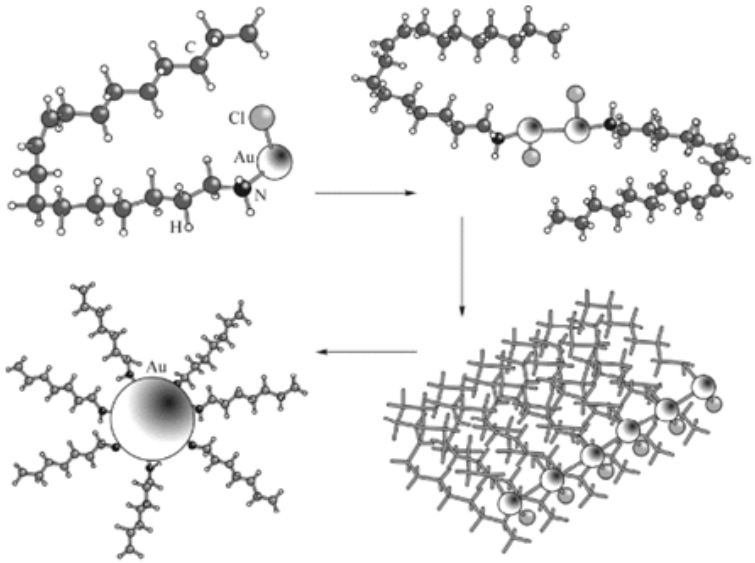

Figure 2-4: Scheme of steps of forming AuNPs from a reaction between the Au precursor and oleylamine. a) AuCl-oleylamine complex formation, b) dimers/trimers formation, c) long chains formation from dimers, and d) formation of gold nanoclusters with surface ligands [64].

- *Seed growth*

Despite the Turkevich and Burst-Shiffrin methods that produce spherical AuNPs, the seed growth method can synthesize various shapes of AuNPs such as cubes, rods, and tubes because of anisotropic growth of the seeds. In this method, with the help of NaBH4, HAuCl4 is first reduced to produce seeds of Au. The seed particles are then mixed with a weak reducing agent such as ascorbic acid, along with a structure-directing agent, to prevent further nucleation and aggregation of the seeds and consequently control the particles' geometries [61, 62].

2.1.1.2 *Green synthesis method*

Several plant-based substances, as well as biopolymers, have been utilized for the green synthesis of AuNPs. Using such materials allows the production of metal NPs in an environmentally friendlier approach than those described above. Thus, the name green synthesis. Various plant extracts such as coconut oil, palm oil, and biopolymers, including chitosan, gelatin, collagen, have been used to prepare AuNPs by reducing HAuCl4 [40].

2.1.1.3 *Biological synthesis*

AuNPs also can be produced in one of the most environmentally friendly approaches using microorganisms, including bacteria, fungi, yeasts, and algae, which lends such technique a higher biocompatible nature. Biological synthesis of AuNPs can occur either intracellularly, resulting in polydisperse particles with specific dimensions, or extracellularly producing monodisperse and purer nanoparticles. In the extracellular method, no further treatment and cleaning process is required as the nanoparticles are produced from cellular constituents such as the reductive enzymes secreted out from the cell or the cell wall. Thus, the particles produced extracellularly tend to be more useful in biomedical applications as they are ready to be utilized directly after synthesis. Although biological synthesis as an eco-friendly production method is always favorable, such approaches face certain difficulties, including precisely control the shape and the size of the AuNPs and scaling up the production to an industrial level [63, 64].

2.1.2 Self-assembled thin-film nanostructures

Apart from the colloidal metal NPs that can be used in various applications, self-assembled nanoparticle thin-films are among critical technologies and have been the subject of interest in multiple applications such as biomedical and energy industries, including chemical and biological

sensors, diffractive optical devices, solar cells, organic photovoltaics and conductive thin-films [69]. Metallic nanoparticle films, including AuNPs, as functional periodic structures are among the major examples of these self-assembled particle arrays developed for a variety of purposes [70].

Electronic and optical properties of metallic thin films such as AuNPs coating are affected by the shape, size, and packing of the particles. Therefore, the synthesis of the nanoparticles and fabrication process of the thin-film structure can significantly impact film properties [71]. Consequently, choosing a proper fabrication method and optimizing the fabrication conditions are critical factors to be considered. Solution-based thin-film deposition techniques are fast, simple, and low-cost that have been excessively applied in various applications in industry, scientific research, and biomedical devices. All in all, diverse thin film deposition techniques can be used to deposit AuNPs on different substrates [72].

2.2 Thin-film deposition

Thin-film deposition, both large-scale, and small-scale manufacturing has been excessively performed via coating techniques. Due to its economy of scale, a roll-to-roll (or sheet-to-sheet) deposition system is most promising for low-cost deposition of NPs into thin films. A Roll-to-roll deposition approach is a continuous process in which a flexible substrate is passed between large rollers, and deposition can take place in subsequent steps to form multiple films and layers. The substrate speed can be more than 50 km/h allowing for the deposition to happen at a less energy and materials consumption (thus less cost) than using traditional coating methods such as dip coating, vacuum, and others. Thus, a large-scale technology that is compatible with the roll-to-roll and continuous deposition process of NPs is considered to be ideal for mass production on an industrial scale [55]. Roll-to-roll techniques are widely used in the printing of newspapers, billboards, logos, RFIDs, and circuit boards, to mention a few. Here we will briefly describe some of the printing methods that can be used in the fabrication of thin films of NPs.

2.2.1 Printing techniques

By printing, we mean a direct transfer of a shape or pattern unto the substrate during the deposition process. In this case, both deposition and patterning of the materials occur simultaneously. Some of the scalable roll-to-roll processes compatible printing techniques include screen printing,

gravure printing, flexographic printing, and inkjet printing. In screen printing, a pre-patterned screen mesh is used to transfer (print) a pattern of ink unto the substrate (figure 2-5 (a, b)). This approach has broadly been used for developing biosensors and fabricating electrochemical electrodes using organic and inorganic materials, including gold nanoparticles [73]. Gravure and flexographic printing techniques, displayed in figure 2-5 (c, d), are among the most used roll-to-roll printing methods, in particular, in newspaper production. Here, single or multiple engraved rotating cylinders transfer the patterned ink to the surface substrate. In the above two processes, the substrate achieves momentarily contact with some of the printing elements (for example, contact with mesh in screen printing and anilox roller in gravure) [74].

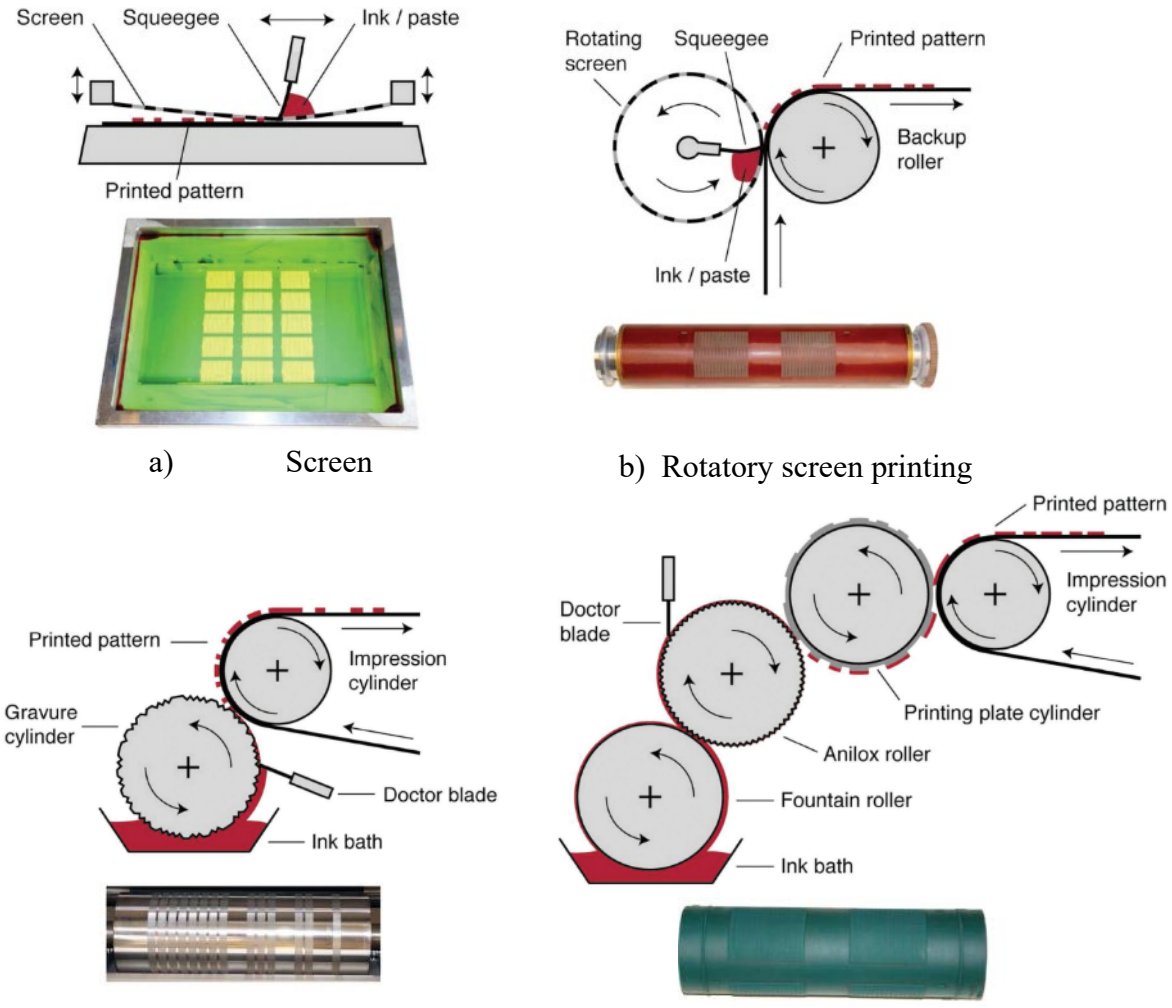

Figure 2-5: Large scale roll to roll printing techniques [73]

On the other hand, the roll-to-roll compatible inkjet printing is a non-contact deposition technique which is capable of precise on-demand positioning and patterning of liquid materials at desired locations over the substrate surface and almost 100% use of formulated inks, thus leading to the very low carbon footprint. The combinatorial capability of such techniques also allows for rapid discovery and optimization of materials and thin-film structures. Moreover, inkjet printing is an additive printing technique with high precision, high resolution, and reproducibility. These attributes make it ideal for the advanced manufacturing of NPs and other multifunctional materials and devices. In this regard, it has been widely used in electronics, photonics, and biomedical applications [75]. As shown in figure 2-6, ink in the form of tiny droplets propels through the nuzzle and deposits unto the substrate. Inkjet printing takes place in two different modes of continuous jet or drops-on-demand process using thermal or piezoelectric actuators to push out the drops through the nozzle head. The resolution of features printed by inkjet varies from 30-50 µm using single or multi nozzles print heads. The printing speed depends on the number of functioning nozzles. Rapid and high volume production is feasible using series and parallel arrangements of nozzles and print heads [69, 70]. Among several factors affecting the inkjet printing process, viscosity and rheology of the ink are critical, and they must be well-controlled to avoid the clogging of the printhead in order to achieve a successful printing run. Inkjet printing, figure 2-6, has been applied in the design and fabrication of electrochemical electrodes for use in electrochemical biosensors. In this case the ink is made up of electroconductive materials, such as colloidal solution of AuNPs [76].

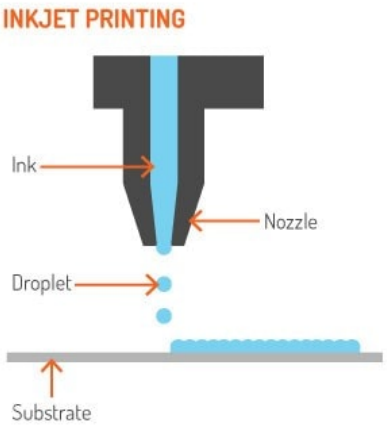

Figure 2-6: Schematic illustration of drop-on-demand inkjet printing [76]

2.2.2 Coating techniques

Although there are numerous coating techniques, we will limit our discussion to a few of them, namely spin, spray, dip, and blade coating.

2.2.2.1 *Spin coating*

One of the standard techniques used for thin film deposition of liquids is spin coating. Deposition can occur in either a dynamic mode when the substrate spins during the deposition process or a static mode that the substrate starts to rotate after the introduction of the liquid material (figure 2-7.a). Centrifugal force will result in the formation of a thin film over the substrate surface. The rotation speed and time, solution viscosity, and solvents used are some parameters that define the final thickness of the film. The rotational requirement of this technique limits its applications to individually cut substrates, thus rendering this technique useless in high-speed roll-to-roll additive manufacturing [77]. On the other hand, spray, dip, and blade coating are highly compatible with roll-to-roll manufacturing.

2.2.2.2 *Spray coating*

In spray coating, pressurized air or gas or an ultrasonic system is used to break the solution into a flow of fine droplets, which are continuously dispensed and deposited on the substrate (figure 2-7.b). Many variables play an integral role in determining the final quality of the coating, including the ink surface tension and viscosity, gas flow, nozzle dimensions and distance to the substrate, and spraying speed, to mention a few [78].

2.2.2.3 *Dip coating*

In this technique, the substrate is immersed in the solution, and then it is removed at a constant speed. During immersion, the solution wets both surfaces of the substrate. The coating is obtained upon the removal of the substrate from the liquid bath at a controlled speed (Figure 2-7.c). The factors determining the quality and thickness of the thin film coating include solution viscosity, solvent evaporation rate, airflow, and substrate withdrawal speed [77].

2.2.2.4 *Blade coating*

Doctor blade coating (DCB) is a deposition technique that has widely been used in large-scale thin-film production and various applications such as textile, printing technologies, ceramic

industries, medical patches, and solar cell manufacturing [70]. In this technique, the liquid (ink) is placed on the substrate in front of the doctor blade, as shown in figure 2-7.d. A thin film is obtained upon the blade movement, which results in leveling the ink to the desired layer thickness as dictated by the distance between the blade and the substrate, speed, and angle of the blade, viscosity and evaporation rates of the liquid components of the ink, to mention a few [79].

In addition to the passive deposition of materials, blade coating has been used in the fabrication of filtration membrane, full-color displays, and diffractive optics as well as the synthesis of 3D highly ordered structures of various nanocomposite materials, including colloidal crystal-polymer nanocomposites and microporous polymers [70].

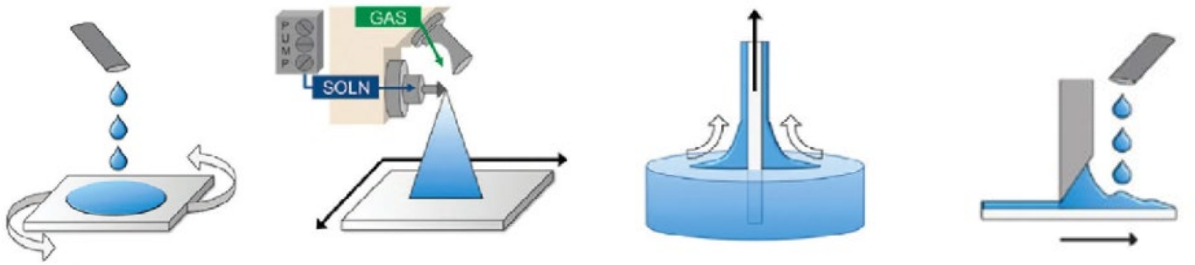

Figure 2-7: Coating techniques used for thin film deposition [80]

2.2.3 Printing approach to *in-situ* synthesis of gold nanoparticles

Solution-based thin-film deposition of NPs has conventionally involved the use of pre-synthesized NPs hosted in a liquid medium. In the case of AuNPs, a colloidal solution is used in such deposition processes. The AuNPs must be made first using traditional wet chemical methods followed by their purification (including size uniformity), and finally dispersing the NPs in an organic solvent to form the deposition inks. However, in a more facile and faster way, functional materials can also be synthesized *in-situ* and patterned simultaneously on the substrate surface. Reactive deposition, such as reactive inkjet printing [54], refers to the process by which, for example, the gold nanoparticles synthesis, thin-film, and patterning all occur on-demand and at specified locations over the substrate surface. The inks, in this case, consist of 1) Au precursor ink and 2) a reducer ink. Such an approach leads to a more convenient, simpler, and faster one-step direct fabrication of the AuNPs thin films on varied substrates. The additional advantage of reactive

coating includes less material waste and energy consumption and the shorter production process as the final fabrication takes place at the same time as the synthesis of the NPs [77, 78].

2.3 Biomedical applications of AuNPs

There has been an ever-growing use of nanotechnology and nanomaterials in diagnostics and therapeutics in the past decade. Gold nanoparticles, owing to their outstanding photochemical, electrical, and optical properties, have been exceedingly utilized in numerous areas, including drug delivery [83], therapy and cancer cells destruction procedures [84], disease detection and diagnostics[81, 82], and biosensors [67].

2.3.1 Gold nanoparticle-based biosensors

Considering remarkable advances in technology and medicine in recent decades, there is an ever-growing demand for rapid, low-cost, precise, and point-of-care diagnosis of diseases and serious health conditions [87]. As a result, biosensors, capable of detecting chemicals and biomolecules causing diseases, have been abundantly developed toward this end. Biosensors, generally, provide a platform that consists of a bioreceptor for interacting with the analyte, a transducer for generating a detectable signal from that interaction, and a signal processing system to interpret the detected signals. A wide variety of bio-sensing platforms based on multiple types of detectable signals can be fabricated, ranging from electrochemical to optical biosensors [88]. Since the first introduction of the electrochemical glucose biosensor by Clark and Lyons in 1962, various approaches have been studied to develop sensing platforms with higher sensitivity, lower price, less detection time, and higher limit of detection LOD [89].

With the advent of nanotechnology, nanomaterials have gained significant attention in designing and fabricating bio-sensing devices. Among metal nanoparticles, AuNPs, have been tremendously used in diverse biosensors due to their excellent biocompatibility, high surface energy, high surface-volume ratio, electroconductivity, and exceptional light-scattering properties [90]. Chemical or physical changes that occur as an outcome of the analyte-receptors binding can produce electrical, optical, or qualitative measuring transduction signals depending on the type of AuNPs-based biosensors. Figure 2-9 illustrates multiple chemical and physical properties of AuNPs used for different detection modalities and methods of AuNPs-based biosensing probes.

Colorimetric assay, optical, electrochemical, and piezoelectric biosensors are examples of diagnostic measures utilizing AuNPs, which are briefly reviewed in the following sections.

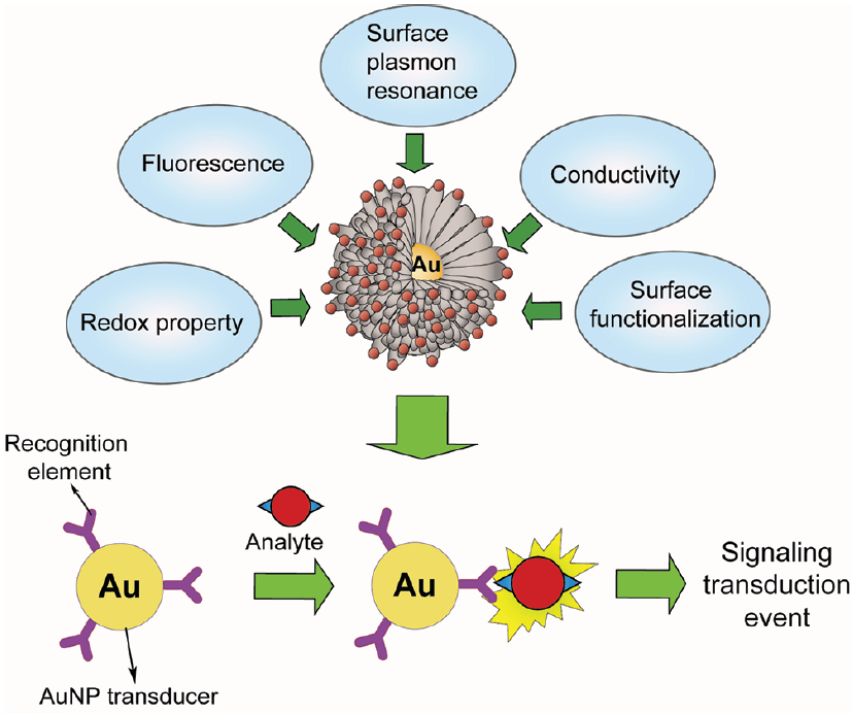

Figure 2-8: Physical properties of AuNPs used for various sensing methods and schematic illustration of an AuNP-based detection system. Unique properties of AuNPs, such as conductivity, surface plasmon resonance producing ability to quench (or enhance) fluorescence and catalyze reactions, enable their broad applications in various sensing approaches [91, 92].

2.3.2 Electrochemical GNP-based Biosensors

The superior properties of AuNPs, including their high surface area, high conductivity, and catalytic properties, have made them an excellent candidate for electrochemical and electrocatalytic sensors for the detection of numerous analyte materials. AuNPs allow electron conduction; hence, they can easily transfer the electron between the immobilized redox protein and the sensor's electrode material [93]. Gold nanoparticles can be deposited on the electrodes to promote the immobilization and binding of the enzymes specific to different analytes, such as glucose oxidase, which are required for the recognition of those analytes. [94]. Furthermore, immunosensors provide a highly sensitive and selective biorecognition based on antibody-antigen interaction. The application of gold nanoparticles as biosensing platforms not only supports the bioactivity of the biomolecules due to the biocompatibility of the AuNPs, which is vital to the sensors' functionality, but it also improves the electrochemical signal [95].

DNA sensors, offering a rapid, reliable, and affordable pathway for DNA sequences diagnosis, are another type of electrochemical sensors that substantially have been developed for the diagnosis of genetic disorders. It is easy to functionalize the AuNPs with oligonucleotides, which makes them excellent to be used in DNA biosensors. The AuNPs can also mediate the transfer of electrons to the electrode, which amplifies the signal production. Moreover, the AuNPs contain thousands of oxidizable or reducible gold atoms by which can increase the generated signal. AuNPs also can be exploited to enhance the sensor stability and the detection limit through the surface modification of the electrochemical electrodes [96].

2.3.3 Piezoelectric Biosensors

The piezoelectric response is the basis of the piezoelectric sensors in which an electric signal is generated when a mechanical force is applied to the piezoelectric material. Quartz crystal is the most popular material used in piezoelectric biosensors with high sensitivity. Various analytes such as cells, bacteria, genes, proteins, and toxins are detectable when the mass changes due to their presence on the surface of the quartz crystal. A shift in the resonance frequency, consequently, can be detected. Due to the high specific surface area, AuNPs can increase sensor sensitivity by providing more biding sites for the biomolecules [97]. Moreover, AuNPs can act as labels due to their contribution to signal amplification because of their high density, which enhances the mass on the surface of the quartz crystal [98].

2.3.4 Colorimetric Biosensors

Gold nanoparticles can represent different colors in diverse sizes and shapes, as well as different aggregation states. When adding the analyte, the color of the colloidal solution changes. This is due to either aggregation or dispersion of the AuNPs. Various kinds of colorimetric biosensors have been produced based on this color change effect [91]. Changing the distance between AuNPs or binding the analyte to the surface of the particles causes the change in the color of the gold nanoparticle solution and its characteristic plasmonic peak wavelength. Colorimetric sensing based on AuNPs is used for the detection of heavy metals, pesticide residues, banned additives, and biotoxins in food. [99]. Ferhan et al. have developed an AuNPs based colorimetric sensing platform that showed sensitivity to the lead ions. Functionalized AuNPs were loaded into poly (oligo-ethylene glycol) methacrylate -POEGMA- brushes coating the substrate. Figure 2-9.(a) illustrates how by adding Pb^{2+}, Au-Pb alloy is formed, and subsequently, it is released from the

surface. The bluish color of the coated substrate fades as the lead ion concentration is increased [100]. Moreover, a biosensor for the detection of H_2O_2 was developed based on AuNPs aggregation mediated by cysteine. According to figure 2-9.(b), oxidation of cysteine to cystine by H_2O_2, and subsequently, aggregation of AuNPs due to the H-bond formation and electrostatic interaction among the particles, could result in the color change. This process was the basis of the sensing strategy used for detecting H_2O_2 and consequently sensing glucose, as H_2O_2 is produced through oxidation of glucose by GOx [101].

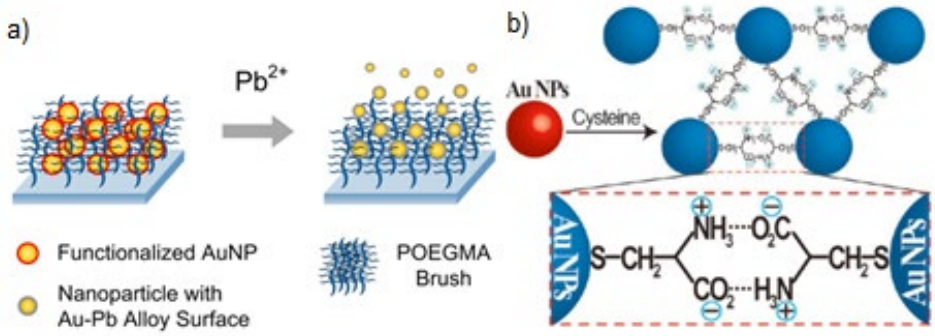

Figure 2-9: (a) Schematic of Au NP-based colorimetric sensor for lead detection. (b) Cysteine-mediated colorimetric detection [99].

2.3.5 Optical biosensors

Optical biosensors have shown promise in biological detection, drug discovery, food safety, and environmental monitoring with high sensitivity, reliability, and processability. Various modalities of optical biosensing are employed for bio-detection. Metal nanoparticles have an integral role in these methods. Optical biosensors operate based on any alteration that occurs in reflected light as a result of the presence of an analyte. The plasmonic properties AuNPs in response to incident external electromagnetic radiation provide an extensive range of optical sensing applications [102]

Surface plasmon resonance (SPR) is a phenomenon that occurs on metal thin-film substrates because of the interaction between the conduction electrons and incident light at the metal surface interface. This interaction at the metal film surface excites surface electromagnetic waves and generates resonance with the incident light wave, leading to absorption of the light [103].

SPR provides a sensitive, noninvasive, label-free, and real-time method of analyzing and monitoring biomolecular interactions. Molecular interactions between proteins, for example, can

be detected via the SPR technique as the refractive index of the film changes by binding the analyte molecule to an immobilized receptor molecule on a metal thin film [22].

The surface plasmon effect was first introduced by Wood in the early 20th century, while Kretschmann and Otto described the optical excitation of surface plasmons via the attenuated total reflection (ATR) technique later in 1968. Figure 2-10 illustrates the surface plasmon sensing technique demonstrated by Kretschmann with prism coupling to detect biomolecules [104]. The sensing setup generally consists of a thin metal film, mainly gold or silver with 50 nm of thickness, attached to a high refractive prism coupler, which is immobilized with the recognition molecules. When the light incidents the prism wall, it is mostly reflected, while a small portion is leaked into the thin metal film in the form of an evanescent wave and passes through the thin metal film. This evanescent field excites surface plasmons on the other side of the gold at the interface between the metal surface and the detecting analyte. Attachment of the analyte to the receptor causes a change in the refractive index, which is detectable in a real-time and label-free manner. Additionally, a shift in the SPR resonance angle as a reflectivity curve can be observed.

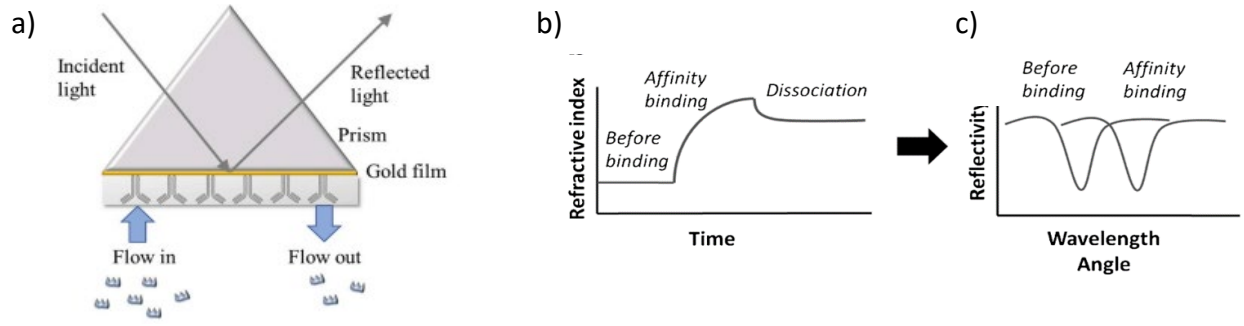

Figure 2-10: (a) Kretschmann type prism coupling SPR biosensor framework (b) change of refractive index vs. time due to the affinity binding between receptors and analytes causing (c) a shift of the reflectivity curve vs. wavelength of source light or angle of reflected light [22]

SPR has been applied in diverse analytical applications, including food safety [105] and food allergen detection [102, 103], such as Escherichia coli [108], doping analysis [109], environmental monitoring, and more promising in medical diagnosis and clinical applications.

2.3.6 LSPR based biosensors

When the dimensions of the nanoparticles are lower than that of the incident wavelength of light (figure 2-11), the resulting electronic oscillations due to their interaction with the photon electric

field is localized. Localized surface plasmon resonance (LSPR) can be demonstrated via the emergence of a remarkable absorption band. The frequency and intensity of the adsorption band are dependent on the nanoparticle material, size, and shape [91, 106].

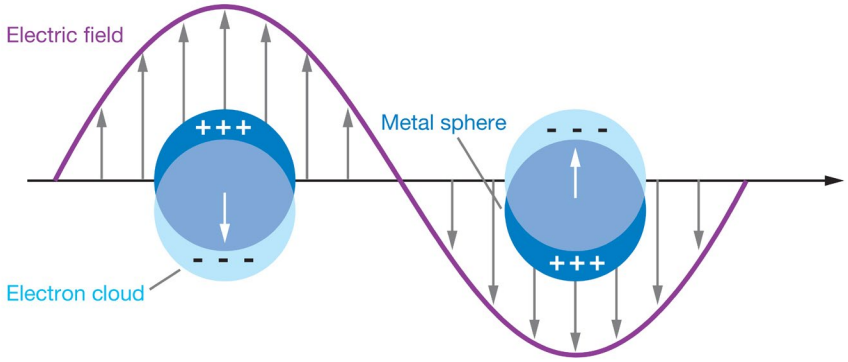

Figure 2-11: Schematic of localized surface plasmon resonance [110]

Gold nanoparticles have been widely utilized for LSPR biosensors with applications in chemical detection, biochips, and biomolecules recognition. The wavelength of the LSPR peak for various shapes of AuNPs, including spheres, nanorods, star shapes, or polyhedral, varies in location [111]. Figure 2-12 illustrates the different plasmonic peaks that result from different shapes of the AuNPs. The peak around 500 is indicative of a sphere-shaped AuNPs.

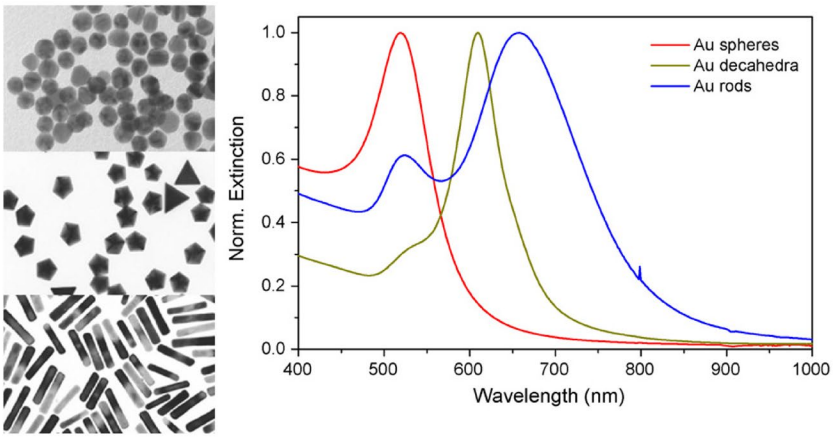

Figure 2-12: TEM and UV-Vis spectra of AuNPs with various geometric shapes [111]

LSPR biosensing is performed in two modes; resonance alteration due to the aggregation of the metal nanoparticles or change of refractive index. In the first mode, the change of color and redshift of the resonance peak due to the aggregation of the nanoparticles represents the sensing

performance. In other words, when two metal nanoparticles, after the interaction with the analyte, come close to each other within less than one diameter, the corresponding resonance peak redshifts, which can indicate the presence of the analyte. In the latter mode, however, the change in the refractive index causes the redshift in the LSPR spectrum. Biomolecular interaction at the surface of the functionalized gold nanoparticles, for example, causes a difference in the local refractive index, which can be detected by observing a displacement of the LSPR peak (figure 2-13).

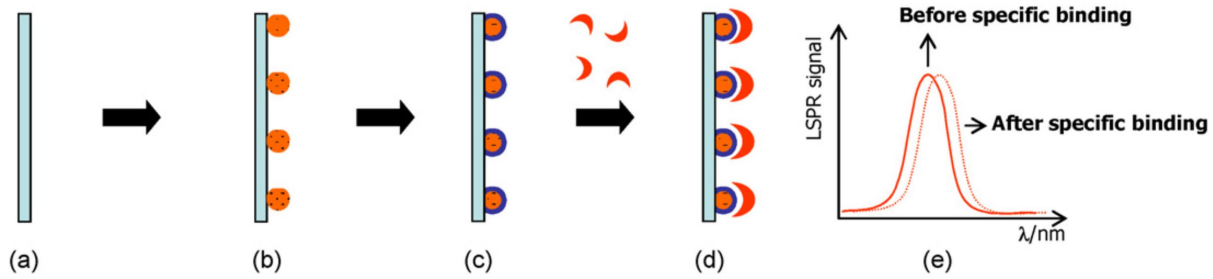

Figure 2-13: Schematic diagram of the refractive index based LSPR biosensor preparation. Functionalized gold nanoparticles were deposited on a glass slide (b). Adding the biomolecule analytes (c) followed by the interaction between the biomolecules and the gold nanoparticles (d). This interaction results in a shift in the LSPR signal, as shown in (e).

2.3.7 LSPR based biosensor applications

LSPR-based biosensors have been developed to recognize the leading causing root of the various diseases and health conditions. These optical-based biosensors are used to reveal the elevated levels of biomarkers and biomolecules in body fluids and detect pathogenic microorganisms such as bacteria and viruses. Antibodies are frequently used as receptors for selective binding and consequently identifying the target analyte. Numerous novel methods have been recently developed to replace the antibodies with other sensing molecules such as aptamers and imprinted polymers; however, antibody- immobilized platforms are still the primary option for fabricating LSPR based biosensors since they have shown high stability, affinity, and selectivity [23].

2.3.7.1 *Biomolecules detection*

Glucose, the end-product of the digestion of carbohydrates, has a key role in generating the required energy for cells and the body's metabolism. Generally, the concentration of glucose in the blood is maintained by insulin, a regulatory hormone produced by the islets of Langerhans within the pancreas. When the body fails to make enough insulin to control the amount of glucose in the blood at a constant range, it results in diabetes mellitus. Type 1 diabetes is an autoimmune

disease when the pancreatic cells are damaged and fail to produce insulin. In contrast, insulin resistance in (signaling) cells is the main reason for type 2 diabetes, which prevents the cells from up taking the glucose in the blood [112]. To date, loads of different bio-sensing essays have been designed for glucose detection in solutions, with some focusing on the diagnosis of elevated levels of glucose in the human body fluids such as saliva and blood [112].

An LSPR based glass sensor chip layered with self-assembled AuNPs was created by Chou et al. to detect glucose in saliva. It was fabricated in a comfortable and low-cost way. With only a redshift in the UV spectrum peak after soaking into a sugar-containing solution, the sensor identifies the presence of the glucose in those solutions. Consequently, it enables a straightforward and inexpensive real-time detection of various concentrations of glucose with high sensitivity. Moreover, it was also shown that smaller AuNPs (less than 20 nm) lead to a better sensitivity compared to bigger ones [113].

2.3.7.2 *Bacteria detection*

Microbial infections are among the deadliest diseases threatening human health and causing multiple health problems. Bacterial contamination is a serious concern in various areas, from the food industry to public health and hospitalization [114]. Food-borne illnesses are mostly caused by bacterial contamination arising from substandard storage, transportation, and distribution conditions of food products. Deficiency in methods and techniques to detect bacterial pathogens in these processes leads to serious health conditions [115].

Salmonella typhimurium, *Escherichia coli O157: H7*, *Staphylococcus aureus*, *and Listeria monocytogenes* are the most prevalent disease-causing pathogenic bacteria. Severe health conditions and diseases such as septicemia, diarrhea, fatigue, hemolytic uremic syndrome, abdominal pain, and even kidney failure can be triggered by consuming bacterial-contaminated water and food products [116]. Severe dehydration due to diarrhea, as the body loses a considerable amount of water, can lead to death. This incidence is especially more serious in young children. Therefore, reliable methods to accurately identify microbial pathogens to prevent such infectious diseases are highly demanded. Typical practices for detection include plate culturing and colony counting, polymerase chain reaction (PCR), and enzyme-linked immunosorbent assay (ELISA). Generally, PCR-based methods are time-consuming and require well-trained staff, while ELISA tests entail specific antibodies [117].

Several chemical sensors and biosensors have been developed to diagnose pathogenic bacteria. These include electrochemical sensors, surface plasmon resonance sensors, chemiluminescence, fiber-optic biosensors, impedimetric Immunosensors, microfluidic devices, and conductometric methods15-17 [118]. However, despite their advantages, they demand well-trained technicians, advanced equipment and require large concentrations of pathogens for proper operation and detection. Moreover, they are relatively costly, time-consuming, and complicated procedures that often fail to result in reliable results. These shortcomings restrict the application of such detection sensors in real-time point of care diagnostics. Hence, more convenient, cost-effective and quick sensing procedures are required for a reliable analyte/pathogen identification [45]. In this venue, developing LSPR based biosensors using AuNPs is one of the promising strategies to fill in the present detection gap.

Yoo et al. have fabricated an LSPR sensor using repeated layering of AuNPs and silica conjugated with Aptamers. In general, aptamers are nucleic acid structures showing high affinity and specificity to a broad range of analytes that can be easily synthesized and modified inexpensively and take a crucial part in sensing the bacterial cells. The Aptamer immobilized sensor created by Yoo et al. resulted in a detection limit of 30 CFU with excellent sensitivity to 3 different types of bacteria. However, the preparation process comprised multiple steps and complicated equipment such as E-beam evaporator [115, 116]. Oh. et al. developed a portable LSPR based detection of *S. typhimurium* using aptamers conjugated AuNP-based sensor chip. By modifying the fabrication process and creating just a single layer of AuNPs, the sensor reported a straightforward and faster label-free identification of the targeted bacteria [45]. The detection could result within 30 to 35 min and less time was spent on preparing the glass slide-based biosensor in comparison with the previous sensor chip.

2.3.7.3 *Viral detection*

Surface plasmon resonance-based immunosensors have also been designed for the identification of viral pathogens like the one was used for rapid detection of the H7N9 influenza virus. In this case, it showed a higher detection limit than conventional methods used for influenza detection, including polymerase chain reaction and influenza diagnostic tests [117]. Gold nanoparticle-based sensor using the LSPR mechanism is a potentially reliable analytical method for the Newcastle disease virus (NDV) with a 50 -10 times increased detection limit [122]. Analogously, a label-free

LSPR based platform for detecting HIV was developed employing AuNPs and observing the changes of the refractive index on the AuNPs surface [123].

2.4 Silver nanoparticles

Due to their special chemical and optical properties, particularly antimicrobial effect, silver nanoparticles (AgNPs) have been widely studied and applied in some health care products. AgNPs have great potential in various biomedical applications such as medical device coatings, diagnostic and optoelectronic devices, imaging, and drug delivery systems. Physical, optical, and catalytic properties of AgNPs have been shown to get affected by alteration of their size, morphology, and surface characteristics. Therefore, synthesis routes of the AgNPs are of importance as they can impact the NPs properties. Similar to AuNPs, AgNPs are commonly synthesized through top-down physical methods, various wet chemical and photochemical bottom-up roots, and biological synthesis methods [124].

The physical approaches to synthesize AgNPs include laser ablation techniques and the evaporation-condensation methods. Although such methods contribute to the large-scale production of AgNPs with high purity, they suffer from several shortcomings, including high energy consumption, time-consuming production, and limited fabrication of NPs on a substrate and not in free form (e.g., powder). Here again, the wet chemical approaches are the industry standards for the manufacturing of AgNPs. Similar to AuNPs, AgNPs are chemically synthesized majorly through the Turkevich and Burst-Schiffrin methods using different reducing and stabilizing agents to control the size and shape of the AgNPs. Green synthesis and biological methods have also been used to synthesize AgNPs; however, their adoption remains restricted to relatively small-scale synthesis [124].

Since antimicrobial activity of the AgNPs is the primary attraction of these NPs, as far as this thesis is concerned, the discussion below will be limited to highlighting few advances related to such aspects only.

2.4.1 AgNPs as an antibacterial agent

Bacteria resistance against antibiotics is a serious concern of health systems. Using AgNPs as a disinfectant could be an efficient alternative that promises the development of various multi-functional biomaterials and devices. Antimicrobial wound dressings containing AgNPs, invasive

catheters, and endotracheal tubes coated with AgNPs are some commercially available applications using AgNPs as an antibacterial and antiviral agent and. Silver ions released from the AgNPs in the wound dressings kill the bacteria, therefore, prevent the infection at the exuding wound site [121, 122]. Dental implants and dental filling materials containing silver also are used to avoid infections and inflammations in the oral cavity [127].

Furthermore, AgNPs have been used for developing anti-infective fabrics and textiles, which can be used in protective clothing for healthcare workers, such as masks and security coats and hospital uniforms. AgNPs bonded to chitin nanofiber fabricated sheets have shown promising antimicrobial activities against bacteria like E. coli and viruses, including the H1N1influenza A virus. Such AgNPs embedded nanofiber structures can be utilized to produce antibacterial plastics, papers, and cloths [128].

2.4.2 Antiviral activity of AgNPs

Just like bacteria, viruses are also some of the primary microbes causing diseases threatening human life around the world. Due to their indifference to antibacterial medicine, viral infections can wreak havoc not only on the health of humans but also cripple the economy [129]. Although vaccination has led to control of the numerous viral infections or, in some cases, even extinction of the viruses, newly emerged viruses such as Ebola, Zika, and the most recent SARS-CoV-2 still cause hundreds of thousands of deaths [130]. The rapid outbreak of the novel viral diseases, in addition to the development of antiviral resistivity to conventional pharmaceutical products, are serious threats that caused bio-scientists and healthcare providers to rush in search of effective vaccines to stop the spread of such detrimental viruses (e.g., newly developed vaccines by China, Russia, USA, and Germany) [131]. Despite these efforts, recent reports in the UK of a new version of the SARS-COV-2 virus that does not respond to such vaccines is a cause of concern that is causing much anxiety worldwide.

Metallic AgNPs are highly promising in the fight against both versions of the virus, causing COVID-19 (and soon to be COVID-20) illness. In general, a viral infection is a result of viral replication, which begins with the entry of the virus into the host cell and then translation and production of copies of its genome using the cells' nucleic acids. It is more likely that AgNPs disrupt the contact and, subsequently, the adsorption of the virus onto the host cells by acting on the surface of the viruses [132]. Three different mechanisms of action are suggested for AgNPs

against viruses. Zodrow et al. and Gusseme et al. argue that Ag^+ ions released from the dissolution of AgNPs, could inhibit the virus replication. Ag^+ has shown to be able to strongly interact with functional groups of the surface proteins of viruses like thiol or the active sites of many enzymes involved in virus replication, thus interrupting the functionality of the viruses [129, 130]. The second mechanism suggests a physical interaction of the AgNPs with the surface of the viruses that hinders them from anchoring onto the host cells and, subsequently, restrain their infectious effects. In the last mechanism, the local release of the reactive oxygen species (ROS) from the AgNP bound to the virus can damage the membrane of the virus [39].

Although the actual antiviral mechanism of the AgNPs is not fully understood, the results of numerous studies have clearly demonstrated the antiviral activity of the AgNPs. For example, AgNPs have been effective against Herpes simplex virus type 1 (HSV) by inhibiting the binding of the virus to the cells [135]. Moreover, adhesion of the AgNPs to the envelope of the human immunodeficiency virus (HIV) has been shown to prevent its infection ability. It was suggested AgNPs bind to the virus surface glycoproteins, which can hinder the attachment of the virus to the cells [132, 133].

Although at its research infancy, the size of the AgNPs has shown to impact their antiviral activity, significantly. AgNPs of ≤25 nm have shown to have inhibiting effects against arenavirus replication [138]. Gaikwad et al. demonstrated the antiviral effects of AgNPs with a size of 7-20 nm against herpes simplex virus (HSV) types 1/2 and human parainfluenza virus type-3 [139]. The small size of 10 nm AgNPs also showed effects against the Monkeypox virus (MPV). However, increasing the size to 25 nm, 50 nm, and 80 nm raised the mean number of MPV plaque-forming units (PFU)/well. In this regard, the impact of the size of AgNPs on their antiviral capability is not well understood until today, but it is the subject of further research [140].

2.5 Application of silver nanoparticles to combat COVID-19

2.5.1 SARS-CoV-2

The newly emerged pandemic of coronavirus disease 19, known as COVID-19, is caused by severe acute respiratory syndrome coronavirus 2 (SARS-CoV-2). Although much disputed lately, December 2019 was when the first cases of the infection were publicly identified. Since then, millions of people have been tackling its massive outbreak in more than 199 countries and

territories worldwide. It has caused the death of hundreds of thousands and restricted everyday life of hundreds of million people. Needless to say that it continues to impact the world economy in a negative way unseen since the Great Depression [137, 138].

The coronaviruses are ca. 65-125 nm in size made up of RNA and belong to the Coronaviridae family, which cause infection in the upper section of the respiratory system and the gastrointestinal tract of the host. However, what makes SARS-COV-2 special is that it can invade the lower respiratory system as well, causing life-threatening illnesses in some patients. The reason why the virus is named corona arises from the morphology of the outer surface of the virus that is covered by spike proteins (S protein), which resembles a crown (figure 2-14) [143]. SARS-CoV-2 consists of 3 other types of proteins, two of which include envelope protein and membrane protein that reside in the outer membrane between the spikes supporting the spectrum integrity of the virus. The fourth protein, nucleocapsid, exists inside the membrane surrounding thousands of nucleotides of RNA, which form the viral genome. Spike proteins help in the binding of the coronavirus to the host cell receptors and entering the cells [144]. This new virus belongs to the human coronavirus species, which were previously discovered and known as SARS-Cov, Middle East respiratory syndrome (MERS) CoV, Human Cove (H-CoV) HKU1, HCoV-NL63, HCoV-OC43, and HCoV-229E with relatively similar genetic structure [130].

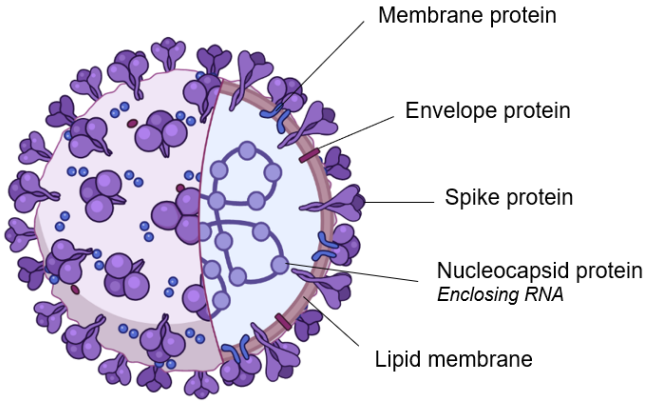

Figure 2-14: SARS-CoV-2 crown-like structure (The image is recreated in BioRender) [145]

High speeding spread, rising number of infected cases, and increasing mortality rates have led scientists to take stern actions to tackle the COVID-19 through developing promising diagnosis techniques and therapeutic approaches. Metallic nanoparticles, especially gold and silver

nanoparticles, owing to their remarkable records in diagnostics and disinfectants, have been considered as candidates in the fight to limit the spread of the virus. In this venue, this thesis presents, for the first time to my knowledge, an investigation of blade coated AgNPs (and AuNPs) and their impact on the mortality of COV-SARS-2.

2.5.2 Silver nanoparticles as a potential antiviral agent for disinfecting against COVID-19

Antiviral metal nanoparticles are capable of easily making interaction with the SARS-Cov-2. They typically are spherical with a diameter of 1-50 nm and an average of 22 nm, which is smaller than that of the virus [146]. AgNPs are suggested to be an efficient candidate to fight against the outbreak of the COVID-19. It is hypothesized that the AgNPs can bind to the spike glycoprotein of the virus; consequently, they hinder the adsorption of the virus onto the cells. Moreover, alkaline pH around the respiratory epithelium (where the virus is more likely to exist) caused by the release of the silver ions provides a hostile environment that can lead to the death of the virus. Figure 2-15 represents the virus function and the proposed mechanism of action of the AgNPs against the SARS-CoV-2 virus [147].

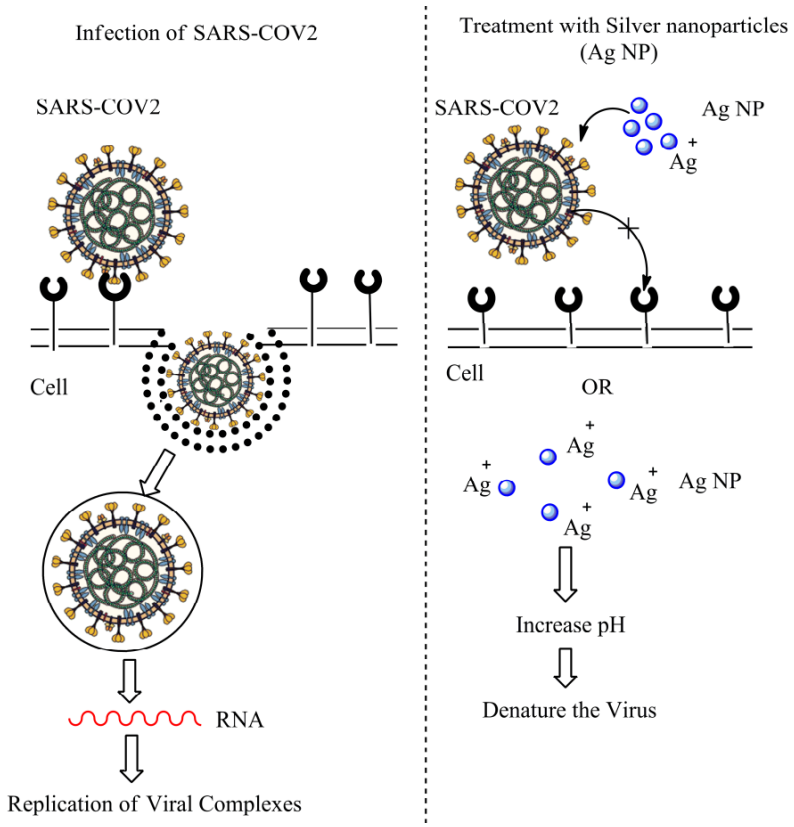

Figure 2-15: Schematic of the possible antiviral action of the AgNPs towards SARS-CoV-2 [148]

Chapter 3. Gold Nanoparticles

This chapter demonstrates the use of blade coating as a candidate for reactive fabrication of self-assembled gold nanoparticles (AuNPs) thin films on glass and silicon substrates. The benefits of this approach is to enable low cost and rapid manufacturing of NPs. In this study, the primary reactants including a gold precursor and a reducing agent are used in two consecutive coating runs, only, to fabricate the AuNPs. The shape and size distribution of AuNPs, as well as the film coverage, are shown to depend on the solvent system (acting as carrier for the reactants). The chapter describes the coating process and characterization of the fabricated NPs. Furthermore, the application of such blade coated films in a biosensing activity will be presented. In this regard, the blade coated AuNPs thin films is investigated for glucose detection by analyzing changes of the LSPR spectrum caused by changes of dielectric environment owing to the presence of the glucose with a different concentration in the surrounding medium.

3.1 Reactive blade coating of gold nanoparticles

3.1.1 Materials

Different organic solvents were used for preparing the inks for AuNPs synthesis. Isopropyl alcohol IPA ($CH_3CHOHCH_3$) was obtained from Pure Standard Products PSP. Toluene (TOL) (methylbenzene) (C_7H_8) was purchased from Fisher Chemicals (US), and 1,2-dichlorobenzene (DCB) ($C_6H_4Cl_2$) was obtained from Merck (Darmstadt, Germany). Other solvents, including dimethyl sulfoxide (DMSO) ($(CH_3)_2SO$) and tert-butyl alcohol (TBA) $(CH_3)_3COH$, were purchased from Sigma-Aldrich. The gold precursor gold (III) chloride hydrate ($HAuCl_4.xH_2O$) and oleylamine (OA) ($C_{18}H_{35}NH_2$) as the reducer were also purchased from Sigma-Aldrich. The solvents obtained from Sigma Aldrich and used in cleaning the substrates prior to the coating process include acetone (C_3H_6O) and ethanol (C_2H_5OH). Standard microscopic glass slides (25×75×1mm) purchased from Fisherfinest (USA) were cut into halves (25×30mm) and used as the working substrates. Silicon wafers were also used as alternate substrates. Blade coating was performed by carbon steel sterile surgical blades, which were obtained from Kai medical co. (Japan).

3.1.2 Characterization instruments

The absorbance spectrum of the substrates was measured by using Cary 7000 Measurement Spectrophotometer available at the Centre for Advanced Materials Research (CAMaR group labs facilities) at the University of Ottawa. To characterize the morphology of the nanoparticles and the microstructure of the coatings, the substrates' surface was observed by Scanning Electron Microscope (SEM) system Zeiss Gemini 500, available in the NanoFab lab facilities at the Research Centre for Photonics at the University of Ottawa. The crystalline phase characterization was carried out by X-ray diffraction analysis (XRD) using Rigaku Ultima IV Diffractometer at the X-ray Core Facility at the University of Ottawa. Surface tension and contact angle measurements were carried out using the Ossila Contact Angle Goniometer

3.1.3 Substrate preparation

Prior to blade coating, the glass/silicon substrates were ultrasonically cleaned by 4 consecutive steps starting with deionized water for 5 mins followed by immersing in acetone, ethanol, and isopropyl alcohol, each for 10 min. The substrates were dried with air flow after each cleaning step. The cleaned substrates were kept in a sealed container in a vacuumed desiccator before using for the coating process.

3.1.4 Ink preparation

Two different types of inks, including the reducer and gold precursor, were prepared for the blade coating process. For the reducing solution ink, 0.5ml of oleylamine (OA) was added to 5ml of toluene and shaken for 1 min at room temperature forming a colorless clear solution of 10% V/V ratio. Incidentally, the OA acts also as a caping agent for the resulting NPs, as will be shown later. The Au precursor solution ink was made by dissolving 20 mg (0.6mMol) of gold (III)chloride hydrate $HAuCl_4.xH_2O$ in 2ml of IPA (10 mg/mL) [0.03Mol/L] at room temperature, resulting in a yellow-colored solution.

3.1.5 Blade coating process

Figure 3-1 illustrates the fabrication steps of the NPs via the blade coating process. Clean microscope slides were used as substrate. A surgical razor blade was used to spread the liquids of each layer on top of the glass using two fixed Kapton tape railings of thickness 0.1mm. To coat a slide, first, a few drops of the reducing ink were placed on one sidewall of the blade onto the

substrate (figure 3-1.a). Immediately afterward, the blade was continuously dragged to the end part of the glass slide to spread the solution ink on the surface of the substrate (figure 3-1.b). To avoid cross-contamination, another clean blade was placed at the starting point (figure 3-1.c) to coat the gold precursor ink on the surface as the second layer following a similar procedure as for the first layer (figure 3-1.d). The angle between the blade and the substrate was maintained at 50 degrees during the coating process. After the coating process is complete, the substrates were heated first at 80°C for one hour and then at 100°C for 2h in order to accelerate the reduction reaction (figure 3-1.e). After the heat treatment, the deposited films were characterized to unveil the thin film structure and its surface morphology. All experiments were carried out in the air.

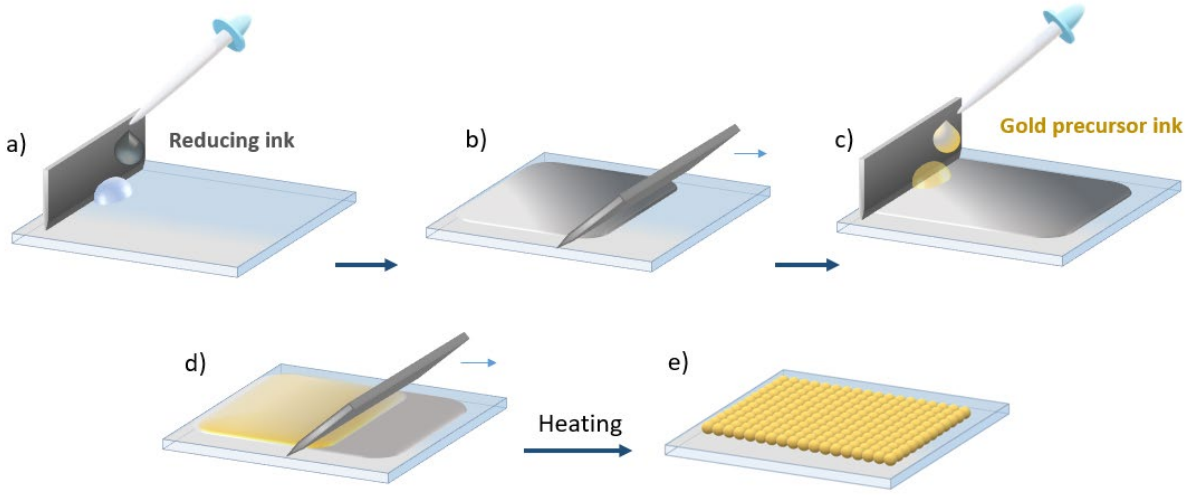

Figure 3-1: Blade coating process used for *in-situ* fabrication of the self-assembled AuNPs. a) Dispensing and b) Blade coating the reducing ink. c) Dispensing and d) Blade coating the precursor ink. e) Formation of AuNPs thin film after heat treatment, and f) SEM image of the synthesized AuNPs using TOL/IPA inks.

To study how different solvents affect the formation of the thin films and NPs, several organic solvents were utilized to prepare both the reducer and the precursor ink solutions. TOL and DCB were used as reducing ink, while IPA, DMSO, and TBA were used as the Au precursor solvent. Therefore, to distinguish each solvent system used in a different experiment, every experiment was named as the "reducer ink solvent /precursor ink solvent." For instance, a bilayer using TOL as reducer and IPA as precursor solvent is represented by "TOL/IPA," indicating the two different layers on top of each other with TOL ink blade coated first followed by that of IPA.

After the blade coating and post-processing steps, the resulting thin films were characterized by various techniques to analyze their morphology, and size, distribution, and crystalline phase structure of the synthesized NPs in the film. Morphology and the microstructure of the coatings, as well as the shape, size, and particle size distribution, were analyzed by imaging the surface of the blade coated silicon substrates using scanning electron microscopy (SEM-Zeiss Gemini 500). The silicon (Si) substrates were used to improve imaging due to Si's acceptable electrical conductivity, which reduced charging effects and thus facilitate the SEM imaging process. Images were taken in various magnifications while tuning the voltage to get reasonable resolution. Average particle size and size distribution were measured using ImageJ software, which is a standard image processing software for analyzing microscopic images [149, 150].

To identify the AuNPs coatings and analyze the plasmonic resonance properties of the blade coated thin film, UV-Vis spectrometer (Carry 7000) was used, and the corresponding plasmonic spectrum was obtained in the wavelength range of 400-800 nm. The crystallographic phase composition of the blade coated thin films was investigated by an X-ray diffractometer **(**Rigaku Ultima IV Diffractometer**).** Surface tension, as well as the contact angle of the various solvents and inks used in the coating processes, were measured using Ossila contact angle goniometer.

3.1.6 Results and discussion

In this section, the images and measurements obtained from the characterization of all the samples using different characterization techniques are provided along with a brief discussion of such results.

TOL/IPA

After heat treatment of coated TOL/IPA bilayer ink system, colored films were easily visible to the naked eye. The resulting XRD investigation of the coating is presented in figure 3-2. Distinct peaks at 38°, 44°, and 64.4° of the XRD pattern corresponding to the standard Bragg crystallographic planes of (111), (200), and (220), respectively, are clearly visible. These planes represent the face center cubic (FCC) lattice structure of the AuNPs, thus confirming the formation of the crystalline gold structure on the substrate surface. Increased intensity of the peak at 38° also indicates the preferential growth of Au in the (111) orientation [151]. Peaks at 31.5° and 32.7°

could be assigned to the remaining AuCl, which are not reduced completely during the heat treatment process.

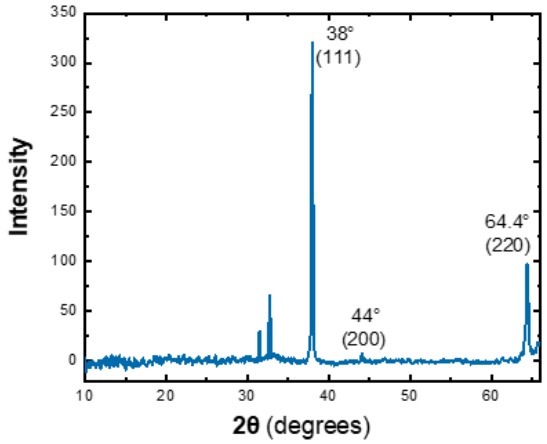

Figure 3-2: XRD analysis of AuNPs using TOL/IPA inks. Peaks at 38°, 44°, and 64.6° are related to crystalline gold.

Figure 3-2 shows the UV measurement of the TOL/IPA coated substrate. A distinct peak is seen at 552 nm, which corresponds to the characteristic plasmonic spectrum of the compact films of the AuNPs [54].

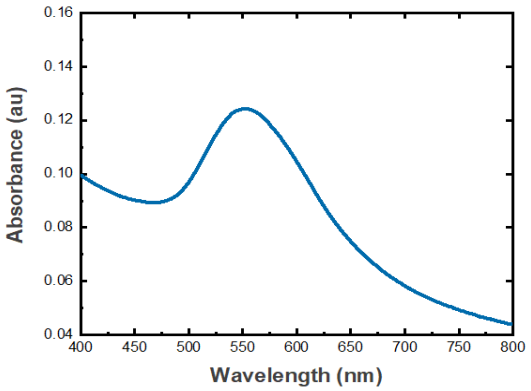

Figure 3-3: UV-Vis spectrum AuNPs using TOL/IPA ink shows plasmon resonance peak at 552 nm.

Further evidence of the formation of NPs is demonstrated in the SEM images (figure 3-4. a-c), which shows a uniform surface coverage of spherical AuNPs with well-defined nano-size. The particle size histogram of the nanoparticle in figure 3-4.d displays a uniform distribution of particle sizes with an average size of 10±2 nm.

The size distribution was obtained from measuring the surface area and then the diameter of the nanoparticles using ImageJ software. Image contrast was initially adjusted by applying a filter to set a suitable threshold that can determine the surface area of the particles. Then the surface area of the particles was measured through Analyze Particle command, and consequently, the diameter of the particles was calculated. Then the average particle diameter size and the distribution histogram of the particles were plotted using Origin software. The separation observed between AuNPs is due to the surface ligands around the AuNPs formed by oleylamine as a capping agent. Chemical composition analysis of the coating carried out by Energy-dispersive X-ray spectroscopy (EDS) (figure 3-5) also shows Au as the overwhelming component of the NPs. The carbon peak in EDS originates from the presence of the alkyl chain in the surface ligands formed around the NPs [152].

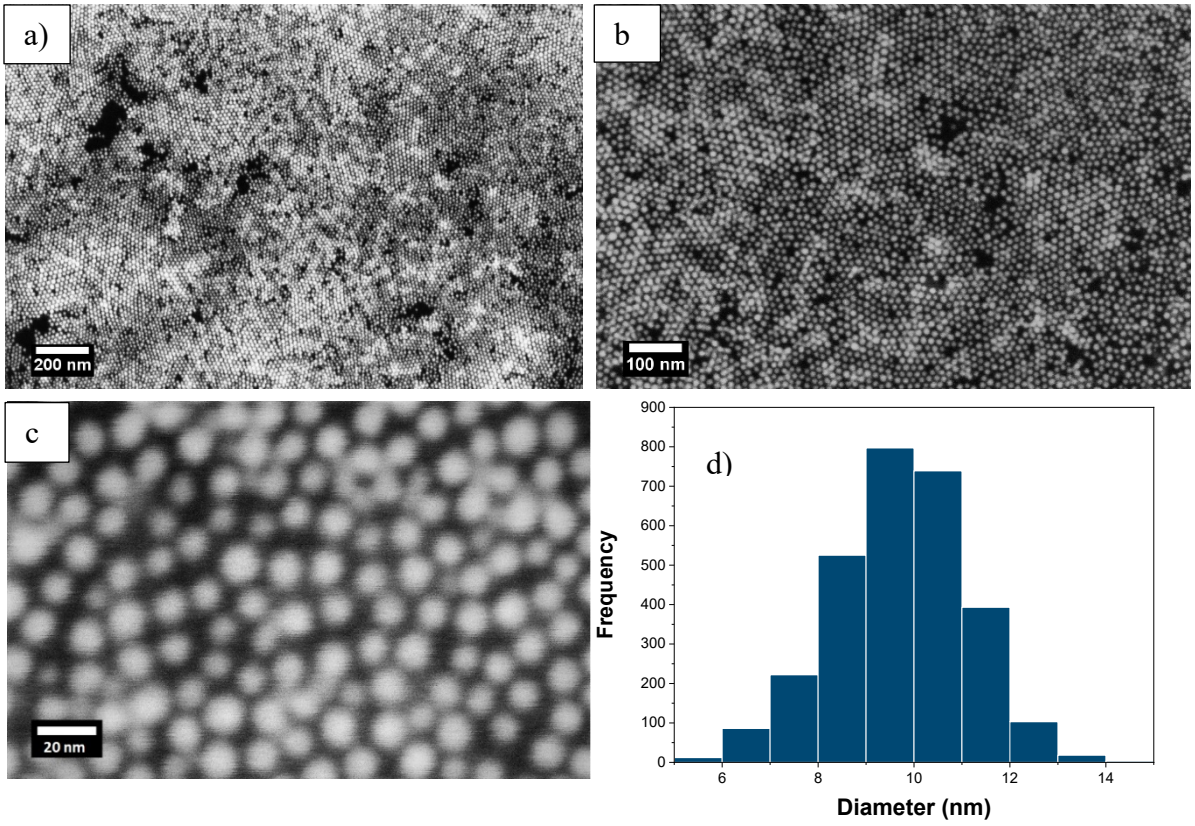

Figure 3-4: SEM images of synthesized AuNPs after blade coating of the TOL/IPA inks. Images at (a) 50 KX, (b)100 KX, (c)500 KX magnification showing close-packed spherical NPs. (d) particle size distribution histogram of the AuNPs obtained from image b with average particle size od (10±2) nm.

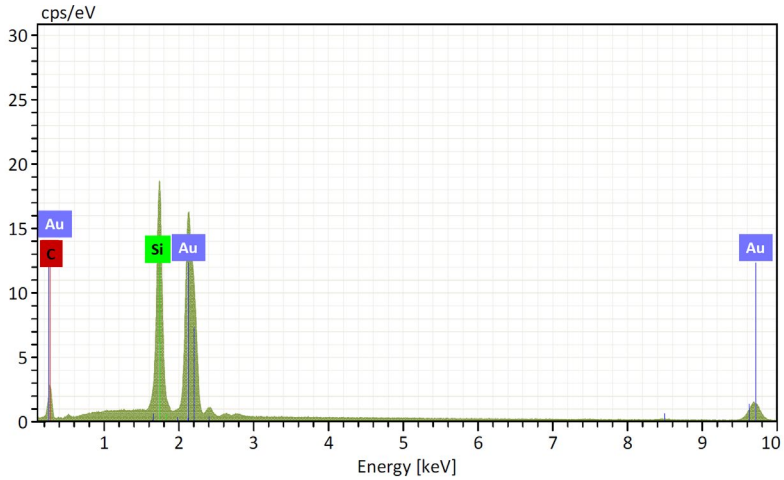

Figure 3-5: EDS analysis of TOL/IPA bilayer. Silicon peaks are due to the Si-wafer used as the substrate, and carbon peak is due to the alkyl chain of the oleylamine ligand as the capping molecules.

Figure 3-6 and figure 3-7 display the SEM images of the nanoparticles formed by repeating the experiment for second and third times, respectively. The average particle size was measured to be 10±2 nm. Self-assembled AuNPs have a spherical morphology and closed-pack microstructure.

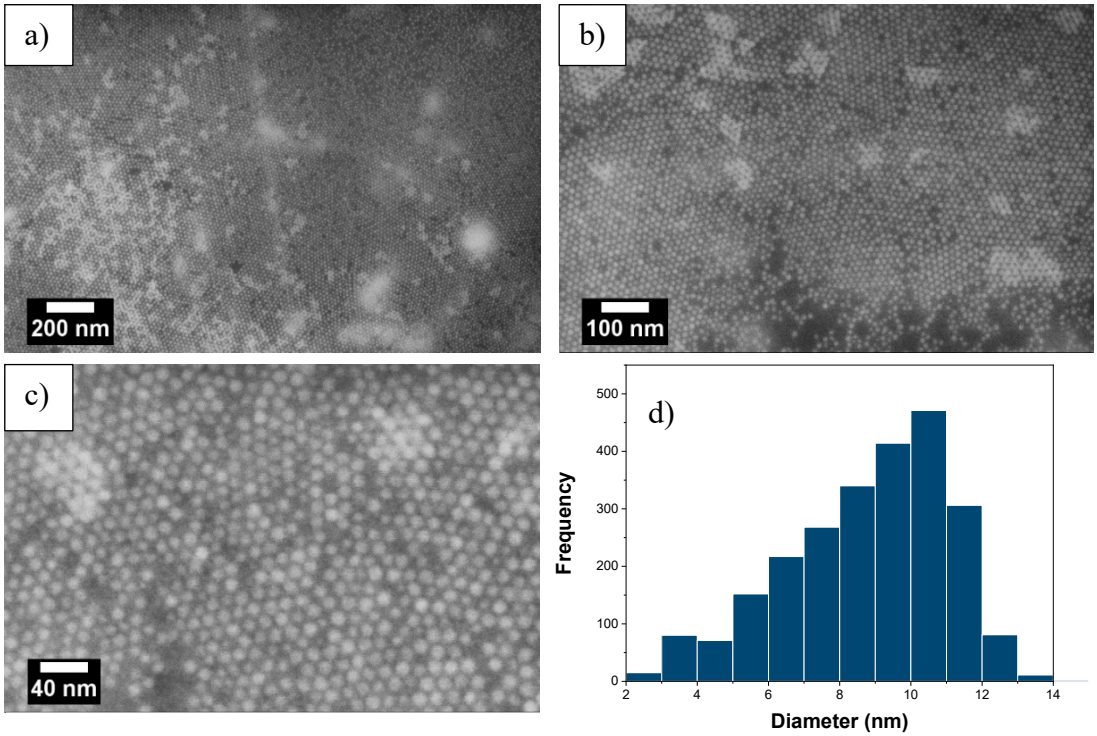

Figure 3-6: SEM images of the second experiment for the blade coated TOL/IPA bilayer. Images at (a) 50 KX, (b) 100 KX, (c) 250 KX magnification showing closed pack spherical NPs. (d) Particle size distribution histogram of the AuNPs obtained from image b with an average particle size of (10±2) nm. It shows results similar to the first experiment.

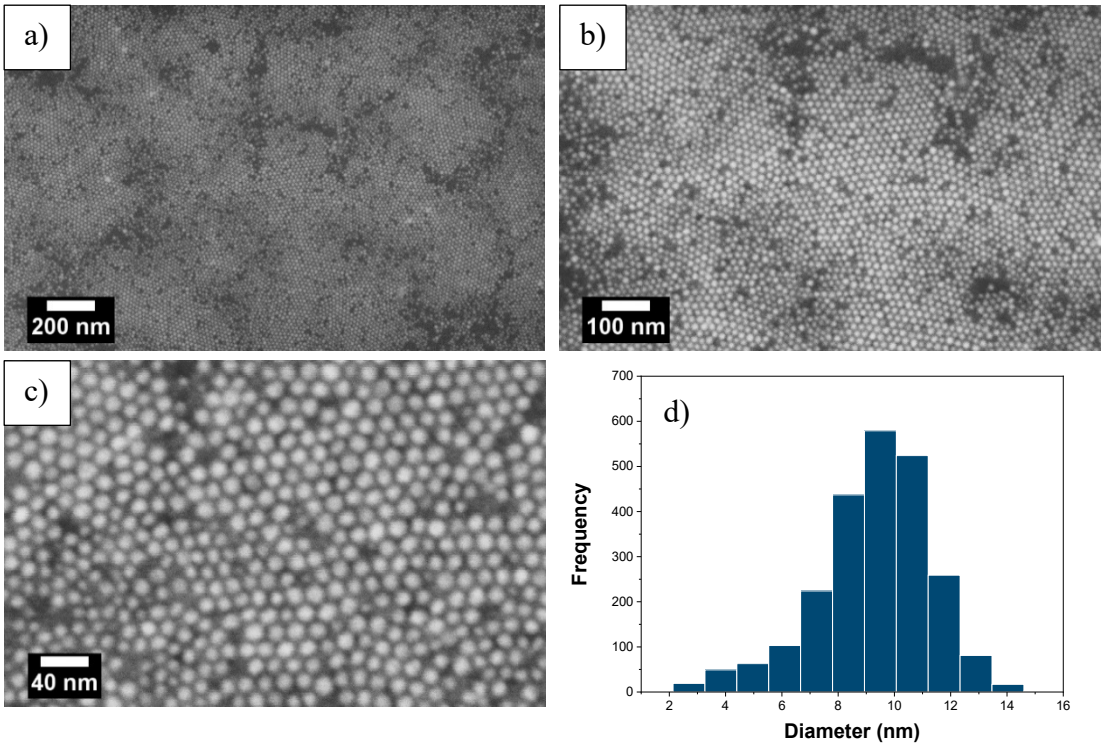

Figure 3-7: SEM images of the third experiment for the blade coated TOL/IPA bilayer. Images at (a) 50 KX, (b) 100 KX, (c) 250 KX magnification showing close-packed spherical NPs. (d) particle size distribution histogram of the AuNPs obtained from image b with an average particle size of (10±2) nm. It shows results similar to the first experiment.

A change in the concentration of the reducing agent or gold precursor was observed to influence the size of the NPs in agreement with previous results gained by reactive inkjet printing [4]. Table 3-1 represents the concentration of all the various inks and solvents used to prepare the gold coated bilayers.

I**mpact of Reducing Agent:** To study the effect of the reducing agent on the formation of NPs, the concentration of oleylamine was increased three times while the concentration of gold precursor was kept unchanged. In this case, 1.5 ml OA was dissolved in 5 ml toluene [30% V/V] (labeled as TOL3X), and 20 mg (0.06mM) $HAuCl_4.xH_2O$ was dissolved in 2ml IPA [0.03Mol/L] (labeled as IPA). The coating process and heat treatment were carried out analogously by first blade coating the reducer ink (TOL3X) on the glass substrate followed by the Au precursor solution (IPA). The resulting bilayer of TOL3X/IPA was then heat treated as described earlier for the TOL/IPA case. In this case, the SEM results (figure 3-8) show a slight increase in the size of AuNPs when oleylamine concentration was increased three times. A packed thin film of self-

assembled AuNPs with relatively high mono-dispersity and average particle size of (13±2) nm is visible in the image.

Figure 3-8: (a) SEM image of blade coated TOL3X/IPA bilayer showing the formation of self-assembled

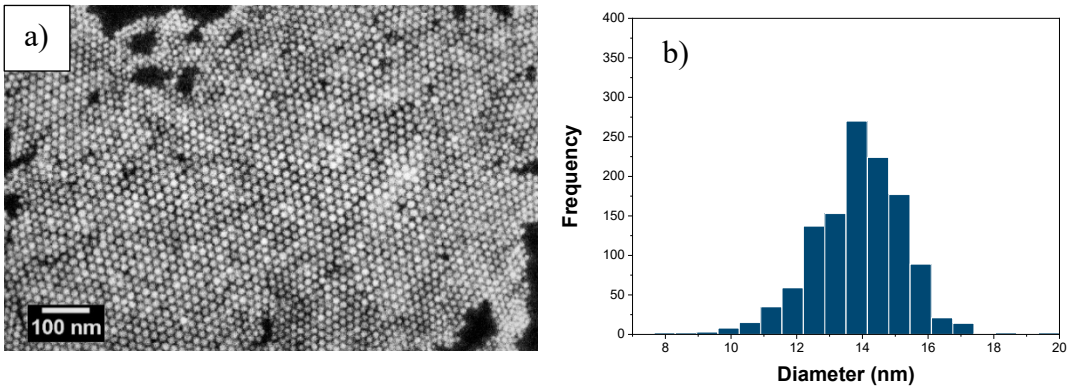

spherical AuNPs and (b) particle size distribution histogram of the NPs with an average particle size of (13±2) nm.

Impact of Gold Precursor: To investigate how a change in the concentration of gold precursor affects the on NPs size, the concentration of the AuNPs precursor was increased three times more than that of the initial experiment TOL/IPA. In this case, 60 mg (0.18mM) $HAuCl_4.xH_2O$ was dispersed in 2ml in IPA [0.09 Mol/L]. The reducer ink, however, was kept unchanged by using the 10% V/V ink solution of TOL and OA. The resulting blade-coated bilayer was labeled as TOL/IPA3X. In this case, the blade coating and heating were performed in a similar fashion to that of TOL/IPA. Characterization of the resulting thin film indicated that increasing the concentration of the AuNPs precursor resulted in an increased size of the self-assembled AuNPs. An average diameter of 11±2 nm as can be seen in the SEM image and size distribution histogram in figure 3-9-a and b, respectively.

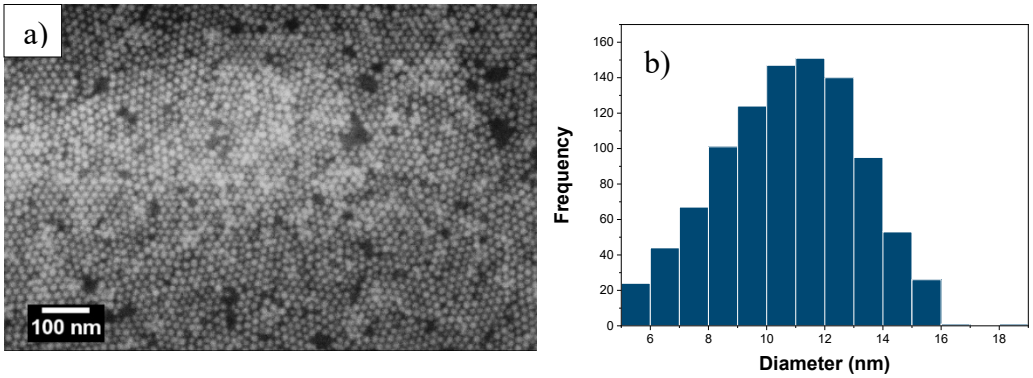

Figure 3-9: (a) SEM image of blade coated TOL/IPA3X bilayer showing the formation of self-assembled spherical AuNPs and (b) particle size distribution histogram of the NPs with average particle size of (11±2) nm.

Table 3-1: Description of the different batches of NPs synthesized by blade coating the bilayer of reducer ink/precursor ink subsequently. A bilayer consists of two layers of different inks on top of each other, e.g., TOL/IPA is a bilayer of TOL and IPA. Gold precursor is $HAuCl.xH_2O$. The notation "3X" indicates 3 times increase in the concentration of the reducer or precursor concentration. For example, IPA3X indicates 3 times increase in Au precursor concentration. 2x(TOL/IPA) represent a stack of two TOL/IPA bilayers printed in the following sequence: TOL/IPA/TOL/IPA.

Sample	Reducer ink		Precursor ink		Number of bilayers
	Solvent	OA/solvent (V/V%)	Solvent	gold precursor (mg/ml)	
TOL/IPA	TOL	10	IPA	10	1
TOL3X/IPA	TOL	30	IPA	10	1
TOL/IPA3X	TOL	10	IPA	30	1
2x(TOL/IPA)	TOL	10	IPA	10	2
3x(TOL/IPA)	TOL	10	IPA	10	3
TOL /DMSO	TOL	10	DMSO	10	1
DCB/IPA	DCB	10	IPA	10	1
DCB/DMSO	DCB	10	DMSO	10	1
DCB/TBA	DCB	10	TBA	10	1

Oleylamine (OA), Toluene (TOL) ,1,2-Dichlorobenzene (DCB), Isopropyl alcohol (IPA) Dimethyl sulfoxide (DMSO), Tert-Butyl alcohol (TBA)

Impact of Multilayers: The effects of the multilayers coating of the reducer and precursor inks in an alternate fashion on the formation of AuNPs was examined. In this case, the heat treatment step was carried after casting of each bilayer. Figure 3-10.a shows an SEM image of 2 TOL/IPA bilayers (2x(TOL/IPA)) blade coated on top of each other. The image clearly reveals the formation of AuNPs with an average particle size of (13±2) nm (figure 3-10.b), which, as expected, is larger than the case of a single bilayer of TOL/IPA. The average size of the AuNPs is expected to grow even larger as the number of the TOL/IPA bilayers is increased. Indeed, more than two times

increase in the average size ((22 ± 8) nm) of the self-assembled AuNPs can be seen for the case of 3 TOL/IPA bilayers (3x(TOL/IPA)) deposited on top of each other. The SEM image and the particle size distribution are shown in figures 3.10.c and 3.10.d, respectively. The particle size increase as the number of the bilayers increases is assigned to two causes. First, since the blade coating process of the bilayer is repeated 2 and 3 times, some of the smaller as-synthesized NPs formed during the processing of the first bilayer are re-dissolved and consumed by the large NPs, during the two consecutive bilayer processing steps, making them even larger. This growth is similar to the Ostwald ripening phenomenon, which occurs when large particles with low solubility grow larger at the expense of the more soluble smaller ones [153]. Secondly, the already synthesized NPs can also act as nuclei for further growth of NPs through a slow reduction of the excess Au^{3+} ions by oleylamine directly on the surface of the existing NPs formed in previous processing steps. Such processes can explain not only the large NPs formation but also the large standard deviation of 8 nm in the case of 3 TOL/IPA bilayers.

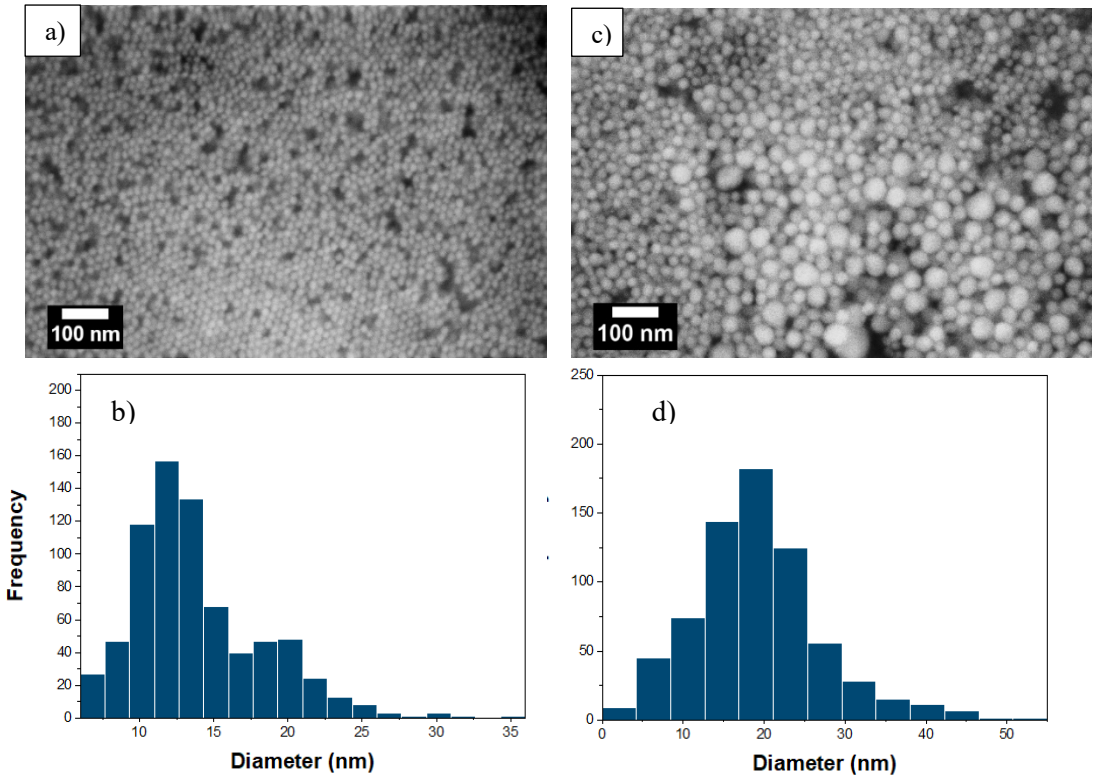

Figure 3-10: (a) SEM image of the film formed after two times repeating TOL/IPA bilayer coatings on top of each other, and (b) particle size distribution of the AuNPs obtained from the 2x(TOL/IPA). (c) SEM image and (d) particle size distribution of AuNPs obtained from 3x(TOL/IPA) bilayers blade coated on top of each other.

Impact of Solvents: In order to examine the effects of the solvents on the growth conditions of the AuNPs upon blade coating, various solvents were used instead of TOL and IPA repeating the coating process steps.

TOL/DMSO

First, the IPA was replaced by dimethyl sulfoxide DMSO as a solvent for the gold precursor ink. DMSO was selected due to its relatively high viscosity (1.99 cP at 25°C), similar to IPA (1.96 cP at 25°C), and a high boiling point (189°C). In this case, a solution of 10 mg/mL of Aucl.xH_2O in DMSO as the precursor ink was prepared. The coating process was carried out by blade coating the reducer ink solution (TOL) followed by the DMSO-based precursor solution on a glass substrate. However, immediately after blade coating on top TOL, the DMSO ink de-wetted the surface, forming island-shaped drops on the substrates rather than a uniform thin film on the surface. This is partly due to the higher surface tension of DMSO (44.1 $mN.m^{-1}$) compared to that of IPA (23 $mN.m^{-1}$). The XRD data (figure 3-11) confirms the poor formation and coverage of NPs as seen in the lack of significant peak intensity, which is not the case with TOL/IPA. The surface tension of IPA, however, is close to that of toluene (28.5 $mN.m^{-1}$), which assists in a better AuNPs film formation process.

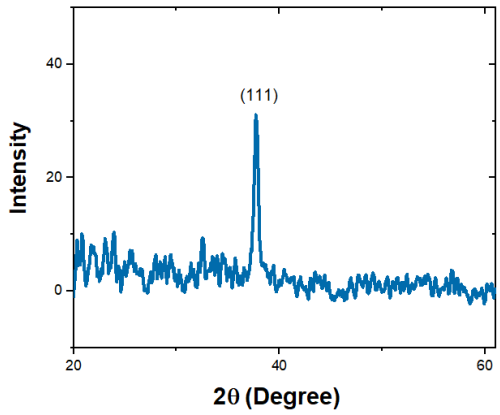

Figure 3-11: Figure 3-11: XRD pattern of TOL/DMSO bilayer shows a mall peak at 38°. The absence of significant peaks with considerable intensity assigns to the poor formation of NPs.

DCB/IPA

The next experiment was performed by substituting TOL with 1,2 Dichlorobenzene (DCB- surface tension of 36.84 $mN.m^{-1}$) for preparing the reducer ink (10% V/V OA in DCB). The gold precursor

ink was prepared using IPA as before (0.1 mg/mL $HAuCl_4.xH_2O$ in IPA). The coating process was performed analogously as in previous samples. This solvent system (DCB/IPA) resulted in a better film formation than the one created by TOL/DMSO, but not as uniform nor as close-packed as in the TOL/IPA case. Colored monolayer could be seen in some parts of the coating; however, it did not fully cover the substrate.

As indicated in figure 3-12, irregularly shaped particles with broad size distribution and an average size of (173±60) nm as clusters of smaller NPs can be seen in the SEM image. A broad absorption peak at 580 nm related to the plasmon resonance of these gold nanoparticles was also obtained by UV-vis absorption measurements (Figure 3-13.a). The red shift toward a longer wavelength, and the broadening of the peak, are due to the increased size of the particles. Figure 3-13.b indicates the peaks related to (111) and (200) crystallographic planes at 38° and 44° in the XRD pattern of the DCB/IPA bilayer.

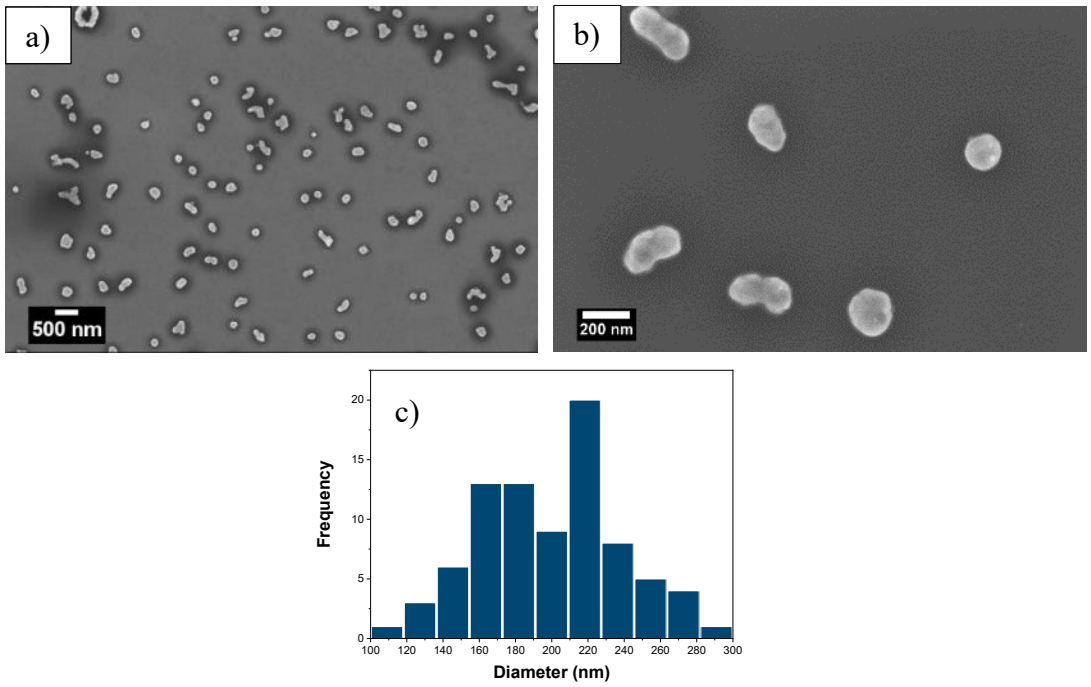

Figure 3-12: SEM images at a)10 KX and b) 50 KX of blade coated DCB/IPA bilayer show clusters of NPs in distributed in the distance over the surface (b) broad size distribution of particles with an average size of (173±60) nm.

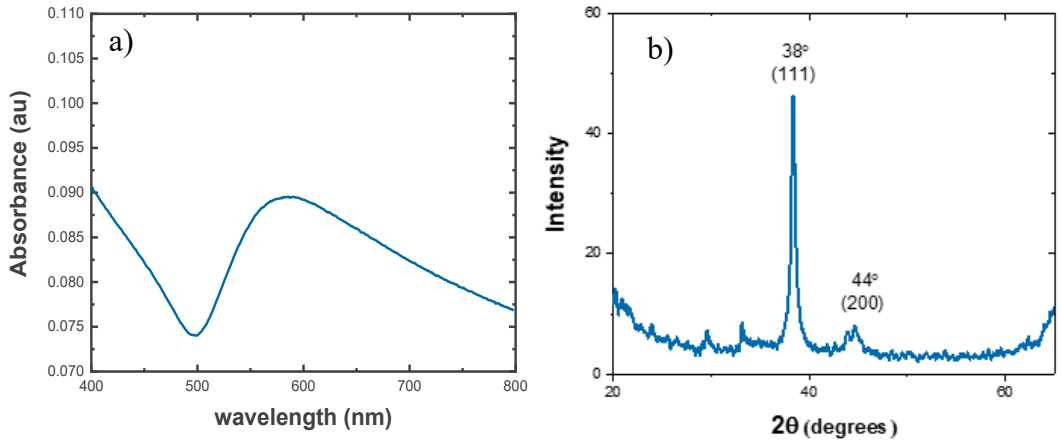

Figure 3-13: (a) UV-Vis Spectrum showing a red shift in the plasmon resonance peak and (b) XRD pattern of blade coated DCB/IPA bilayer indicating a preferential growth of the AuNPs in (111) orientation.

DCB/DMSO

In what follows, DCB was used for dissolving OA, and DMSO was used as the gold precursor solvent. Both solvents have nearly similar boiling points (DMSO-189 °C and DCB-180 °C). The reactive blade coating process was repeated using the same experimental conditions as in TOL/IPA. Upon inspecting the coated films, the coverage over the substrate surface was not uniform. SEM imaging results (figure 3-14) show dispersed NPs with a distorted spherical shape and an average size of (42±11) nm. UV-Vis measurements indicate a slightly red shifted (7 nm) plasmon resonance peak at 559nm (Fig. 4.c), in accord with previous results [154].

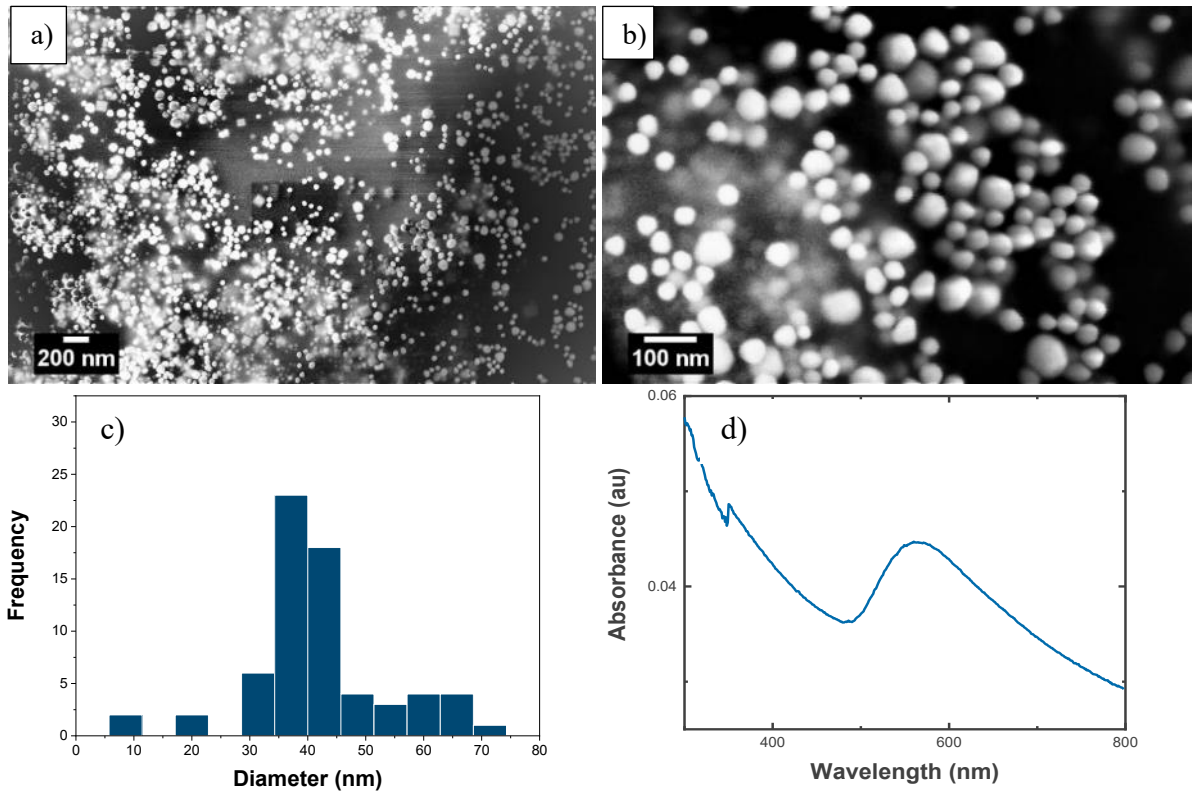

Figure 3-14: (a, b) SEM images at different magnifications displaying the formation of NPs after blade coating the DCB/DMSO bilayer. (c) Particle size distribution histogram obtained from image b. (d) UV-Vis spectrum of blade coated DCB/DMSO bilayer.

DCB/TBA

In these experiments, DCB was substituted for TOL, and tert-butyl alcohol (TBA) was used as a solvent for the gold precursor instead of IPA. Owing to its higher viscosity (3.38 cP at 30°C), TBA was observed to be a suitable candidate for creating a uniform coating as it spreads evenly over the substrate surface upon blade coating. The concentrations of DCB and TBA here followed the same values as in TOL/IPA case.

Upon blade coating of DCB and TBA inks, a colored thin film was observed on the substrate. Upon heat processing, the substrate surface was investigated via SEM imaging, which indicated the formation of NPs. The NPs formed had polyhedral shapes with an average particle size of (220±70) nm (figure 3-15.a, b, and c). The shape of the NPs is quite distinct and clearly different than the spherical form of the AuNPs obtained in the TOL/IPA case. Moreover, the size distribution is broader for the DCB/TBA bilayer than that of the TOL/IPA.

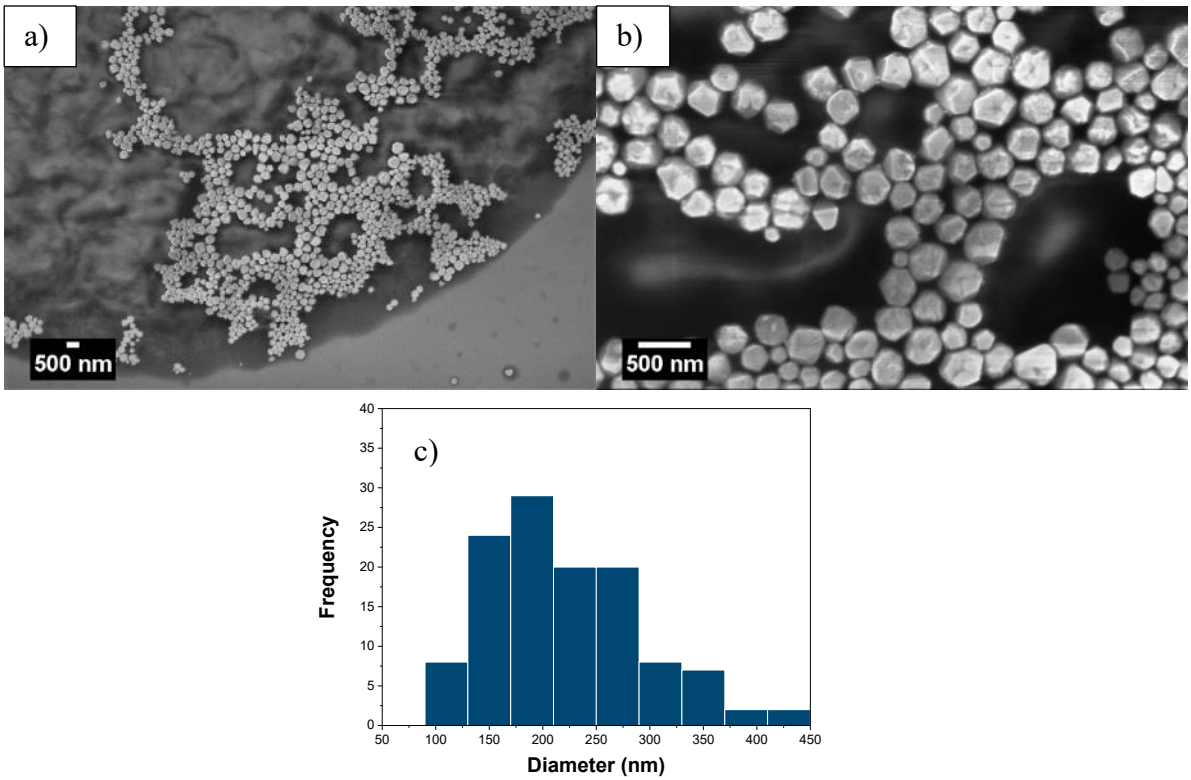

Figure 3-15: SEM image at a) 5 KX and b) 20 KX DCB/TPA bilayer showing polyhedral shape of NPs. (c) The broad size distribution of NPs with an average size of (220±70) nm made by the blade coated DCB/TBA bilayer.

Figure 3-16. shows a UV-Vis absorbance peak at 567 nm for the AuNPs thin film synthesized on the substrate. The XRD data (Figure 3-16.b) reveals a crystalline structure of the formed AuNPs with (111). The SEM results show that the AuNPs in the case of the DCB/TBA bilayer are much larger than those of the TOL/IPA case. The 15 nm red shift of the plasmon resonance peak confirms the increased size of the AuNPs obtained in the (DCB/TBA) case as compared to those synthesized from the TOL/IPA bilayer [154]. Using TBA in DCB/TBA resulted in a better film coverage compared to DCB/DMSO. This could be due to the lower surface tension of TBA (21.3±1) compared to DMSO (44.1±1).

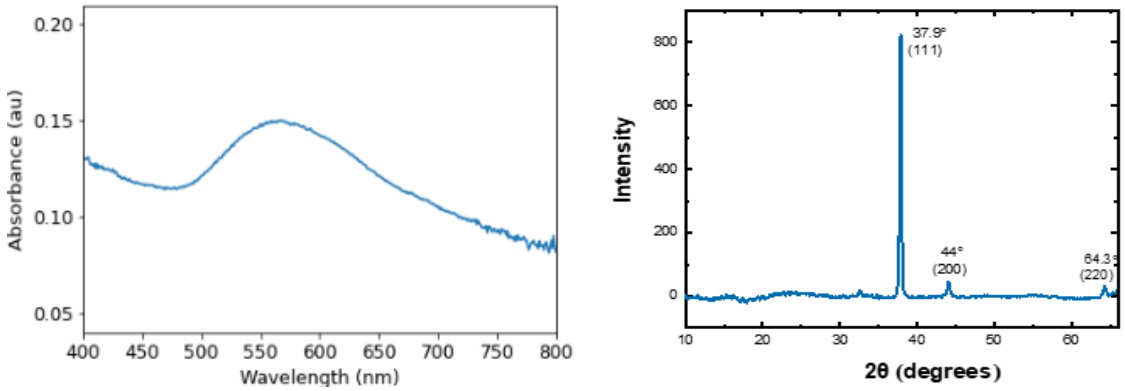

Figure 3-16: (a) UV-Vis spectrum showing a peak at 567 nm indicates a red shift due to the larger size AuNPs formed compared to TOL/IPA bilayer. (b) XRD pattern of the blade coated bilayer of DCB/TBA.

Impact of Solvent Polarity: The difference in polarity between TOL (0.099) and IPA (0.546) (table 3-2) makes them immiscible. This immiscibility allows the IPA-based solution to spread evenly on top of the coated TOL ink (TOL/IPA). Consequently, the reduction of the Au precursor by oleylamine takes place at the interface of these two solvents without their intermixing. This is a necessary condition for the formation of self-assembled nanoparticles [155, 156]. Additionally, the close surface tension values of both IPA and toluene lead to a low contact angle (<5°) when IPA-based ink is coated on top of the TOL reducer layer (figure 3-17). This leads to better spreading of the IPA film over the TOL layer during blade coating and, consequently, results in an overall better film coverage.

On the other hand, despite their immiscibility, the high surface tension of DMSO (44.1 $mN.m^{-1}$) compared to IPA (21.2 $mN.m^{-1}$) (table 3-2) prevents a uniform film formation over the substrate surface when coating TOL/DMSO bilayer. The surface tension of the mixture of DMSO and gold precursor was measured as 42.2 $mN.m^{-1}$ (table 3-3), and the contact angle over the coated layer of TOL reducer ink was measured to be 35 ±1°, as is illustrated in figure 3-17.a.

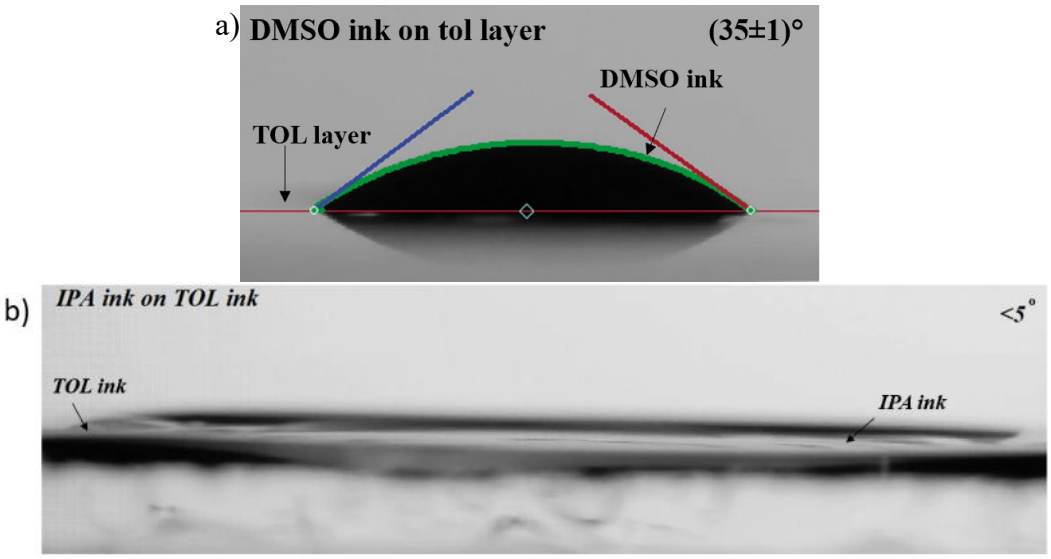

Figure 3-17: Contact angle of precursor ink on the reducer ink coated layer. **a** DMSO precursor ink dropped on the blade coated layer of TOL reducer ink shows a contact angle of (35±1) °, **b** IPA precursor ink dropped on the blade coated layer of TOL reducer ink has a contact angle of <5°.

On the other hand, in the DCB/DMSO bilayer, the solvents have a close polarity (0.225 and 0.444 for DCB and DMSO, respectively), which makes them miscible. In such a solvent system, closely packed structures could not form. Characterization of the DCB/TBA blade coated samples also revealed that using TBA as the precursor solvent can help in the synthesize of larger size AuNPs with relatively uniform coverage over the surface of the glass substrate. This could be due to quite high viscosity and the lower surface tension of TBA (21.3 $mN.m^{-1}$) compared to DMSO that allows some spreading over the substrate surface during blade coating. Higher viscosity of DMSO (1.99 cP) and TBA (3.35 cP) and DCB (1.32 cP) compared to IPA (1.96 cP) and TOL (0.59 cP) restricts the movement of the gold ions, hence, nucleation and growth is localized that results in formation bigger particles in the case of DCB/DMSO and even larger for DCB/TBA [][]. Taking the above observations into consideration, one concludes that the TOL/IPA solvent system was shown to be the best blade coated bilayer to yield monodisperse and spherical self-assembled AuNPs with the highest packing density and size uniformity among all other bilayers presented above.

It is worth mentioning that a uniform coverage was not achieved when the blade coating process was carried in the reverse order where IPA ink is deposited first, followed by the TOL ink. One of the reasons behind this observation is the relatively poorer wetting formed between IPA and TOL. The contact angle measured for the case of TOL being coated on an IPA layer on top of a glass substrate was 18.76±1°, as shown in figure 3-17, as opposed to < 5° for IPA on top of TOL film

(figure 3-18. b). This does not encourage the formation of uniform AuNPs after the heat processing step.

Figure 3-18: Contact angle of a TOL-based reducer ink drop on a blade coated IPA based precursor layer.

Table 3-2: Surface tension, contact angle, polarity, and boiling point of the solvents used for reducer and precursor inks.

Solvents for OA	Surface tension ($mN.m^{-1}$)	Contact angle on the glass	Contact angle on silicon	Polarity	Boiling point (°C)	Viscosity (cP) at 25C°
Tol	27.9	<5°	<5°	0.099	111	0.590
DCB	33.5±1	<5°	<5°	0.225	180	1.32
Solvent for Au						
IPA	21.2	<5°	<5°	0.546	82.5	1.96
DMSO	44.1±1	(15±1) °	(16±1) °	0.444	189	1.99
TBA	21.3±0.2	<5°	<5°	0.389	82	3.35
Oleylamine (OA), Toluene (TOL) ,1,2-Dichlorobenzene (DCB), Isopropyl alcohol (IPA) Dimethyl sulfoxide (DMSO), Tert-Butyl alcohol (TBA). Au precursor is $HAuCl_4.xH_2O$						

Table 3-3: Surface tension and contact angle of the reducer and precursor inks used for blade coating.

Reducing ink	Surface tension ($mN.m^{-1}$)	Contact angle on the glass	Contact angle on Si
TOL+OA	26.1	<5°	<5°
DCB+OA	29.5±1	(5±1) °	(5±1) °
Au precursor ink			
IPA+ $HAuCl_4.xH_2O$	20.3±1	<5°	10±1°
DMSO+ $HAuCl_4.xH_2O$	42.2±1	<5°	(5±1) °
TBA+ $HAuCl_4.xH_2O$	22.8±0.1	<5°	<5°
Oleylamine (OA), Toluene (TOL) ,1,2-Dichlorobenzene (DCB), Isopropyl alcohol (IPA) Dimethyl sulfoxide (DMSO), Tert-Butyl alcohol (TBA)			

3.1.7 Conclusion:

With the use of roll-to-roll compatible reactive blade-coating, it was shown to be possible to synthesize the monodispersed self-assembled Au NPs on rigid substrates with a size in a range of 10-12 nm by merely changing the concentration of the reactants. Various solvent systems, including TOL/IPA, TOL/DMSO, DCB/IPA, DCB/TBA, and DCB/DMSO, were used to investigate the effect of solvents on the size and shape of as-synthesized Au NPs, and quality of coated films on the substrates. Each solvent, owing to its specific properties, including polarity, viscosity, and surface tension, demonstrated a different effect on the coating uniformity and the NPs size and size distribution. Consequently, it is possible to control the shape and the size of NPs simply by using a different solvent system. TOL/IPA solvent system produced the most mono-dispersed self-assembled AuNPs, and uniform film as XRD and EDS analyses indicated that the as-synthesized NPs are pure FCC AuNPs. To sum up, a low-cost, fast, and facile, one-step synthesis of self-assembled gold nanoparticles having controlled size and shape via the reactive blade coating process was demonstrated, which is compatible with the roll-to-roll fabrication that can be scaled up to industrial-scale nanomanufacturing. This work can accelerate the development of low-cost, flexible, and R2R printable AuNPs-based thin-films applicable in various fields of applications.

3.2 Primitive LSPR-based glucose biosensing capability of the reactive blade coated AuNPs film

The LSPR effect of AuNPs is sensitive to small changes in the dielectric environment. In this regard, the presence of the analyte in the surrounding medium of the AuNPs produces a shift in the wavelength of the LSPR peak. Many self-assembled AuNPs thin films have been developed as biosensor platforms for detecting biomolecules such as glucose and various microorganisms, including bacteria and viruses [113, 117]. In this section, the LSPR sensing potential of the reactive blade coated AuNPs films is studied for glucose detection.

3.2.1 Materials and characterization

AuNPs thin films were fabricated on the glass substrates, as described previously in section 3.1, via reactive blade coating of the TOL/IPA inks. D-glucose ($C_6H_{12}O_6$) was purchased from Sigma-Aldrich. UV-Vis spectroscopy (Cary7000 Measurement spectrometer) was used to analyze the Surface plasmon behavior of the AuNPs films and assess their potential as a glucose sensor.

3.2.2 Detecting glucose in different concentrations

Several glucose solutions were prepared to have a concentration of 0, 5, 10, 20, and 50 mg/dL. This was achieved by dissolving 0, 2.5, 5, 10, 25 mg of d-glucose powder in 50ml of deionized water, followed by 10 min stirring. The substrates having the AuNPs film were soaked into the glucose solutions for an hour and then were dried with air blow. The absorbance peaks were measured before and after soaking into the solutions for each substrate using UV-Vis spectroscopy.

3.2.3 Results and discussion

Figure 3-20 shows the LSPR-based glucose sensing using the blade-coated AuNPs films. Red shifts in the wavelength of the peaks were observed after soaking the films into the various concentrations of glucose solution. The observed shifts in LSPR peak were ca. 3 nm, 5nm, 7 nm, and 10 nm for concentrations of 5mg/dL, 10 mg/dL, 20 mg/dL, and 50 mg/dL, respectively. As expected, the zero glucose concentration did not result in any shifts in the peak wavelength of the LSPR.

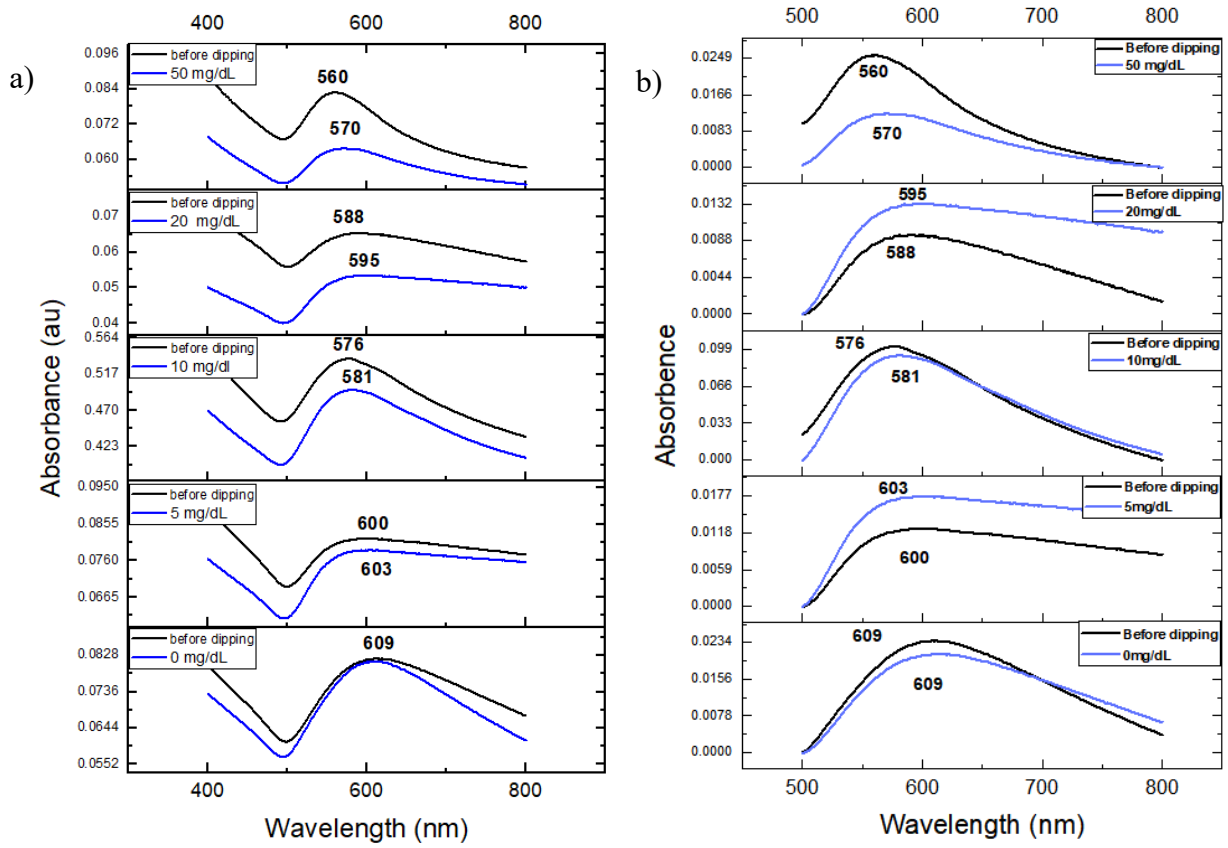

Figure 3-19: a) The UV-Vis spectra of reactive blade coated AuNPs films for detecting 5, 10, 20, 50 mg/dL of glucose solutions. b) Normalized peaks show red shifts after dipping the NPs films in the glucose solutions.

Clearly, the red shift of the LSPR peak to longer wavelengths is related to the detection of glucose by the AuNPs layer. The reason for this shift is due to the hydrogen bonding between the oleylamine on the surface of the AuNPs and the hydroxyl groups of the glucose, which results in the binding of glucose to the AuNPs surface, and consequently changing the dielectric environment around the NPs. This, in turn, leads to the red shift observed in the LSPR peak for the various glucose concentrations. In our case, a glucose detection limit of 5 mg/dL is recorded. The results reported here are comparable to those of published literature on LSPR-based biosensors using self-assembled AuNPs thin films, where the AuNPs were previously made into a colloidal suspension using the time (roughly > 8 hours) and resource-consuming traditional wet chemistry methods described before [113]. With a similar detection limit as traditional approaches, our reactive blade coated film fabricated within 3 hours, along with its roll-to-roll printing compatible nature, suggests a low-cost approach to glucose sensor fabrication.

3.2.4 Conclusion

It has been shown in this chapter that reactive blade coated AuNPs thin films are candidates for glucose detection. Different concentrations of glucose solution contributed to a red shift of varying magnitude in the LSPR peak of the blade coated AuNPs. It was observed that increasing the concentration of the glucose from 5 to 50 mg/dL resulted in a longer red shift in the wavelength of the LSPR peak.

Although the experiment was limited to AuNPs, our approach can easily be extended to other metallic or nonmetallic nanoparticles that are used in bio-detection. However, sensitivity and specificity of the detection needs to be optimized in order to develop a biosensor platform used for a reliable glucose detection. Moreover, further functionalizing of the AuNPs with proper functional groups can impart a specificity of the biosensing chips (substrate-NPs layer) to detect various analytes. For example, using AuNPs decorated with antibodies or aptamers can be used to detect certain biomolecules and microorganisms analogous to detecting *Salmonella typhimurium* by Oh et al. [117].

Chapter 4. Silver Nanoparticles

Based on the promising results for the fabrication of AuNPs thin films, the application of reactive blade coating was extended to the fabrication of silver nanoparticles (AgNPs) thin film due to their critical need in antimicrobial applications. This chapter describes the process of *in situ* self-assembly of AgNPs thin films via reactive blade coating and the influence of various solvents on the NPs and film forming properties.

AgNPs have been suggested as an effective alternative for disinfecting the SARS-CoV-2 virus (the cause of COVID-19 illness) [37, 157]. The reactive blade coated AgNPs thin films fabricated in this study were tested in the disinfection of viruses, namely the Human Coronavirus 229E, a surrogate to SARS-CoV-2 (same family of viruses). The results demonstrate unprecedented results with such a low-cost approach to AgNPs fabrication, with a 99.99% disinfection rate.

4.1 Reactive blade coating of silver nanoparticles

4.1.1 Materials

Different organic solvents, including TOL, 1,2-dichlorobenzene (DCB), isopropyl alcohol (IPA), dimethyl sulfoxide (DMSO), and tert-butyl alcohol (TBA), were used for preparing the various inks for the synthesis of AgNPs. Furthermore, two silver salts, including silver nitrate AgNO3 and silver perchlorate hydrate $AgClO_4.xH_2O$ (purchased from Sigma-Aldrich), were used as silver precursors. As in chapter 3, oleylamine (OA) was used as the reducing agent.

Standard microscopic glass slides cut into two halves(25×30×1mm) and cleaned following the procedure described in chapter 3 were used as substrates. Besides, silicon substrates were also used to assist in better SEM imaging of the self-assembled films.

4.1.2 Characterization Techniques

To analyze and characterize the AgNPs thin films, characterization techniques including UV-Vis spectroscopy, SEM, and X-ray diffraction analysis were used. These tools, along with their location were presented in chapter 3.

4.1.3 Ink preparation

Reducing ink was prepared by dissolving 0.6ml of oleylamine in 2ml toluene-TOL- (or 1,2 Dichlorobenzene (DCB)) acting as a solvent. This was followed by shaking the mixture for 1min at room temperature (RT), which resulted in a colorless clear solution. Silver precursor inks were also prepared using 2ml of various solvents, including isopropyl alcohol (IPA), Tert-butyl alcohol (TBA), Dimethyl Sulfoxide (DMSO), and 50 mg silver salts (25mg/ml) silver perchloride hydrate or silver nitrate) at RT.

4.1.4 Blade coating process

Figure 4-1 illustrates the steps of the coating process used for the self-assembly of the silver nanoparticles. It is similar to the process described in chapter 3. The reducer ink (figure 4-1.a) was coated on the cleaned glass slides, followed by coating the silver precursor ink on top of the first layer (figure 4-1.c). The angle between the blade and the substrate was maintained at 50 degrees during the coating process. After the coating steps are finished, the substrates were heated first at 80°C for one hour, followed by 120°C for 3 h. The resulting coating is illustrated in figure 4-1.e.

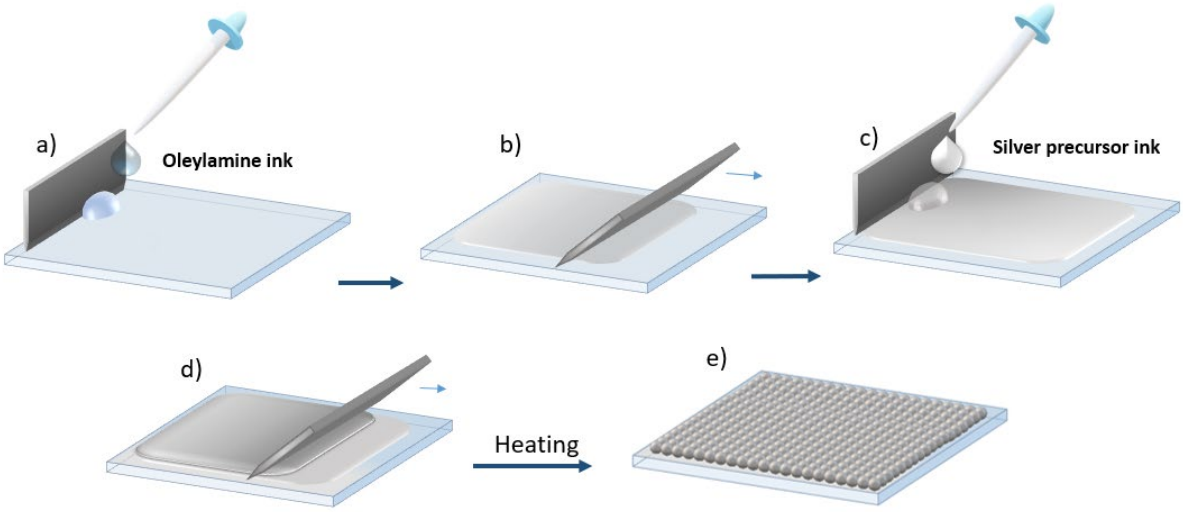

Figure 4-1: Blade coating process used for *in-situ* fabrication of the self-assembled AgNPs. a) Dispensing and b) Blade coating the reducing ink. c) Dispensing and d) Blade coating the precursor ink. e) Formation of AgNPs thin film after heat treatment.

4.1.5 Results and discussion

The characterization results of the various samples obtained using different solvent systems and precursors are presented in the following section.

TOL/IPA

A precursor of silver perchlorate hydrate was dissolved in IPA. Toluene (TOL) was used as a solvent for oleylamine to prepare the reducer ink. The TOL/IPA bilayer was blade coated. After the heating process, a silver-colored layer could be seen on the substrate. However, the color was not uniform, indicating a non-uniform coverage of the coated film on top of the substrate. Optical absorption spectra were recorded for this sample. Figure 4-2.a shows a clear UV absorbance peak at 444 nm, which is associated with the surface plasmon response peak of AgNPs. XRD pattern in (figure 4-2.b) indicates the presence of peaks at 2θ of 38.18° and 44.25°, which are attributed to the (111) and (200) crystallographic planes of the face-centered cubic structure of Ag metal, respectively. The peak at 33.03° could be related to the remaining AgCl ((200) plane) not fully reduced during heat treatment. The SEM images, along with analysis of particle size distribution, are presented in figure 4-3. The image reveals the presence of AgNPs with an average size of (16±3) nm.

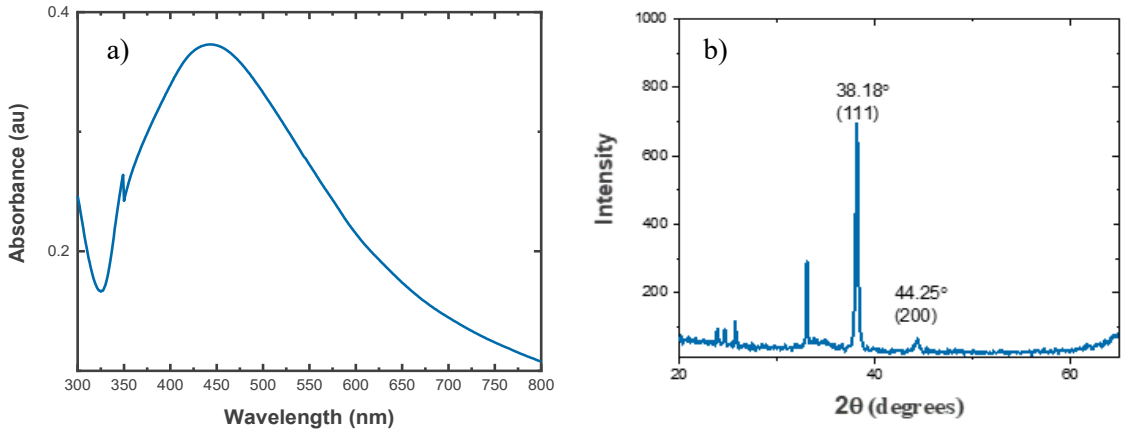

Figure 4-2: Characterization of TOL/IPA bilayer. (a) UV-Vis absorbance spectrum of AgNP films showing plasmon resonance peak at 444 nm, b) XRD spectrum of AgNPs showing distinct peaks at 38.18° and 44.25° characteristics to silver.

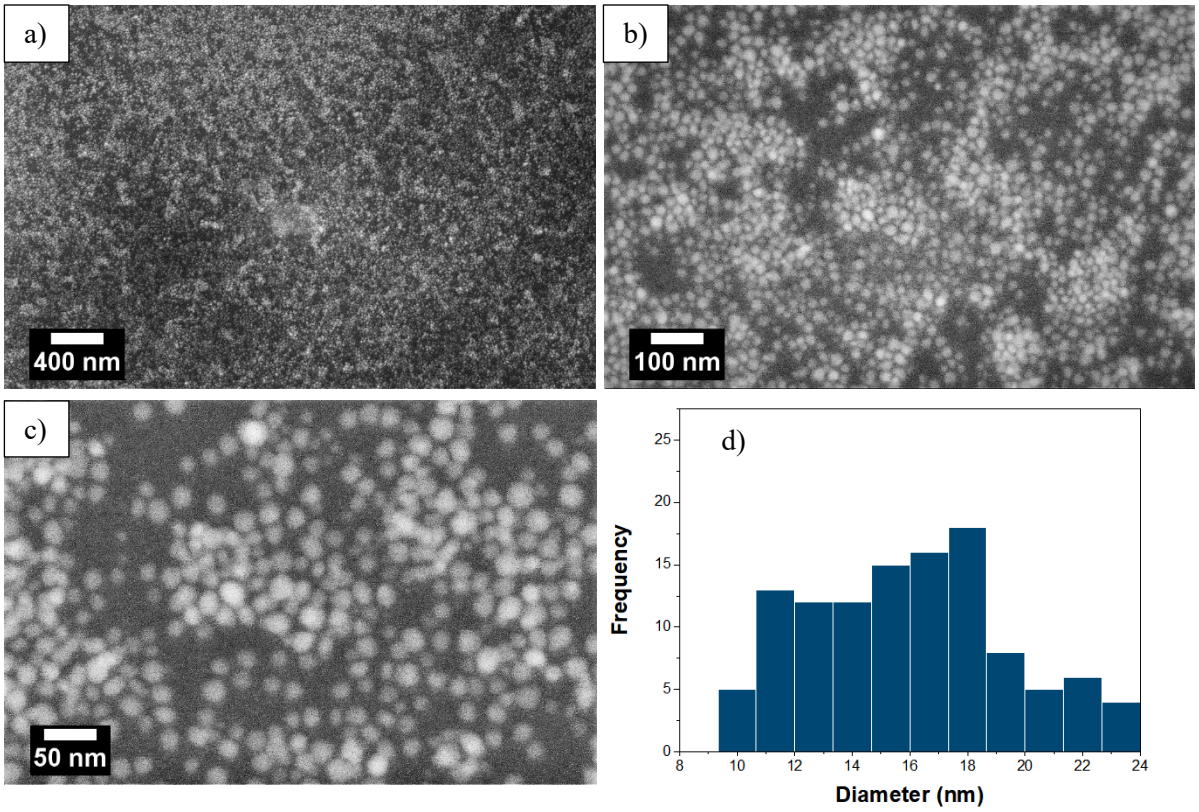

Figure 4-3: SEM images of synthesized AgNPs after blade coating the TOL/IPA bilayer in a) 25KX b) 100KX c) 200KX magnifications. (d) Particle size distribution histogram of the polydisperse AgNPs having an average particle size of (16±3) nm.

DCB/TBA

Ink preparation in this section was based on using DCB as the reducer ink solvent and TBA for dissolving the $AgClO_4.H_2O$. UV-Vis spectrum of the blade coated DCB/TBA film (figure 4-4.a) shows a peak at 477 nm resulting from AgNPs plasmonic absorption. XRD pattern (figure 4-4.b) also shows peaks at $2\theta=37.9°$ and 44° corresponding to (111) and (200) planes of silver, respectively. SEM images in figure 4-5 display polyhedral-shaped NPs over the surface of the glass. The average nanoparticle size is calculated to be 20±6 nm, which is larger than the particles made with TOL/IPA inks.

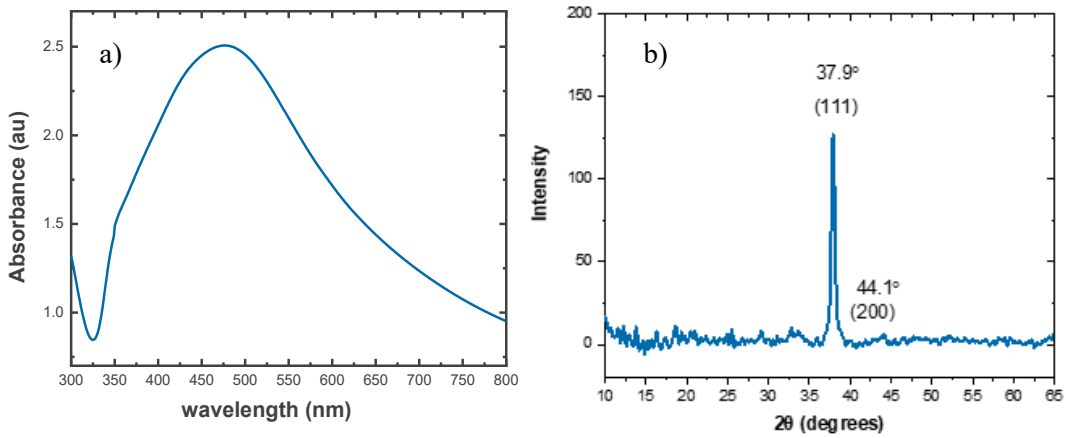

Figure 4-4: Characterization of DCB/TBA bilayer. (a) UV-Vis absorbance spectrum of AgNP films showing plasmon resonance peak at 477 nm, b) XRD spectrum of AgNPs showing distinct peaks at 37.9° and 44° characteristics to silver.

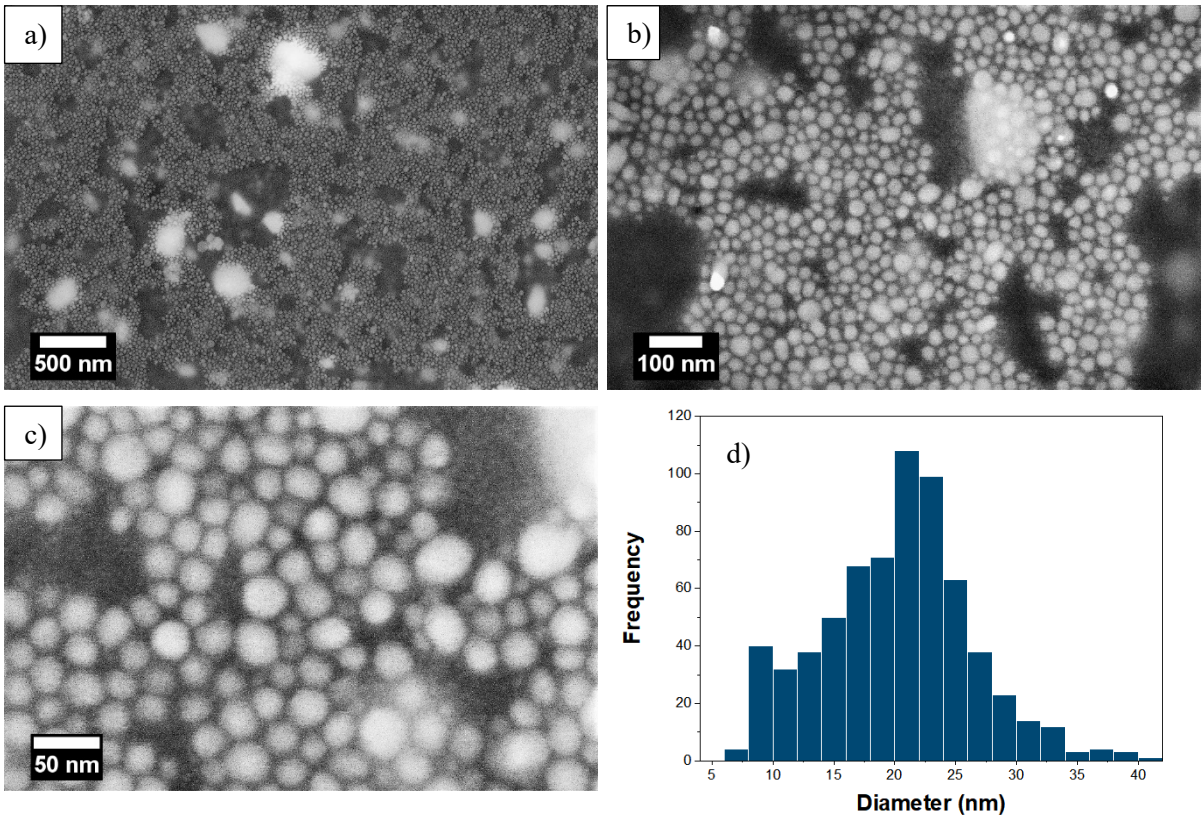

Figure 4-5: SEM images of synthesized AgNPs after blade coating the DCB/TBA bilayer in a) 50KX b) 100KX c) 200KX magnifications. (d) Particle size distribution histogram of the polydisperse AgNPs having an average particle size of (20±6) nm.

TOL/DMSO

The next solvent to examine for the precursor ink was DMSO. However, due to the insolubility of the $AgClO_4$ in DMSO, $AgNO_3$ was used as the silver precursor. TOL containing oleylamine as the reducing agent and DMSO containing $AgNO_3$ as precursor ink were blade coated subsequently. This coating formed a relatively uniform silver colored thin film on the substrate. The plasmonic absorption peak at 442 nm in the UV-Vis spectrum for this sample (figure 4-6.a) indicates the formation of AgNPs. X-ray diffraction peaks at 2θ=37.9° and 44°corresponding to the (111), (200), and (220) planes of crystalline silver are clearly seen in the XRD data of figure 4-6.b. The AgNPs formation is confirmed in the SEM micrographs (figure 4-7). In this case, spherical nanoparticles with an average particle size of 10±1nm and a highly uniform size distribution can be seen on the substrate surface.

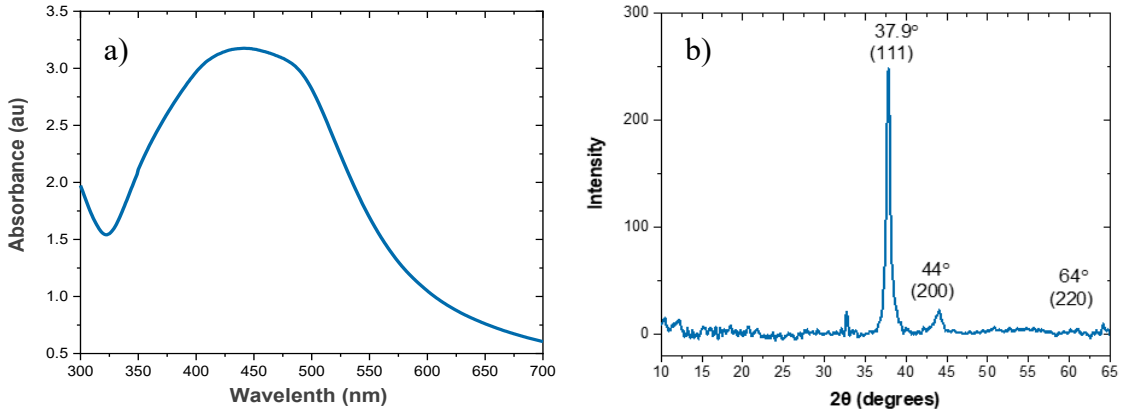

Figure 4-6: Characterization of TOL/DMSO bilayer. (a) UV-Vis absorbance spectrum of AgNP films showing plasmon resonance peak at 442 nm, b) XRD spectrum of AgNPs showing distinct peaks at 37.9° and 44° characteristics to silver.

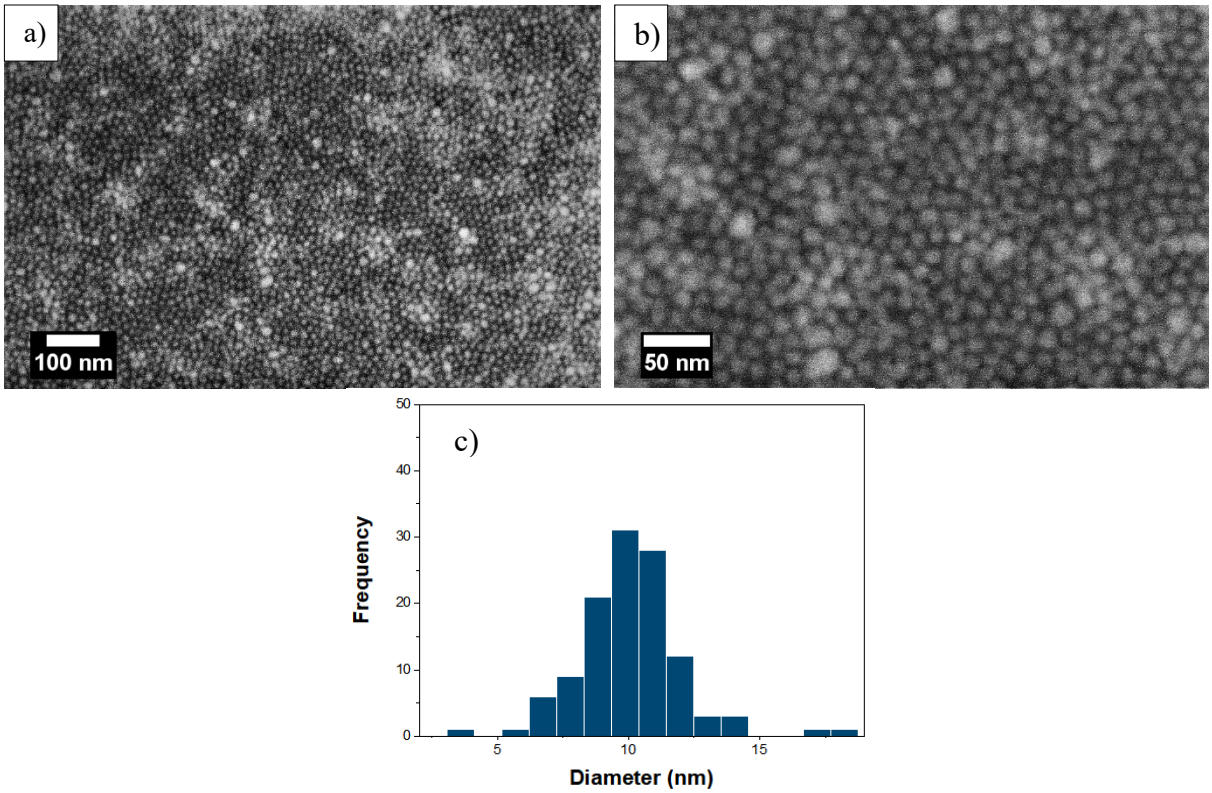

Figure 4-7: SEM images of synthesized AgNPs after blade coating the TOL/DMSO bilayer in a)100k, b) 250k. (d) Particle size distribution histogram of the polydisperse AgNPs having an average particle size of (10±1) nm.

Although all blade coated samples using the various solvent systems formed the AgNPs, they led to different sizes of the NPs and the film coverage. Among these samples, the TOL/DMSO solvent system resulted in NPs having the smallest size and uniform size distribution, with acceptable surface coverage. To analyze the wettability of the inks, their surface tension and contact angle on the glass/Si-wafer were measured (Table 4-1).

Table 4-1: Surface tension and contact angle of inks used in the self-assembly of AgNPs using reactive blade coating technique.

Reducing ink 0.3 OA/Solvent	Surface tension ($mN.m^{-1}$)	Contact angle on glass	Contact angle on Si-wafer
TOL+OA	24.1	<5°	<5°
DCB+OA	29.5±1	<5°	<5°
Ag precursor ink 25mg/ml			
IPA+ $AgClO_4.xH_2O$	21.3±1	<5°	<5°
TBA+ $AgClO_4.xH_2O$	22.3±1	<5°	<5°
DMSO+ $AgNO_3$	39.6±1	(11±2) °	(12±2) °

Toluene (TOL), Oleylamine (OA), 1,2-Dichlorobenzene (DCB), Isopropyl alcohol (IPA) Dimethyl sulfoxide (DMSO), Tert-Butyl alcohol (TBA

All three solvent systems (TOL/IPA, DCB/TBA, and TOL/DMSO) resulted in the synthesis of the self-assembled AgNPs. However, they differ in particle size and thin-film uniformity. For example, TOL/DMSO inks led to smaller particle sizes and more uniform coverage of the coated surface area. A considerable difference in polarity between the two solvents (0.099 for toluene and 0.44 for DMSO) makes them relatively immiscible, and that can lead to the formation of the nanoparticles at the interface between the two ink layers. The solvents immiscibility limits the nucleation of the AgNPs to the interfacial region formed between the two solvents [156]. From table 4-1, it can be seen that the surface tension, as well as the contact angle of the DMSO containing silver precursor ink (<5° nm), are lower than that of the gold precursor ink (35±1°), which leads to better wettability of the coated layers and in turn more uniform films on both glass and Si substrates. Figure 4-8 shows a contact angle of less than 5° for the DMSO silver precursor layer, which indicates the proper wettability of the ink.

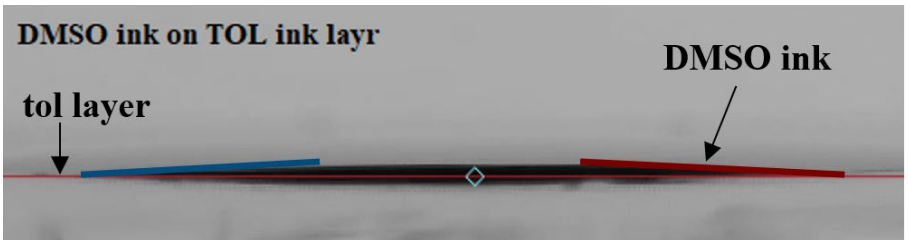

Figure 4-8: Contact angle of DMSO silver nitrate precursor ink on top of TOL reducer ink layer. Red line determines the surface of the TOL blade coated surface where the DMSO ink is dropped (black area).

On the other hand, the TOL/IPA, despite the formation of the nanoparticles, did not result in a uniform film on the substrates. A possible cause for this can be the lower boiling point of IPA (82°C) in comparison with DMSO (189°C) (table 3-1), which leads to faster evaporation of the solvent during the heating process (at 120°C) and in turn, prevents the AgNPs from forming. On the other hand, the higher viscosity of TBA (3.35 cP) compared to other solvents for the precursor inks can be behind the growth of larger size AgNPs in the case of DCB/TBA.

4.1.6 Conclusion

The reactive blade coating process used in this study enabled *in situ* self-assembly of AgNPs where toluene, DCB, IPA, DMSO, and TBA were used as solvents used in these experiments. Silver salts, including silver perchlorate hydrate as the reactant agent and oleylamine as the reducing,

were used for the synthesis of AgNPs. It was concluded from the data that the size of NPs is dependent on the solvent system used. For example, using TOL/DMSO and TOL/IPA inks resulted in an average AgNPs size of 10 nm and 16 nm, respectively. This difference in size can be attributed to the difference in polarity between the reducer and precursor solvents leading to their immiscibility, which in turn allows the nucleation of the AgNPs at the interfacial region between the two solvents.

Based on the experiments above, it can be concluded that reactive blade coating enables *in situ* synthesis of the AgNPs. Such encouraging results from a roll-to-roll compatible coating technique promise to produce AgNPs at a much lower cost than currently possible using traditional liquid chemistry approaches. However, in the near term, several aspects have to be improved in the lab before our approach is ready for prime-time market implementation. Some of the topics that require more research include improvement of thin-film quality and uniformity over large substrate area and surface modification and functionalizing the substrates to allow better spreading and coverage of the coated layers.

4.2 The antiviral response of the as-synthesized AgNPs against SARS-Cov-2 Virus

The potential of the reactive blade-coated self-assembled AgNPs (R-AgNPs) as microbial disinfectants is demonstrated in what follows. Nowadays, there is a desperate need for innovations that can contribute rapidly to limit the spread of COVID-19 and its more infectious new variants detected in many places of the globe.

Reactive blade coated AgNPs on glass substrates were used to estimate their antiviral effect against the SARS-Cov-2 virus, which causes the COVID 19 illness. However, due to the lack of Biosafety Level 3 laboratories at uOttawa, we limit ourselves to the use of Human Coronavirus 229E (HCoV-229E) as a SARS-Cov-2 surrogate, which can be done in the Level 2 Biosafety facility at uOttawa. HCoV-229E belongs to the family Coronaviridae, the same as the SARS-Cov-2. Both are enveloped, positive-sense-single stranded RNA types of viruses, and their genome comprises 26-32 kilobases, which is the longest known viral RNA genome [158].

As shown earlier, blade coating the TOL/DMSO solvent system resulted in monodispersed nanoparticles with better film coverage compared to other solvents. This approach was adopted in the fabrication of AgNPs thin film used in this antiviral study. For comparison, a commercial silver nanoparticle ink formulated for inkjet printing (C-AgNPs) was blade coated on glass and silicon substrates. To evaluate the antiviral efficacy of the AgNPs, plaque assay was performed using HCoV-229E stock. Plaque assay provides a quantitative measurement of the infectious virus after being in contact with the AgNPs (as an antiviral agent). In this method, a monolayer of host cells is infected with serial dilution (stepwise diluted concentrations) of the virus stock and, after a right period (3-14 days), plaques formed in the cell culture are quantified and presented as plaque-forming units per ml/inch (PFU/ml or PFU/inch). A viral plaque, in general, is a group of lysed cells destructed due to infection and surrounded by uninfected cells. This infected area can become visual via an optical microscope or by eyes upon using proper staining of the infected monolayer. The plaque assay determines the concentration of viruses (viral titer) in a pool at which they are capable of infecting the host cells.

4.2.1 Materials

HCoV-229E virus (ATCC#VR-740) and L132 cell line (ATCC® CCL-5) were obtained from Bioanalytical and Molecular Interaction (BioAMI) Laboratory at the Department of Chemistry and Biomolecular Sciences at uOttawa. The L-132 cell line was derived from human embryonic lung tissue and grown in α-EM (GIBCO-BRL cat#41600-016) medium containing L-glutamine and 10% fetal bovine serum (FBS). The culture medium and neutral red Cat# N6264- 50ML for staining viable cells were obtained from Sigma-Aldrich (Canada). Silver nanoparticle conductive ink was obtained from BotFactory (US).

4.2.2 Blade coating of thin films AgNPs

A 30% (V/V) solution of OA and TOL and 50 mg/ml solution of AgNO3 in DMSO were used for reactive blade coating of AgNPs on glass substrates. The increased concentration of the reactants was necessary to improve the AgNPs film coverage and uniformity. In this case, a higher concentration of reducing ink and precursor ink was used. C-AgNPs ink was also blade coated on glass substrates. The post-coating heating treatment step (1h at 80C° and 3h at 120C°) was carried to obtain thin films of C-AgNPs. Morphology and size distribution of the nanoparticles were analyzed in both cases.

4.2.3 Virus titration procedure

All testing and results was carried out and reported following ASTM E1153-03 (Standards Test Method for Efficacy of Sanitizers Recommended for Inanimate Non-Food Contact Surfaces) and CAN/CGSB-2.161-97, (Assessment of Efficacy of Antimicrobial Agents for use on Environmental Surfaces and Medical Devices). Figure 4-9 demonstrates the process of virus titration briefly described as follows. The first stage involves the propagation of the HCoV- 229E. For this purpose, the L-132 cell line derived from human embryonic lung tissue was first subcultured and grown in a T-75 flask containing α-EM (GIBCO-BRL cat #41600-016) in the presence of L-glutamine and 10% fetal bovine serum (FBS), then incubated to form a confluent monolayer. This was followed by adding 200 µL of virus suspension having a multiplicity of infection (MOI) of one plaque per cell to the flask and incubating for one hour at cell culture incubator conditions of 35C° and 5% CO2 to propagate the virus on the cells. Afterward, the solution was refreshed with α-EM having 2% FBS and incubated before the appearance of any

cytopathic effect. Within three days, the infected cells became rounded-up, detached from the flask, and were pipetted out for harvesting the propagated virus. To purify the virus from the lysed cells, the freeze-thawing cycle of the cell suspension was carried out three times, followed by centrifugation at 1000×g for 10 minutes. An aliquot of the harvested virus pool was titrated by plaque-forming assay, where the rest aliquots were stored at 4°C. Plaque assay was performed to find the proper dilution of the virus to be used in the antiviral activity test of the AgNPs.

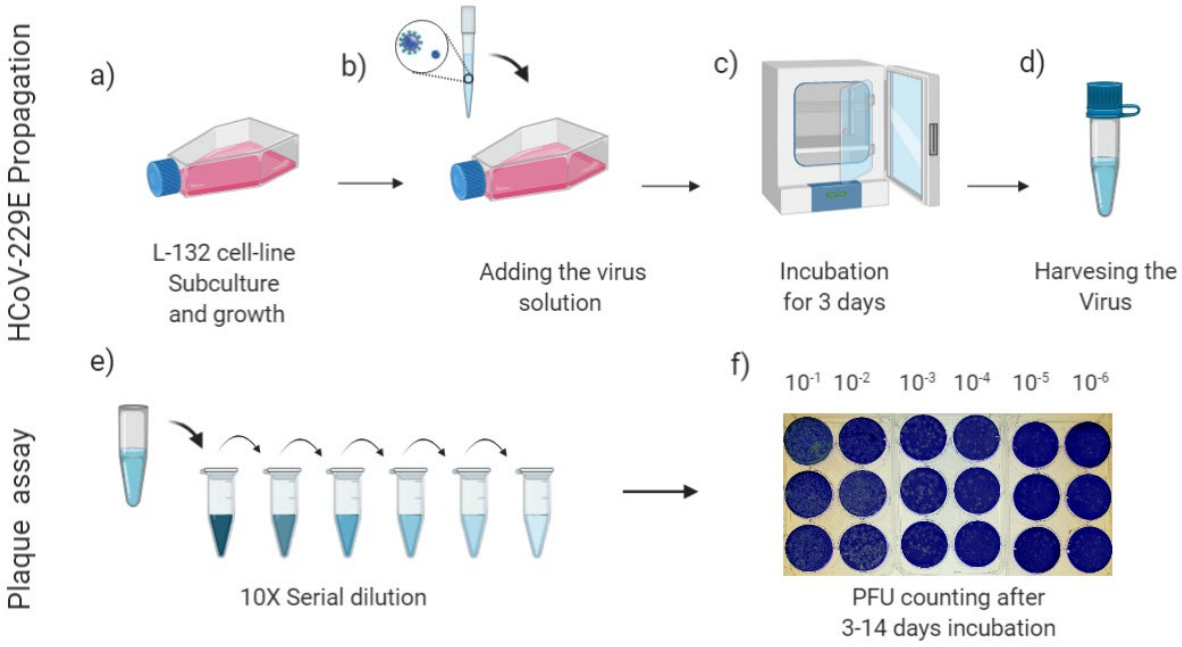

Figure 4-9: Schematic drawing of virus titration process. a) Subculturing L-132 cell line in T-75 flask to form a confluent monolayer. b) Adding the virus suspension to the flask on the cell monolayer. c) Incubating the virus-exposed monolayer (at 35C° and 5% CO2) for three days to propagate the virus. d) Harvesting virus by repeating freeze-thaw cycle and centrifugation. e) 10X Serial dilution of the virus pool. f) Placing the six 10X dilutions onto the six-well plates covered with the host cells (3times repeated). 3-14 days of incubation to see the visible plaques formed on the well. (The image is created in BioRender)

The plaques formed by titrating human coronavirus 229E in 10X serial dilutions incubated with L-132 cells are shown in the figure 4-10. The infected cells were monitored by a microscope to define the right time for plaque counting. The right time is when the survived viruses had the opportunity to make visible plaques but not diffused into each other. The image shows the plaques formed after eight days of incubation. The cells were fixed by 10% formaldehyde and stained by 0.5% crystal violet to visualize countable plaques. Here the two 10-fold dilutions (10^{-3}) seem to have resulted in the proper number of plaques.

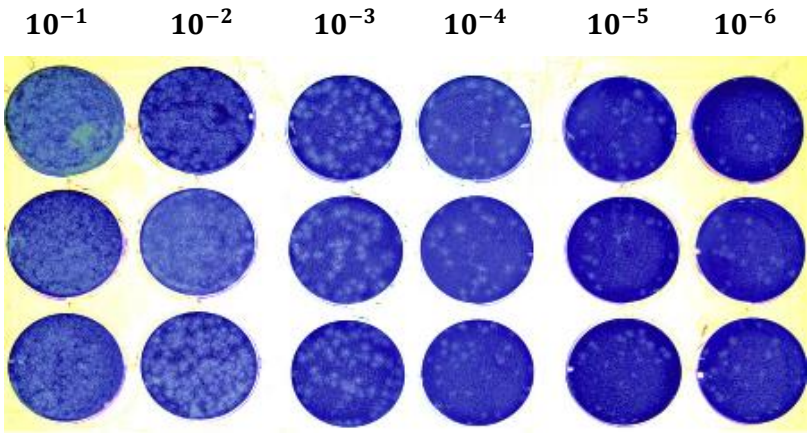

Figure 4-10: Plaques forming after eight days of infecting the L-132 cells with the 10X dilutions of HCoV-229E (repeated three times). Virus-exposed cell monolayers are stained with crystal violet to visualize the formed plaques.

4.2.4 Efficacy of virucidal activity of the AgNPs films

The triplicated tests were conducted to examine the disinfecting efficiency of the reactive self-assembled silver nanoparticles (R-AgNPs) as well as the commercial silver nanoparticle (C-AgNPs) ink blade coated on glass substrates (1x1inch). Figure 4-10 shows the schematic drawing of the virucidal efficacy test used to study the antiviral activity of the blade coated AgNPs. Two 10X dilutions of the HCoV-229E stock were prepared in a soil load with a final concentration of 5% FBS. A 40µL volume of the resulting mixture was poured on the AgNPs blade coated glass slides and incubated for three different contact times of 1, 10, and 30 minutes, respectively. After each contact time, virus-exposed slides were recovered in 1000 µL of the media. The suspensions were then transferred into 10X serial dilution vials and subjected to plaque-forming assay. Both synthesized AgNPs and commercial AgNPs ink coated on glass substrates were used for PFU assay to evaluate their sanitizing effect on the virus. All the control samples used in the experiments were also prepared by incubating the same virus pool on glass slides but without the nanoparticles.

The plaque-forming assays were conducted by placing the 100 µL of appropriate virus dilution on the L-132 monolayer cultured in six-well plates. This was followed by 60 minutes incubation of the well plates at 35°C in a CO_2 atmosphere. 2mL of medium supplemented with 2% FBS and % low melting agarose replaced the solution in each well, proceeding the incubation at 35°C and 5% CO2. On the fourth day, the second layer of agarose media, including 0.03% of neutral red, was

added. Neutral red penetrates the cell membrane and accumulates in the lysosomes of the viable cells. Therefore, it stains the live cells and enables monitoring of the formation of the plaques. Upon developing the plaques, a 10% buffered formalin was added for the fixation of the cells. Three hours later, after removing the overlays and washing the cells, 0.5% crystal violate added for staining the cells and visualizing the plaques. By rinsing the plates, the plaques appeared to have a shape specific to the Human coronavirus 229E. The visible plaques were counted.

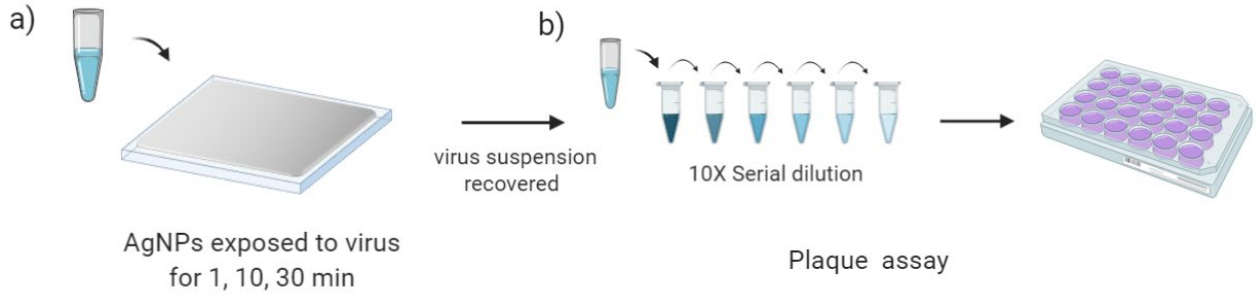

Figure 4-11: Antiviral efficacy of the AgNPs films assessment. a) Exposing the virus titer to both R-AgNPs and C-AgNPs blade coated slides for 1, 10, and 30 minutes. b) Plaque assay. The virus pool after exposure to AgNPs virus was recovered and subjected to plaque assay by 10X serial dilution of the virus suspension and incubation with the host cell monolayer for 3-14 days to be able to visualize the plaques formed on the well. (The image is created in BioRender)

4.2.5 Results and discussion

In what follows, the results were obtained from three independent experiments are reported as mean values ± mean of standard deviations. Figure 4-12. a and b shows the SEM images of the reactive blade coated AgNPs with an average particle size of (26±5) nm (figure 4-9.c). SEM images of the blade coated C-AgNPs, and their size distribution are illustrated in figure 4-12 d-f. In this case, the average size of the NPs is 30±8 Reactive blade coated AgNPs seem to have a better spherical shape uniformity and are monodispersed compared to the films obtained from the blade coated C-AgNPs.

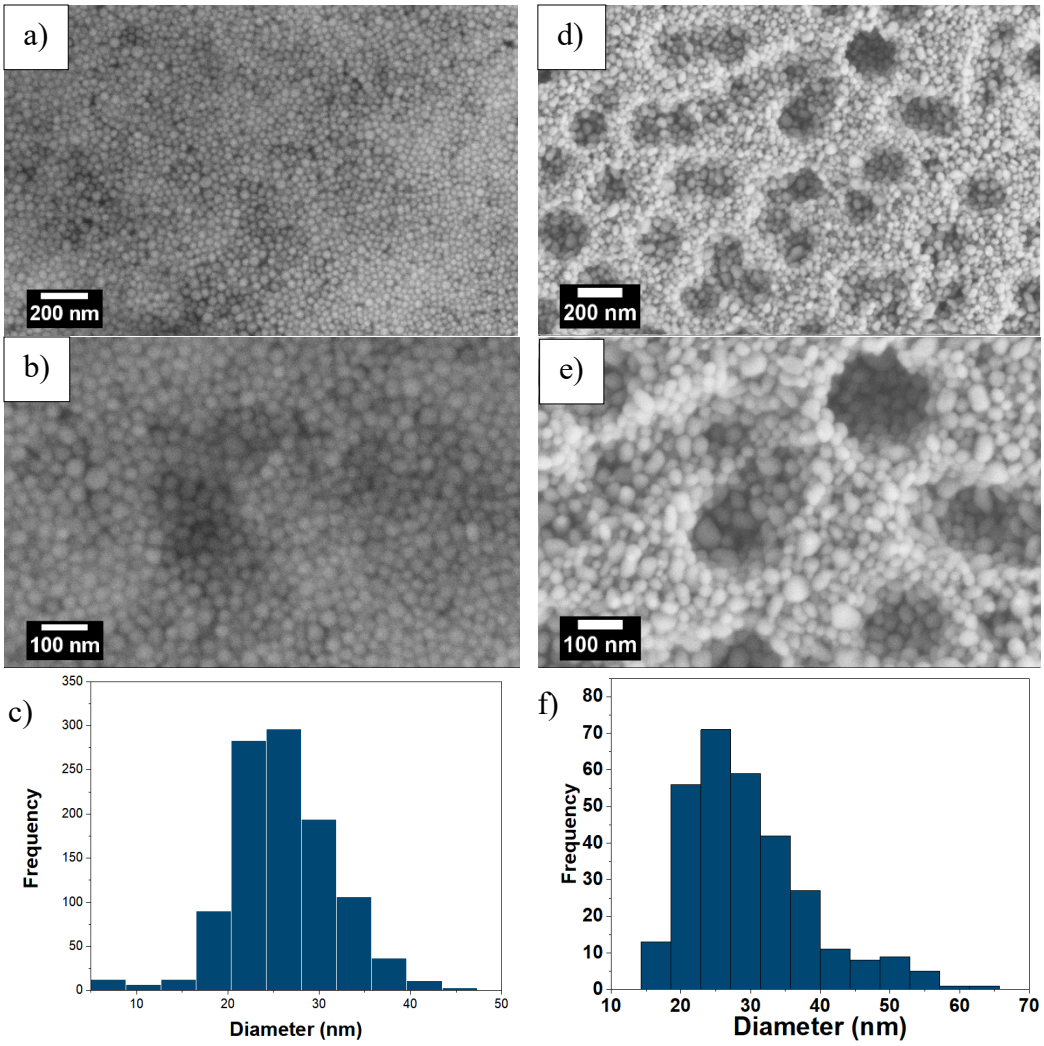

Figure 4-12: (a) and (b) SEM images of R-AgNPs showing closed pack spherical shape of NPs distributed uniformly on the surface, (c) particle size distribution of the R-AgNPs with an average diameter of (26±5) nm. (d) and (e) SEM images of blade coated C-AgNPs showing NPs distributed. The black holes seem to be caused as a result of the vaporization of the solvent. (f) The particle size distribution of C-AgNPs with an average diameter of (30±8) nm.

Figure 4-13 displays the microscopic images of the plaques developed by HCoV-229E after two (a) and eight (b) days, after incubation within the L-132 cell monolayer, which was stained with neutral red. Live cells can be seen as red dots spread on the well plate. However, after eight days of infection with the HCoV-229E, the number of viable cells has decreased, and the gray area represents the formed plaques as a result of the infection and the cells' death. This shows the right time to count the formed plaques.

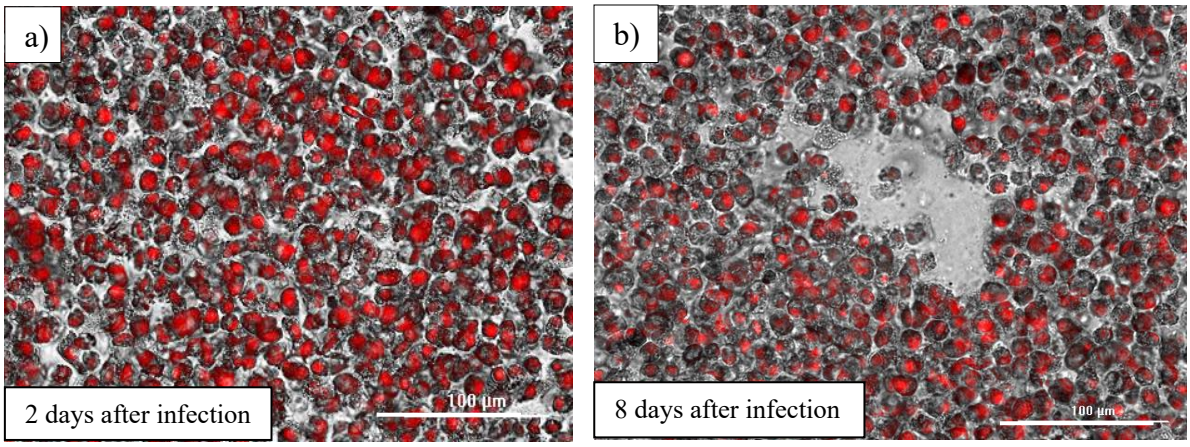

Figure 4-13: Microscopic image of the infected monolayer of the L-132 cells by HCoV-229E virus after (a) two days and (b) eight days of incubation showing plaque formation.

To evaluate the antiviral effect of reactive blade coated AgNPs thin-film on the HCoV-229E virus, the plaque-forming assay was performed. The bar graph in figure 4-14 illustrates the log value of geometric means of the plaque-forming unit (PFU) per inch of the HCoV-229E after contacting the AgNPs layer for 1, 10, and 30 minutes respectively, representing their infectivity compared to the control samples. As can be seen, the infectivity has been reduced for each contact time. Geometric means of the PFU/inch has declined from 7.05 PFU/inch for the control sample to 5.96 PFU/inch and 5.68 PFU/inch after 1 minute and 10 minutes incubation with the synthesized AgNPs, respectively. A more significant decrease to 3.33 PFU/inch is seen within 30 minutes of the virus contact with the AgNPs. The control sample for 30 min contact had a value of 7.2 PFU/inch.

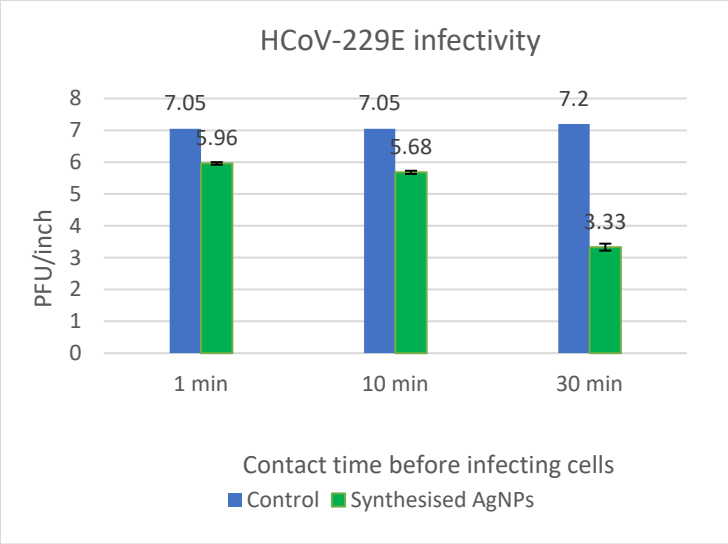

Figure 4-14: Log geometric mean of the HCoV-229E infectivity after contacting the reactive blade coated AgNPs (green) for three intervals of 1, 10, and 30 mins compared to that of control samples where no contact with the virus was initiated (blue)

Figure 4-15 illustrates the log reduction graph as well as the percentage reduction of the virus infectivity after they were in contact with reactive printed AgNPs. Every one log reduction is associated with a percent reduction of the PFU, as presented in table 4-2. This reduced number represents the reduction of the infectivity of the virus. Consequently, it determines the efficiency of the AgNPs to disinfect or weaken the strength of the virus. Log reduction is calculated as shown in formula 1 [159].

- Formula 1: $Log\ Reduction = \log_{10}(\frac{A}{B})$

  or

  $$Log\ Reduction = \log_{10}(A) - \log_{10}(B)$$

A and B are the number of PFU/mL achieved before and after the virus exposure to AgNPs.

Table 4-2: the percent reductions assigned to each number of logs reduction

Log reduction	Number of PFUs	Percentage reduction	Times smaller
0 log (Log0)	1 000 000	0%	N/A
1 log (Log1)	100 000	90%	x 10
2 logs (Log2)	10 000	99%	x 100
3 logs (Log3)	1 000	99.9%	x 1 000
4 logs (Log4)	100	99.99%	x 10 000
5 logs (Log5)	10	99.999%	x 100 000

By incubation of the virus contacting AgNPs for 1 min before infecting the cells, the assay shows a reduction of 1.09 logs (figure 4-14) which is assigned to 91.89% reduction of the HCoV-229E titer. As the contact time increased to 10 minutes, a rise in log reduction to 1.37 was observed, indicating a 95.75% reduction in the number of PFUs. Finally, after 30 min contact time, a log reduction of 3.88 in virus activity is measured. This corresponds to ca. 99.99% of the virucidal effectivity of the silver nanoparticles in disinfecting the virus. This experiment clearly indicates the effectiveness of reactive blade-coated AgNPs in fully incapacitating the infectious activity of the HCov-229E virus within 30 min.

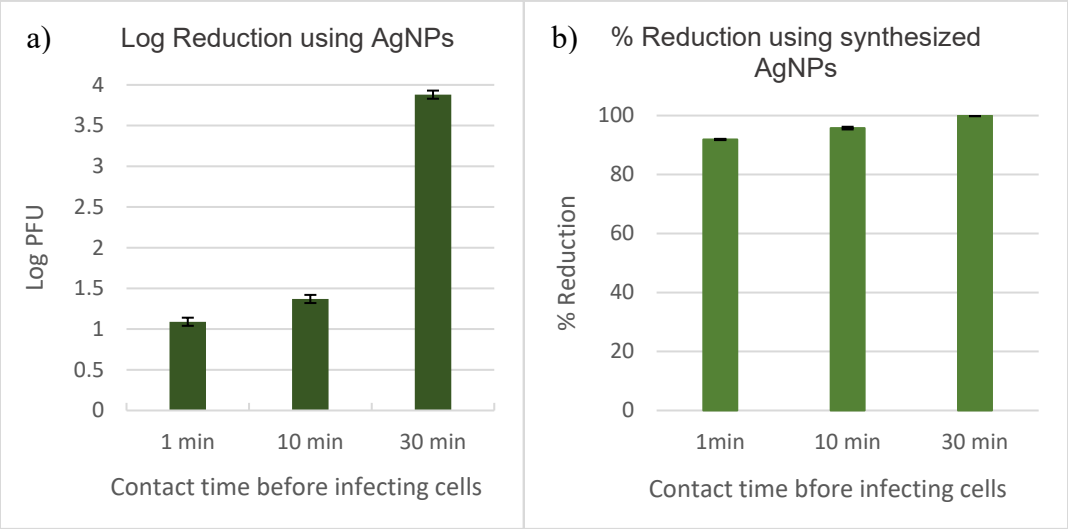

Figure 4-15: (a) Log reduction and (b) percentage reduction graph of the virus infectivity after they were in contact with the reactive blade coated AgNPs for 1, 10, and 30 min, respectively.

Figure 4-16 shows the plaque-forming ability of the HCoV-229E after 1, 10, and 30 min of contact with the blade coated C-AgNPs film (as mentioned in previous sections) and right before incubation with the cell monolayer. Log form of geometric means of the PFU/inch has dropped from 7.05 PFU/inch for the control sample to 5.73 and 5.97 after 1 minute and 10 minutes incubation with the synthesized AgNPs, respectively. For the samples with 30 min contact, the value has declined notably from 7.2 for the control sample to 3.64 PFU/inch.

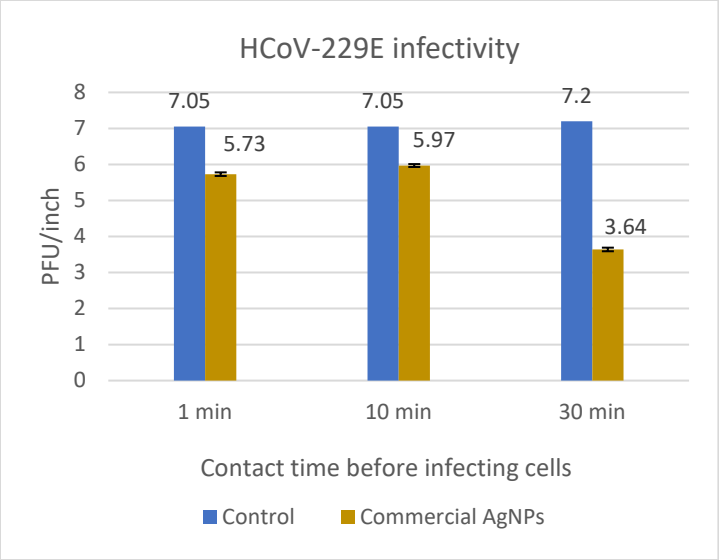

Figure 4-16: Log geometric mean of the HCoV-229E infectivity after contacting the commercial AgNPs film (brown) for three intervals of 1, 10, and 30 mins compared to the control samples representing no contact of the virus with the NPs (blue).

Virus log and percent reduction of the C-AgNPs ink are presented in figure 4-17. a and b, respectively. A log reduction of 1.32, 1.09, and 3.56 can be seen after incubating the virus for 1, 10, and 30 min with the AgNPs film before infecting the cells, which corresponds to a 95.25%, 91.83%, and 99.97% reduction in the viral strength to cause infection in the cells during the respective exposure time mentioned above.

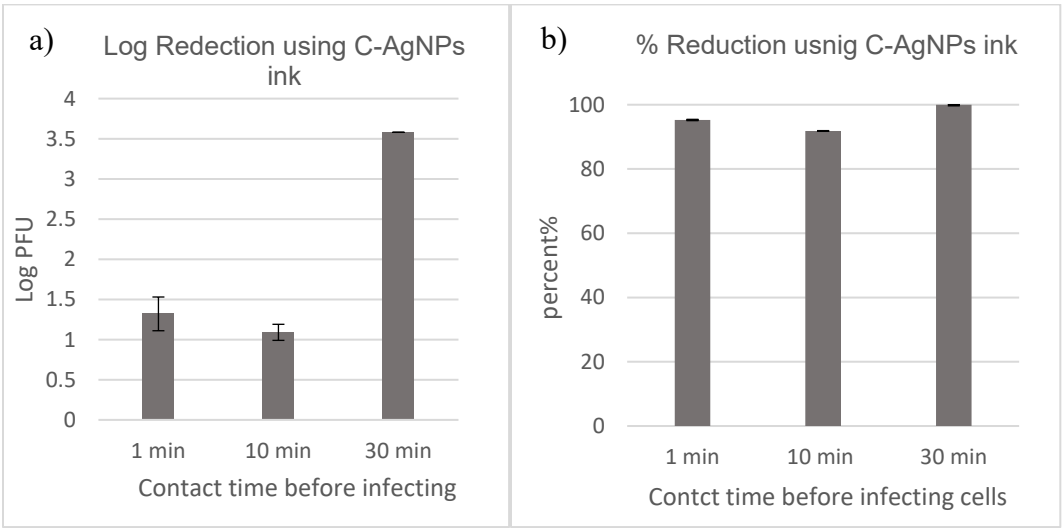

Figure 4-17: (a) log reduction and (b) percentage reduction graph of the virus infectivity after they were in contact with the blade coated commercial AgNPs for 1, 10, and 30 min.

Table 4-3 summarizes the results of the assay presented earlier. The results show a reduction in the log PFU/inch values for every contact time with both the R-AgNPs and C-AgNPs compared to control samples with no exposure to the AgNPs. The reduction is more significant for samples with 30 mins of contact time (99.99% for R-AgNPs and 99.97% for C-AgNPs), which shows the strong infectivity effect of the AgNPs in this period.

Table 4-3: values for Log geometric mean of PFU/inch, log reduction, and %reduction achieved from plaque-forming assays after exposing the virus titer to the AgNPs blade coated slides for 1, 10, and 30 minutes for both R-AgNPs and C-AgNPs.

	Log (PFU/inch)						Log Reduction			% Reduction		
Contact time (min)	1		10		30		1	10	30	1	10	30
	Control	test	Control	test	Control	test						
R-AgNPs	7.05 ± 0.93	5.96 ± 0.04	7.05 ± 0.93	5.68 ± 0.05	7.20 ± 0.79	3.33 ± 0.11	1.09 ± 0.05	1.37 ± 0.05	3.88 ± 0.05	91.98 ± 0.34	95.75 ± 0.05	99.99 ± 0.11
C-AgNPs	7.05 ± 0.93	5.73 ± 0.05	7.05 ± 0.93	5.97 ± 0.04	7.20 ± 0.79	3.64 ± 0.05	1.32 ± 0.84	1.09 ± 0.10	3.56 ± 0.00	95.25 ± 0.21	91.83 ± 0.01	99.97 ± 0.10
Reactive coated AgNPs(R-AgNPs), Commercial AgNPs (C-AgNPs)												

Although the biological mechanisms for disinfection and cytotoxicity are beyond the scope of this thesis, it is worth mentioning that the disinfecting mechanism of the AgNPs remains unclear. Several recent studies consider the interaction of the AgNPs with the structural proteins on the extracellular viruses as the main source of inhibiting viral infection. In this regard, it is suspected that the interaction between the virus and AgNPs prevents the attachment, and consequently, entry of the virus to the target cell and/or destroys the structural integrity of the virions by damaging their surface proteins [157, 160].

AgNPs of <10 nm have demonstrated cytotoxicity even at low concentrations, for instance, 2ppm, while bigger particles (>10 nm) tend to be safer in terms of cytotoxic reaction at the same concentrations [157]. In our case, we anticipate that an average AgNPs size larger than 25 nm obtained by reactive blade coating of self-assembled AgNPs should provide a safer margin of cytotoxicity than the published case of 10 nm. However, experimental results in this regard are needed.

In summary, plaque assay results exhibited a significant decrease in virus infectivity after contacting AgNPs blade coated glass slides with reactively self-assembled and commercial

AgNPs, respectively. Increasing the contact time from 1 to 30 min led to a greater reduction of infectivity of the virus, reaching a 99.99% effectiveness after 30 min. This is a strong testament to the vast commercial potential of our approach, which is far cheaper and has lower manufacturing energy and environmental footprint than other commercially available approaches of AgNPs ink preparation.

4.2.6 Conclusion

Using a self-assemble and uniform film of AgNPs grown on glass substrates via reactive blade coating of TOL/DMSO (reducing/precursor) inks lead to highly promising antiviral effects against the HCoV-229E virus, a SARS-CoV-2 surrogate. In this case, the AgNPs films resulted in more than 90 % reduction in infectivity of the virus after contacting the film for 1 min and reaching 99.99 % value after 30 min. Such results are very encouraging and open up the possibility of low-cost fabrication of AgNPs (and other materials) for a wide range of applications ranging from antimicrobial encapsulation and packaging to self-cleaning personal protective equipment (including face masks), to mention a few.

Chapter 5. Conclusion and Future works

5.1 Conclusion

This study aimed to introduce the potential capability of the large-scale coating technique in the direct fabrication and deposition of thin films of metallic nanoparticles. It was shown that *in-situ* self-assembly of the nanoparticles using metal precursors and a reducing agent is indeed possible using blade coating. The use of starting chemical materials in the coating process as inks and their respective chemical interaction to yield uniform nanoparticles demonstrates the promise of such reactive coating techniques in the manufacturing of metal-based nanoparticles. Two systems were targeted namely gold and silver nanoparticles.

To fabricate AuNPs thin film, oleylamine as the reducing agent and $HAuCl_4.xH_2O$ as the reactant was prepared as inks and blade coated subsequently (i.e., first coating the reducer followed by the precursor) on glass or silicon substrates. After the post-coating heat processing step, SEM imaging, UV-Vis analysis, and XRD crystalline phase analysis revealed the formation of crystalline AuNPs with relatively uniform size distribution on the substrate. In this regard, AuNPs with an average size of 10±2 nm were fabricated using TOL and IPA as the solvents for reducing and precursor agents, respectively. Due to their immiscibility, such solvent facilitated the formation of smaller particles and a more uniform coating on the substrates compared to the other organic solvents used in this study. By changing the concentrations of the reactants or increasing the number of the coated layers, it is possible to control the average particle size. In this regard, particles with an average diameter of 11-12 nm were formed by increasing the concentrations of the reactants while repeating the blade coating process for up to 6 alternating layers of reducer and precursor inks lead to an increased average size of ca. 30 nm.

To demonstrate the use of AuNPs thin films in biomedical engineering applications, a biosensing platform for detecting elevated concentrations of glucose in an aqueous solution using the LSPR effect of the AuNPs was designed. Red shifts were detectable in the plasmon resonance peaks of the NPs after immersing the films in different concentrations of glucose solutions, an indication of the change in the dielectric medium around the NPs due to the presence of glucose, attesting to the functionality of the reactively coated AuNPs film in such an application. As low as 5mg/dL of glucose concentration was detectable, which resulted in a 3 nm red shift in the LSPR peak. By

increasing the glucose concentration to 50 mg/dL, a corresponding increase in the red shift of the wavelength peaks was recorded, which can be used to calibrate the detection range of such biosensors.

To demonstrate the suitability of reactive blade coating of NPs in meeting the urgent need of limiting the spread of COVID-19 illness resulting from the SARS-CoV-2 virus, we evaluated the efficacy of the resulting films of NPs in disinfecting the virus. In this case, reactive blade coated AgNPs thin film on the glass and silicon substrates were used. The self-assembled NPs were synthesized with a relatively uniform size distribution in a range of 10-20 nm. The AgNPs starting inks relied on (TOL+ oleylamine) as the reducer and (DMSO+$AgNO_3$) as the precursor, which were blade coated consecutively. It is noted that this ink system resulted in the most uniform film coverage, thus the reason for its selection for the virus disinfection application.

uOttawa Level-2 Biosafety facility does not allow for the use of live SARS-CoV-2. In fact, there are very few locations in Canada that allow such experiments. However, they are not readily accessible to test the coated AgNPs in an expedited manner. Fortunately, most researchers worldwide use a surrogate virus, namely HCoV-229E, which belongs to the family of SARS virus, including SARS-CoV-2. This provided us with unlimited access to test and optimize our thin films of NPs towards the optimum kill rate of the virus. In fact, the resulting virucidal analysis of the reactive blade coated AgNPs showed a significant reduction of 99.99% in HCoV-229E infectivity after being in contact with the AgNPs for 30 min. Most commercial applications require a 99.9% kill rate. It is worth noting that the results were comparable to those obtained from a blade-coated film made with a commercial silver nanoparticle ink. This is an important aspect of the reactive approach, which positions it to be suited for an on-demand application and provides a longer shelf life of starting inks and more control on the size of the NPs as opposed to an already made NPs ink with fixed nano-particle size.

5.2 Future works

Blade coating is a solution-based thin-film fabrication technique applicable to industrial-scale fabrication. This research suggests the reactive blade coating process for the large-scale synthesis of metallic nanoparticles. Although it resulted in the fabrication of well-defined nanoparticles with an average particle size of less than 20 nm, challenges in large-scale coating uniformity and wettability of inks remain to be addressed. Such challenges can be mitigated by future research focusing on developing a proper surface modification of the substrates (with functional groups) prior to the first coating step and adding the proper surfactants to provide optimum wetting of consequent layers in order to maintain proper size uniformity over the coated area. Another existing application that needs to be addressed is to utilize such an approach in the manufacturing of self-cleaning (disinfecting) personal protective equipment including face masks.

Although the focus was on reactive blade coating, the results here are easily extendable to other roll-to-roll coating/printing techniques, including, but not limited to, screen printing, gravure and flexography, slot-die, etc. All of such reactive coating/printing techniques have a great potential not only to produce low-cost NPs and their films due to their mass-production scale but also to be environmentally friendly advanced manufacturing approaches in biomedical engineering applications due to their low carbon footprint and high efficiency of starting materials use (minimum waste products).

References

[1] S. Syama and P. Mohanan, The Promising Biomedical Applications of Engineered Nanomaterials, in *Handbook of Nanomaterials for Industrial Applications*, Elsevier, 2018.

[2] M. Abd Elkodous *et al.*, Therapeutic and diagnostic potential of nanomaterials for enhanced biomedical applications, *Colloids and Surfaces B: Biointerfaces*, vol. 180, pp. 411–428, 2019.

[3] K. Shrivas, A. Ghosale, P. K. Bajpai, T. Kant, K. Dewangan, and R. Shankar, Advances in flexible electronics and electrochemical sensors using conducting nanomaterials: A review, *Microchemical Journal*, vol. 156, p. 104944, 2020.

[4] S. Sahani and Y. Chandra Sharma, Advancements in applications of nanotechnology in global food industry, *Food Chemistry*, p. 128318, 2020.

[5] R. and M. ltd, Nanomaterials - Market Analysis, Trends, and Forecasts, Oct. 2019. https://www.researchandmarkets.com/reports/344105/nanomaterials_market_analysis_trends_and (accessed May 09, 2020).

[6] B. Pelaz *et al.*, The State of Nanoparticle-Based Nanoscience and Biotechnology: Progress, Promises, and Challenges, *ACS Nano*, vol. 6, no. 10, pp. 8468–8483, 2012.

[7] Nanomaterials Market, Growth, Trends, and Forecast (2020 - 2025), https://www.mordorintelligence.com/industry-reports/nanomaterials-market

[8] S. Edebali, Y. Oztekin, and G. Arslan, Metallic Engineered Nanomaterial for Industrial Use, in *Handbook of Nanomaterials for Industrial Applications*, Elsevier, pp. 67–73, 2018.

[9] L. A. Kolahalam, I. V. Kasi Viswanath, B. S. Diwakar, B. Govindh, V. Reddy, and Y. L. N. Murthy, Review on nanomaterials: Synthesis and applications, *Materials Today: Proceedings*, vol. 18, pp. 2182–2190, 2019.

[10] A. Mtibe, T. H. Mokhothu, M. J. John, T. C. Mokhena, and M. J. Mochane, Fabrication and Characterization of Various Engineered Nanomaterials, in *Handbook of Nanomaterials for Industrial Applications*, Elsevier, pp. 151–171, 2018.

[11] K. Khalid *et al.*, Advanced in developmental organic and inorganic nanomaterial: a review, *Bioengineered*, vol. 11, no. 1, pp. 328–355, 2020.

[12] J. Yang *et al.*, Carbon Dot-Based Platform for Simultaneous Bacterial Distinguishment and Antibacterial Applications, *ACS Appl. Mater. Interfaces*, vol. 8, no. 47, pp. 32170–32181, 2016.

[13] K. McNamara and S. A. M. Tofail, Nanoparticles in biomedical applications, *Advances in Physics: X*, vol. 2, no. 1, pp. 54–88, 2017.

[14] R. Arvizo, R. Bhattacharya, and P. Mukherjee, Gold nanoparticles: opportunities and challenges in nanomedicine, *Expert Opinion on Drug Delivery*, vol. 7, no. 6, pp. 753–763, 2010.

[15] S. A. Bansal, V. Kumar, J. Karimi, A. P. Singh, and S. Kumar, Role of gold nanoparticles in advanced biomedical applications, *Nanoscale Adv.*, 2020.

[16] N. Elahi, M. Kamali, and M. H. Baghersad, Recent biomedical applications of gold nanoparticles: A review, *Talanta*, vol. 184, pp. 537–556, 2018.

[17] Fen-Ying Kong, Jin-Wei Zhang, Rong-Fang Li, Zhong-Xia Wang, Wen-Juan Wang, and Wei Wang, Unique Roles of Gold Nanoparticles in Drug Delivery, Targeting and Imaging Applications, *Molecules*, vol. 22, no. 9, p. 1445, 2017.

[18] X. Yu, Y. Jiao, and Q. Chai, Applications of Gold Nanoparticles in Biosensors, *Nano LIFE*, vol. 06, no. 02, p. 1642001, 2016.

[19] Y. Kumari *et al.*, Gold nanoparticles: New routes across old boundaries, *Advances in Colloid and Interface Science*, vol. 274, p. 102037, 2019.
[20] K. Sztandera, M. Gorzkiewicz, and B. Klajnert-Maculewicz, Gold Nanoparticles in Cancer Treatment, *Mol. Pharmaceutics*, vol. 16, no. 1, pp. 1–23, 2019.
[21] V. Amendola, R. Pilot, M. Frasconi, O. M. Maragò, and M. A. Iatì, Surface plasmon resonance in gold nanoparticles: a review, *J. Phys.: Condens. Matter*, vol. 29, no. 20, p. 203002, 2017.
[22] S. Mariani and M. Minunni, Surface plasmon resonance applications in clinical analysis, *Anal Bioanal Chem*, vol. 406, no. 9, pp. 2303–2323, 2014.
[23] J.-H. Choi, J.-H. Lee, J. Son, and J.-W. Choi, Noble Metal-Assisted Surface Plasmon Resonance Immunosensors, *Sensors*, vol. 20, no. 4, p. 1003, 2020.
[24] Y. Liu *et al.*, Low-Cost Localized Surface Plasmon Resonance Biosensing Platform with a Response Enhancement for Protein Detection, *Nanomaterials (Basel)*, vol. 9, no. 7, 2019.
[25] K. Takemura, O. Adegoke, T. Suzuki, and E. Y. Park, A localized surface plasmon resonance-amplified immunofluorescence biosensor for ultrasensitive and rapid detection of nonstructural protein 1 of Zika virus, *PLOS ONE*, vol. 14, no. 1, p. e0211517, 2019.
[26] A.-C. Burdușel, O. Gherasim, A. M. Grumezescu, L. Mogoantă, A. Ficai, and E. Andronescu, Biomedical Applications of Silver Nanoparticles: An Up-to-Date Overview, *Nanomaterials (Basel)*, vol. 8, no. 9, 2018.
[27] S. Kumar, A. Shukla, P. P. Baul, A. Mitra, and D. Halder, Biodegradable hybrid nanocomposites of chitosan/gelatin and silver nanoparticles for active food packaging applications, *Food Packaging and Shelf Life*, vol. 16, pp. 178–184, 2018.
[28] M. E. K. Kraeling *et al.*, In vitro percutaneous penetration of silver nanoparticles in pig and human skin, *Regulatory Toxicology and Pharmacology*, vol. 95, pp. 314–322, 2018.
[29] Y. Zhou and R.-C. Tang, Facile and eco-friendly fabrication of AgNPs coated silk for antibacterial and antioxidant textiles using honeysuckle extract, *Journal of Photochemistry and Photobiology B: Biology*, vol. 178, pp. 463–471, 2018.
[30] K. Kejlová *et al.*, Characteristics of silver nanoparticles in vehicles for biological applications, *International Journal of Pharmaceutics*, vol. 496, no. 2, pp. 878–885, 2015.
[31] S. Lee and B.-H. Jun, Silver Nanoparticles: Synthesis and Application for Nanomedicine, *IJMS*, vol. 20, no. 4, p. 865, 2019.
[32] B. Le Ouay and F. Stellacci, Antibacterial activity of silver nanoparticles: A surface science insight, *Nano Today*, vol. 10, no. 3, pp. 339–354, 2015.
[33] T. T. N. Dung *et al.*, Silver nanoparticles as potential antiviral agents against African swine fever virus, *Mater. Res. Express*, vol. 6, no. 12, p. 1250g9, 2020.
[34] E. G. Haggag *et al.*, Antiviral potential of green synthesized silver nanoparticles of, Lampranthus coccineus and Malephora lutea, *International Journal of Nanomedicine*, 2019.
[35] S. W. Kim, J. H. Jung, K. Lamsal, Y. S. Kim, J. S. Min, and Y. S. Lee, Antifungal Effects of Silver Nanoparticles (AgNPs) against Various Plant Pathogenic Fungi, *Mycobiology*, vol. 40, no. 1, pp. 53–58, 2012.
[36] WHO ,Press release, *WHO*. https://www.who.int/whr/1996/media_centre/press_release/en/ (accessed Aug. 28, 2020).
[37] S. Talebian, G. G. Wallace, A. Schroeder, F. Stellacci, and J. Conde, Nanotechnology-based disinfectants and sensors for SARS-CoV-2, *Nat. Nanotechnol.*, vol. 15, no. 8, pp. 618–621, 2020.

[38] J. Wang *et al.*, Disinfection technology of hospital wastes and wastewater: Suggestions for disinfection strategy during coronavirus Disease 2019 (COVID-19) pandemic in China, *Environmental Pollution*, vol. 262, p. 114665, 2020.
[39] C. Weiss *et al.*, Toward Nanotechnology-Enabled Approaches against the COVID-19 Pandemic, *ACS Nano*, vol. 14, no. 6, pp. 6383–6406, 2020.
[40] C. Daruich De Souza, B. Ribeiro Nogueira, and M. E. C. M. Rostelato, Review of the methodologies used in the synthesis gold nanoparticles by chemical reduction, *Journal of Alloys and Compounds*, vol. 798, pp. 714–740, 2019.
[41] R. Herizchi, E. Abbasi, M. Milani, and A. Akbarzadeh, Current methods for synthesis of gold nanoparticles, *Artificial Cells, Nanomedicine, and Biotechnology*, vol. 44, no. 2, pp. 596–602, 2016.
[42] S. R. Ahmed *et al.*, In situ self-assembly of gold nanoparticles on hydrophilic and hydrophobic substrates for influenza virus-sensing platform, *Scientific Reports*, vol. 7, no. 1, pp. 1–11, 2017.
[43] H. Khateb, G. Klös, R. L. Meyer, and D. S. Sutherland, Development of a Label-Free LSPR-Apta Sensor for Staphylococcus aureus Detection, *ACS Appl. Bio Mater.*, vol. 3, no. 5, pp. 3066–3077, 2020.
[44] P. Kajal, K. Ghosh, and S. Powar, Manufacturing Techniques of Perovskite Solar Cells, in *Applications of Solar Energy*, H. Tyagi, A. K. Agarwal, P. R. Chakraborty, and S. Powar, Eds. Singapore: Springer Singapore, pp. 341–364, 2018.
[45] S. Y. Oh *et al.*, Development of gold nanoparticle-aptamer-based LSPR sensing chips for the rapid detection of Salmonella typhimurium in pork meat, *Sci Rep*, vol. 7, no. 1, p. 10130, 2017.
[46] F. Yaghubi, M. Zeinoddini, A. R. Saeedinia, A. Azizi, and A. Samimi Nemati, Design of Localized Surface Plasmon Resonance (LSPR) Biosensor for Immunodiagnostic of E. coli O157:H7 Using Gold Nanoparticles Conjugated to the Chicken Antibody, *Plasmonics*, 2020.
[47] M. Brust, D. Bethell, C. J. Kiely, and D. J. Schiffrin, Self-Assembled Gold Nanoparticle Thin Films with Nonmetallic Optical and Electronic Properties, *Langmuir*, vol. 14, no. 19, pp. 5425–5429, 1998.
[48] F. Toderas, M. Baia, L. Baia, and S. Astilean, Controlling gold nanoparticle assemblies for efficient surface-enhanced Raman scattering and localized surface plasmon resonance sensors, *Nanotechnology*, vol. 18, no. 25, p. 255702, 2007.
[49] W. Jang, H. Byun, and J.-H. Kim, Rapid preparation of paper-based plasmonic platforms for SERS applications, *Materials Chemistry and Physics*, vol. 240, p. 122124, 2020.
[50] M. Abulikemu, E. H. Da'as, H. Haverinen, D. Cha, M. A. Malik, and G. E. Jabbour, In Situ Synthesis of Self-Assembled Gold Nanoparticles on Glass or Silicon Substrates through Reactive Inkjet Printing, *Angew. Chem. Int. Ed.*, vol. 53, no. 2, pp. 420–423, 2014.
[51] M. Abulikemu and G. Jabbour, In situ synthesis of nanoparticles on substrates by inkjet printing,2014.
[52] X.-Y. Zhang *et al.*, Self-Assembly of Large-Scale and Ultrathin Silver Nanoplate Films with Tunable Plasmon Resonance Properties, *ACS Nano*, vol. 5, no. 11, pp. 9082–9092, 2011.
[53] A. Goyal *et al.*, In situ Synthesis of Metal Nanoparticle Embedded Free Standing Multifunctional PDMS Films, *Macromolecular Rapid Communications*, vol. 30, no. 13, pp. 1116–1122, 2009.

[54] M. Abulikemu, E. H. Da'as, H. Haverinen, D. Cha, M. A. Malik, and G. E. Jabbour, In Situ Synthesis of Self-Assembled Gold Nanoparticles on Glass or Silicon Substrates through Reactive Inkjet Printing, *Angewandte Chemie*, vol. 126, no. 2, pp. 430–433, 2014.
[55] R. Søndergaard, M. Hösel, D. Angmo, T. T. Larsen-Olsen, and F. C. Krebs, Roll-to-roll fabrication of polymer solar cells, *Materials Today*, vol. 15, no. 1, pp. 36–49, 2012.
[56] K. Cooper, Scalable Nanomanufacturing—A Review, *Micromachines*, vol. 8, no. 1, p. 20, 2017.
[57] A. Flower, Mark Andy | Flexographic Printing Presses | Digital Printing Presses. https://www.markandy.com/ (accessed Apr. 21, 2021).
[58] Voith. https://voith.com/corp-en/index.html (accessed Apr. 21, 2021).
[59] N. Sharma, G. Bhatt, and P. Kothiyal, Gold Nanoparticles synthesis, properties, and forthcoming applications : A review, *Indian Journal of Pharmaceutical and Biological Research*, vol. 3, no. 02, Art. no. 02, 2015.
[60] E. Sánchez-López *et al.*, Metal-Based Nanoparticles as Antimicrobial Agents: An Overview, *Nanomaterials*, vol. 10, no. 2, Art. no. 2, 2020.
[61] L. Marinescu *et al.*, Optimized Synthesis Approaches of Metal Nanoparticles with Antimicrobial Applications, *Journal of Nanomaterials*, vol. 2020, p. e6651207, 2020.
[62] J. Turkevich, P. C. Stevenson, and J. Hillier, A study of the nucleation and growth processes in the synthesis of colloidal gold, *Discuss. Faraday Soc.*, vol. 11, p. 55, 1951.
[63] M. Brust, M. Walker, D. Bethell, D. J. Schiffrin, and R. Whyman, Synthesis of thiol-derivatised gold nanoparticles in a two-phase Liquid–Liquid system, *J. Chem. Soc., Chem. Commun.*, vol. 0, no. 7, pp. 801–802, 1994.
[64] M. V. Kirichkov *et al.*, In situ analysis of the formation steps of gold nanoparticles by oleylamine reduction, *J Struct Chem*, vol. 58, no. 7, pp. 1403–1410, 2017.
[65] L. Uson, V. Sebastian, M. Arruebo, and J. Santamaria, Continuous microfluidic synthesis and functionalization of gold nanorods, *Chemical Engineering Journal*, vol. 285, pp. 286–292, 2016.
[66] C. Ziegler and A. Eychmüller, Seeded Growth Synthesis of Uniform Gold Nanoparticles with Diameters of 15−300 nm, *J. Phys. Chem. C*, vol. 115, no. 11, pp. 4502–4506, 2011.
[67] K. Kalimuthu, B. S. Cha, S. Kim, and K. S. Park, Eco-friendly synthesis and biomedical applications of gold nanoparticles: A review, *Microchemical Journal*, vol. 152, p. 104296, 2020.
[68] K. Kalimuthu, R. Suresh Babu, D. Venkataraman, Mohd. Bilal, and S. Gurunathan, Biosynthesis of silver nanocrystals by Bacillus licheniformis, *Colloids and Surfaces B: Biointerfaces*, vol. 65, no. 1, pp. 150–153, 2008.
[69] W.-Y. Ko, J.-Z. Chen, Y.-C. Yan, and K.-J. Lin, Nanoparticle-based thin film devices and their applications, *Journal of Nanomedicine & Nanotechnology*.
[70] H. Yang and P. Jiang, Large-Scale Colloidal Self-Assembly by Doctor Blade Coating, *Langmuir*, vol. 26, no. 16, pp. 13173–13182, 2010.
[71] S. A. Ng, K. A. Razak, A. A. Aziz, and K. Y. Cheong, The effect of size and shape of gold nanoparticles on thin film properties, *Journal of Experimental Nanoscience*, vol. 9, no. 1, pp. 64–77, Jan. 2014.
[72] M. Eslamian, Inorganic and Organic Solution-Processed Thin Film Devices, *Nanomicro Lett*, vol. 9, no. 1, 2017.

[73] L. Gonzalez-Macia and A. J. Killard, Screen printing and other scalable point of care (POC) biosensor processing technologies, in *Medical Biosensors for Point of Care (POC) Applications*, Elsevier, pp. 69–98, 2017.
[74] R. R. Søndergaard, M. Hösel, and F. C. Krebs, Roll-to-Roll fabrication of large area functional organic materials, *Journal of Polymer Science Part B: Polymer Physics*, vol. 51, no. 1, pp. 16–34, 2013.
[75] M. Singh, H. M. Haverinen, P. Dhagat, and G. E. Jabbour, Inkjet Printing-Process and Its Applications, *Adv. Mater.*, vol. 22, no. 6, pp. 673–685, 2010.
[76] J. Li, F. Rossignol, and J. Macdonald, Inkjet printing for biosensor fabrication: combining chemistry and technology for advanced manufacturing, *Lab Chip*, vol. 15, no. 12, pp. 2538–2558, 2015.
[77] A. Jilani, M. S. Abdel-wahab, and A. HosnyHammad, Advance Deposition Techniques for Thin Film and Coating, *Modern Technologies for Creating the Thin-film Systems and Coatings*, 2017.
[78] F. Aziz and A. F. Ismail, Spray coating methods for polymer solar cells fabrication: A review, *Materials Science in Semiconductor Processing*, vol. Complete, no. 39, pp. 416–425, 2015.
[79] A. Berni, M. Mennig, and H. Schmidt, Doctor Blade, in *Sol-Gel Technologies for Glass Producers and Users*, M. A. Aegerter and M. Mennig, Eds. Boston, MA: Springer US, pp. 89–92, 200.
[80] A. Chilvery, S. Das, P. Guggilla, C. Brantley, and A. Sunda-Meya, A perspective on the recent progress in solution-processed methods for highly efficient perovskite solar cells, *Sci Technol Adv Mater*, vol. 17, no. 1, pp. 650–658, 2016.
[81] G. Jabbour, M. Abulikamu, H. W. Choi, and H. Haverinen, Reactive Inkjet Printing as a Tool for in situ Synthesis of Self-Assembled Nanoparticles, in *Nanomaterials for 2D and 3D Printing*, John Wiley & Sons, Ltd, pp. 69–82, 2017..
[82] P. J. Smith and A. Morrin, Reactive inkjet printing, *J. Mater. Chem.*, vol. 22, no. 22, p. 10965, 2012.
[83] A. Khan, R. Rashid, G. Murtaza, and A. Zahra, Gold Nanoparticles: Synthesis and Applications in Drug Delivery, *Trop. J. Pharm Res*, vol. 13, no. 7, p. 1169, 2014.
[84] S. Jain, D. G. Hirst, and J. M. O'Sullivan, Gold nanoparticles as novel agents for cancer therapy, *Br J Radiol*, vol. 85, no. 1010, pp. 101–113, 2012.
[85] M. Cordeiro, F. Ferreira Carlos, P. Pedrosa, A. Lopez, and P. V. Baptista, Gold Nanoparticles for Diagnostics: Advances towards Points of Care, *Diagnostics (Basel)*, vol. 6, no. 4, 2016.
[86] K. A. Razak, S. R. Makhsin, N. D. Zakaria, and N. M. Nor, Gold nanoparticles for diagnostic development, p. 53.
[87] V. Lee, N. F. Mohd-Naim, E. Tamiya, and M. U. Ahmed, Trends in Paper-based Electrochemical Biosensors: From Design to Application., *Analytical sciences : the international journal of the Japan Society for Analytical Chemistry*, vol. 34, no. 1, pp. 7–18, 2018.
[88] R. J. Narayan, *Medical Biosensors for Point of Care (POC) Applications*. Elsevier, 2017.
[89] J. Hopkins, K. Fidanovski, A. Lauto, and D. Mawad, All-Organic Semiconductors for Electrochemical Biosensors: An Overview of Recent Progress in Material Design, *Front. Bioeng. Biotechnol.*, vol. 7, p. 237, 2019.

[90] Y. Li, H. J. Schluesener, and S. Xu, Gold nanoparticle-based biosensors, *Gold Bull*, vol. 43, no. 1, pp. 29–41, 2010.
[91] H. Aldewachi, T. Chalati, M. N. Woodroofe, N. Bricklebank, B. Sharrack, and P. Gardiner, Gold nanoparticle-based colorimetric biosensors, *Nanoscale*, vol. 10, no. 1, pp. 18–33, 2018.
[92] K. Saha, S. S. Agasti, C. Kim, X. Li, and V. M. Rotello, Gold Nanoparticles in Chemical and Biological Sensing, *Chem. Rev.*, vol. 112, no. 5, pp. 2739–2779, 2012.
[93] J. M. Pingarrón, P. Yáñez-Sedeño, and A. González-Cortés, Gold nanoparticle-based electrochemical biosensors, *Electrochimica Acta*, vol. 53, no. 19, pp. 5848–5866, 2008.
[94] S. Zhang, N. Wang, H. Yu, Y. Niu, and C. Sun, Covalent attachment of glucose oxidase to an Au electrode modified with gold nanoparticles for use as glucose biosensor, *Bioelectrochemistry*, vol. 67, no. 1, pp. 15–22, 2005.
[95] M. Vidotti, R. F. Carvalhal, R. K. Mendes, D. C. M. Ferreira, and L. T. Kubota, Biosensors based on gold nanostructures, *J. Braz. Chem. Soc.*, vol. 22, no. 1, pp. 3–20, 2011.
[96] P. A. Rasheed and N. Sandhyarani, Electrochemical DNA sensors based on the use of gold nanoparticles: a review on recent developments, *Microchim Acta*, vol. 184, no. 4, pp. 981–1000, 2017.
[97] P. Jiang, Y. Wang, L. Zhao, C. Ji, D. Chen, and L. Nie, Applications of Gold Nanoparticles in Non-Optical Biosensors, *Nanomaterials (Basel)*, vol. 8, no. 12, 2018.
[98] Z. Yan *et al.*, A label-free immunosensor for detecting common acute lymphoblastic leukemia antigen (CD10) based on gold nanoparticles by quartz crystal microbalance, *Sensors and Actuators B: Chemical*, vol. 210, pp. 248–253, 2015.
[99] J. Xu, Thin Films of Gold Nanoparticles: Temporal Stability and Mechanisms of Degradation, p. 55.
[100] A. R. Ferhan, L. Guo, X. Zhou, P. Chen, S. Hong, and D.-H. Kim, Solid-Phase Colorimetric Sensor Based on Gold Nanoparticle-Loaded Polymer Brushes: Lead Detection as a Case Study, *Anal. Chem.*, vol. 85, no. 8, pp. 4094–4099, 2013.
[101] F. Wang, X. Liu, C.-H. Lu, and I. Willner, Cysteine-Mediated Aggregation of Au Nanoparticles: The Development of a H_2O_2 Sensor and Oxidase-Based Biosensors, *ACS Nano*, vol. 7, no. 8, pp. 7278–7286, 2013.
[102] C. Chen and J. Wang, Optical biosensors: an exhaustive and comprehensive review, *Analyst*, vol. 145, no. 5, pp. 1605–1628, 2020.
[103] D. G. Drescher, D. Selvakumar, and M. J. Drescher, Chapter One - Analysis of Protein Interactions by Surface Plasmon Resonance, in *Advances in Protein Chemistry and Structural Biology*, vol. 110, R. Donev, Ed. Academic Press, pp. 1–30, 2018.
[104] J. Zhou *et al.*, Surface plasmon resonance (SPR) biosensors for food allergen detection in food matrices, *Biosensors and Bioelectronics*, vol. 142, p. 111449, 2019.
[105] Y.-C. Wong and R. J. L. Sr, *Analysis of Food Toxins and Toxicants*. John Wiley & Sons, 2017.
[106] N.-T. Nguyen, Chapter 4 - Fabrication technologies, in *Micromixers (Second Edition)*, N.-T. Nguyen, Ed. Oxford: William Andrew Publishing, 2012, pp. 113–161.
[107] P. A. Mosier-Boss, Review on SERS of Bacteria, *Biosensors (Basel)*, vol. 7, no. 4, 2017.
[108] S. Wang *et al.*, The Development of a Portable SPR Bioanalyzer for Sensitive Detection of Escherichia coli O157:H7, *Sensors*, vol. 16, no. 11, Art. no. 11, 2016.
[109] R. Gutiérrez-Gallego, E. Llop, J. Bosch, and J. Segura, Surface plasmon resonance in doping analysis," *Anal Bioanal Chem*, vol. 401, no. 2, pp. 389–403, 2011.

[110] K. A. Willets and R. P. Van Duyne, Localized Surface Plasmon Resonance Spectroscopy and Sensing, *Annu. Rev. Phys. Chem.*, vol. 58, no. 1, pp. 267–297, 2007.
[111] B. Sepúlveda, P. C. Angelomé, L. M. Lechuga, and L. M. Liz-Marzán, LSPR-based nanobiosensors, *Nano Today*, vol. 4, no. 3, pp. 244–251, 2009.
[112] D. Fitzpatrick, Chapter 4 - Glucose Biosensors, in *Implantable Electronic Medical Devices*, D. Fitzpatrick, Ed. Oxford: Academic Press, pp. 37–51. 2015.
[113] H.-T. Chou, W.-H. Huang, T.-M. Wu, Y.-K. Yu, and H.-C. Hsu, LSPR based glucose sensor using au nanoparticles fabricated by photochemical method, in *2017 International Conference on Applied System Innovation (ICASI)*, pp. 1591–1594, 2017.
[114] J. Chen, S. M. Andler, J. M. Goddard, S. R. Nugen, and V. M. Rotello, Integrating recognition elements with nanomaterials for bacteria sensing, *Chem. Soc. Rev.*, vol. 46, no. 5, pp. 1272–1283, 2017.
[115] H. Yousefi, M. M. Ali, H.-M. Su, C. D. M. Filipe, and T. F. Didar, Sentinel Wraps: Real-Time Monitoring of Food Contamination by Printing DNAzyme Probes on Food Packaging, *ACS Nano*, vol. 12, no. 4, pp. 3287–3294, 2018.
[116] S. Chandra, T. K. Mahto, A. R. Chowdhuri, B. Das, and S. kumar Sahu, One step synthesis of functionalized carbon dots for the ultrasensitive detection of Escherichia coli and iron (III), *Sensors and Actuators B: Chemical*, vol. 245, pp. 835–844, 2017.
[117] S. Y. Oh *et al.*, Development of gold nanoparticle-aptamer-based LSPR sensing chips for the rapid detection of Salmonella typhimurium in pork meat, *Sci Rep*, vol. 7, no. 1, p. 10130, 2017.
[118] R. Singh, M. D. Mukherjee, G. Sumana, R. K. Gupta, S. Sood, and B. D. Malhotra, Biosensors for pathogen detection: A smart approach towards clinical diagnosis, *Sensors and Actuators B: Chemical*, vol. 197, pp. 385–404.
[119] N. Alizadeh, M. Y. Memar, S. R. Moaddab, and H. S. Kafil, Aptamer-assisted novel technologies for detecting bacterial pathogens, *Biomedicine & Pharmacotherapy*, vol. 93, pp. 737–745, 2017.
[120] S. M. Yoo, D.-K. Kim, and S. Y. Lee, Aptamer-functionalized localized surface plasmon resonance sensor for the multiplexed detection of different bacterial species, *Talanta*, vol. 132, pp. 112–117, 2015.
[121] Y.-F. Chang *et al.*, Simple Strategy for Rapid and Sensitive Detection of Avian Influenza A H7N9 Virus Based on Intensity-Modulated SPR Biosensor and New Generated Antibody, *Anal. Chem.*, vol. 90, no. 3, pp. 1861–1869, 2018.
[122] B. Luo *et al.*, A novel immunosensor based on excessively tilted fiber grating coated with gold nanospheres improves the detection limit of Newcastle disease virus, *Biosensors and Bioelectronics*, vol. 100, pp. 169–175, 2018.
[123] J.-H. Lee, B.-C. Kim, B.-K. Oh, and J.-W. Choi, Highly sensitive localized surface plasmon resonance immunosensor for label-free detection of HIV-1," *Nanomedicine: Nanotechnology, Biology and Medicine*, vol. 9, no. 7, pp. 1018–1026, 2013.
[124] S. H. Lee and B.-H. Jun, Silver Nanoparticles: Synthesis and Application for Nanomedicine, *Int J Mol Sci*, vol. 20, no. 4, 2019.
[125] Y. Y. Hong Hu, A Review on Antimicrobial Silver Absorbent Wound Dressings Applied to Exuding Wounds, *J Microb Biochem Technol*, vol. 07, no. 04, 2015.
[126] I. Negut, V. Grumezescu, and A. M. Grumezescu, Treatment Strategies for Infected Wounds, *Molecules*, vol. 23, no. 9, Art. no. 9, 2018.

[127] J. M. Corrêa, M. Mori, H. L. Sanches, A. D. da Cruz, E. Poiate, and I. A. V. P. Poiate, Silver Nanoparticles in Dental Biomaterials, *International Journal of Biomaterials*, 2015.
[128] M. Ishihara, V. Q. Nguyen, Y. Mori, S. Nakamura, and H. Hattori, Adsorption of Silver Nanoparticles onto Different Surface Structures of Chitin/Chitosan and Correlations with Antimicrobial Activities, *International Journal of Molecular Sciences*, vol. 16, no. 6, Art. no. 6, 2015.
[129] T. Ibn-Mohammed *et al.*, A critical analysis of the impacts of COVID-19 on the global economy and ecosystems and opportunities for circular economy strategies, *Resour Conserv Recycl*, vol. 164, p. 105169, 2021.
[130] R. K. Kakhki, M. K. Kakhki, and A. Neshani, COVID-19 target: A specific target for novel coronavirus detection, *Gene Reports*, vol. 20, p. 100740, 2020.
[131] S. Galdiero, A. Falanga, M. Vitiello, M. Cantisani, V. Marra, and M. Galdiero, Silver Nanoparticles as Potential Antiviral Agents, *Molecules*, vol. 16, no. 10, pp. 8894–8918, 2011.
[132] C. J. Burrell, C. R. Howard, and F. A. Murphy, Chapter 4 - Virus Replication, in *Fenner and White's Medical Virology (Fifth Edition)*, C. J. Burrell, C. R. Howard, and F. A. Murphy, Eds. London: Academic Press, pp. 39–55, 2017.
[133] Z. K *et al.*, Polysulfone ultrafiltration membranes impregnated with silver nanoparticles show improved biofouling resistance and virus removal, *Water Res*, vol. 43, no. 3, pp. 715–723, 2008.
[134] B. D. Gusseme *et al.*, Biogenic Silver for Disinfection of Water Contaminated with Viruses, *Appl. Environ. Microbiol.*, vol. 76, no. 4, pp. 1082–1087, 2010.
[135] D. Baram-Pinto, S. Shukla, N. Perkas, A. Gedanken, and R. Sarid, Inhibition of Herpes Simplex Virus Type 1 Infection by Silver Nanoparticles Capped with Mercaptoethane Sulfonate, *Bioconjugate Chem.*, vol. 20, no. 8, pp. 1497–1502, Aug. 2009.
[136] H. H. Lara, N. V. Ayala-Nuñez, L. Ixtepan-Turrent, and C. Rodriguez-Padilla, Mode of antiviral action of silver nanoparticles against HIV-1, *Journal of Nanobiotechnology*, vol. 8, no. 1, p. 1, 2010.
[137] J. Elechiguerra *et al.* , *J Nanobiotechnol*, vol. 3, no. 1, p. 6, 2005.
[138] J. L. Speshock, R. C. Murdock, L. K. Braydich-Stolle, A. M. Schrand, and S. M. Hussain, Interaction of silver nanoparticles with Tacaribe virus, *J Nanobiotechnol*, vol. 8, no. 1, p. 19, 2010.
[139] S. Gaikwad *et al.*, Antiviral activity of mycosynthesized silver nanoparticles against herpes simplex virus and human parainfluenza virus type 3, *Int J Nanomedicine*, vol. 8, pp. 4303–4314, 2013.
[140] S. Nakamura *et al.*, Synthesis and Application of Silver Nanoparticles (Ag NPs) for the Prevention of Infection in Healthcare Workers, *Int J Mol Sci*, vol. 20, no. 15, 2019.
[141] M. P. Lythgoe and P. Middleton, Ongoing Clinical Trials for the Management of the COVID-19 Pandemic, *Trends in Pharmacological Sciences*, vol. 41, no. 6, pp. 363–382, 2020.
[142] D. C. Wheelock, Comparing the COVID-19 Recession with the Great Depression, *es*, vol. 2020, no. 39, 2020.
[143] M. A. Shereen, S. Khan, A. Kazmi, N. Bashir, and R. Siddique, COVID-19 infection: Origin, transmission, and characteristics of human coronaviruses, *Journal of Advanced Research*, vol. 24, pp. 91–98, 2020.

[144] X. Ou *et al.*, Characterization of spike glycoprotein of SARS-CoV-2 on virus entry and its immune cross-reactivity with SARS-CoV, *Nat Commun*, vol. 11, no. 1, p. 1620, 2020.
[145] Understanding SARS-CoV-2 and the drugs that might lessen its power, *The Economist*, 2020.
[146] R. Vazquez-Munoz and J. L. Lopez-Ribot, Nanotechnology as an Alternative to Reduce the Spread of COVID-19, *Challenges*, vol. 11, no. 2, p. 15, 2020.
[147] D. S. Sarkar, Silver Nanoparticles with Bronchodilators Through Nebulisation to Treat COVID 19 Patients., *Journal of Current Medical Research and Opinion*, vol. 3, no. 04, Art. no. 04, 2020.
[148] A. Salleh *et al.*, The Potential of Silver Nanoparticles for Antiviral and Antibacterial Applications: A Mechanism of Action, *Nanomaterials*, vol. 10, no. 8, Art. no. 8, 2020.
[149] F. Papadopulos *et al.*, Common Tasks in Microscopic and Ultrastructural Image Analysis Using ImageJ, *Ultrastructural Pathology*, vol. 31, no. 6, pp. 401–407, 2007.
[150] X. Liu, M. Atwater, J. Wang, and Q. Huo, Extinction coefficient of gold nanoparticles with different sizes and different capping ligands, *Colloids and Surfaces B: Biointerfaces*, vol. 58, no. 1, pp. 3–7, 2007.
[151] S. Krishnamurthy, A. Esterle, N. C. Sharma, and S. V. Sahi, Yucca-derived synthesis of gold nanomaterial and their catalytic potential, *Nanoscale Res Lett*, vol. 9, no. 1, p. 627, 2014.
[152] X. Liu *et al.*, A study on gold nanoparticle synthesis using oleylamine as both reducing agent and protecting ligand, *J Nanosci Nanotechnol*, vol. 7, no. 9, pp. 3126–3133, 2007.
[153] L. Ratke and P. W. Voorhees, *Growth and Coarsening: Ostwald Ripening in Material Processing*. Springer Science & Business Media, 2002.
[154] J. C. Martínez, N. A. Chequer, J. L. González, and T. Cordova, Alternative Metodology for Gold Nanoparticles Diameter Characterization Using PCA Technique and UV-VIS Spectrophotometry, *NN*, vol. 2, no. 6, pp. 184–189, Jan. 2013.
[155] E. Smirnov, *Assemblies of Gold Nanoparticles at Liquid-Liquid Interfaces: From Liquid Optics to Electrocatalysis*. Springer International Publishing, 2018.
[156] S. Sachdev *et al.*, Synthesis of Gold Nanoparticles Using the Interface of an Emulsion Droplet, *Langmuir*, vol. 33, no. 22, pp. 5464–5472, 2017.
[157] S. S. Jeremiah, K. Miyakawa, T. Morita, Y. Yamaoka, and A. Ryo, Potent antiviral effect of silver nanoparticles on SARS-CoV-2, *Biochemical and Biophysical Research Communications*, vol. 533, no. 1, pp. 195–200, 2020.
[158] A. Chakraborty and A. Diwan, NL63: A Better Surrogate Virus for studying SARS- CoV-2, p. 9, 2020.
[159] Log and Percent Reductions in Microbiology and Antimicrobial Testing | Microchem Laboratory.https://microchemlab.com/information/log-and-percent-reductions-microbiology-and-antimicrobial-testing (accessed Feb. 17, 2021).
[160] J. R. Swathy, M. U. Sankar, A. Chaudhary, S. Aigal, Anshup, and T. Pradeep, Antimicrobial silver: An unprecedented anion effect, *Scientific Reports*, vol. 4, no. 1, Art. no. 1, 2014.